Multi-metal nano-materials as efficient electrocatalysts

Liuqing Pang

THESE DE DOCTORAT

Présentée à

L'UNIVERSITE DE LILLE

pour obtenir le grade de

DOCTEUR EN SCIENCES

Dans la spécialité :

Micro-nanosystèmes et Capteurs

par

Liuqing PANG

Multi-Metal Nano-Materials as Efficient Electrocatalysts

Nano-matériaux multi-métaux en tant qu'électrocatalyseurs efficaces

Co-directeurs de thèse :

Dr. Rabah Boukherroub

Prof. Sabine Szunerits

Soutenue le 10/07/2020 devant le jury d'examen :

Dr. Bruno Fabre	**Université de Rennes 1, France**	**Rapporteur**
Dr. François Ozanam	**Ecole Polytechnique, France**	**Rapporteur**
Prof. Alexandru Vlad	**Université Catholique de Louvain, Belgique**	**Examinateur**
Prof. Henri Happy	**IEMN, France**	**Président du jury**

Abstract

In this thesis, we have developed high-efficiency, high-stability, and cost-effective electrocatalysts using a simple and environmentally friendly process. Firstly, we prepared new $PtRu_2$ nanoparticles supported on sulphur- and nitrogen-co-doped crumbled graphene with trace amounts of iron ($PtRu_2$/PF) electrocatalyst by one-step hydrothermal process. The $PtRu_2$/PF catalyst achieved a current density of 10 $mA \cdot cm^{-2}$ at a low overpotential value of only 22 mV for HER at pH=1 and a current density of 10 mA cm^{-2} at an overpotential of only 270 mV for the OER in alkaline solution. Interestingly, this catalyst was also efficient for methanol oxidation reaction (MOR) in acidic solution and oxygen reduction reaction (ORR) in 0.1 M KOH solution. Secondly, we described the preparation of a hybrid material consisting of cobalt oxide decorated on nitrogen-doped MoS_2 supported on carbon fibers (CoO/N-MoS_2/CF) through a two-step process combining hydrothermal technique and electrochemical deposition. The CoO/N-MoS_2/CF achieved a current density of 10 mA cm^{-2} at an overpotential of only 78 mV for the HER and a current density of 50 mA cm^{-2} at 458 mV for the OER in 1.0 M KOH. Additionally, the CoO/N-MoS_2/CF delivered a maximum current density of 53 mA cm^{-2} at an applied cell voltage of 1.5 V for a two-electrode water splitting. Thirdly, we showed for the first time the extraordinarily capacity of perforated gold nanoholes (Au NHs) electrodes for electrochemical water splitting under illumination with light. The strong plasmonic electromagnetic enhancement, which occurs under illumination of the perforated Au NHs electrode, facilities the dissociation of water into H_2. The overpotential for the HER occurs on such plasmonic electrodes at a current density of 100 mA cm^{-2} was 205 mV, largely improved compared to the reference material, Pt. The fast electrocatalytic behavior of the interface was attested by a low Tafel slope of 33 mV dec^{-1}. All of these

materials were characterized by a variety of different techniques, such as SEM, TEM, XRD, XPS, Raman and electrochemical measurements.

Key words: $PtRu_2$/PF, CoO/N-MoS_2/CF, Au NHs, HER, OER, water splitting.

Résumé

Dans ce travail de thèse, nous avons synthétisé des catalyseurs très efficaces et stables en utilisant un processus simple et respectueux de l'environnement. Premièrement, nous avons préparé des nanoparticules de $PtRu_2$ supportées sur un matériau à base de graphène co-dopé au soufre et à l'azote renfermant des traces de fer ($PtRu_2$/PF) par une réaction hydrothermale. Le catalyseur $PtRu_2$/PF peut produire une densité de courant de 10 mA cm^{-2} à une faible valeur de surtension de 22 mV pour HER à pH = 1, et une densité de courant de 10 mA cm^{-2} à une surtension de 270 mV pour l'OER en milieu alcalin. De plus, ce catalyseur est également très efficace pour l'oxydation du méthanol (MOR) en milieu acide et pour la réduction d'oxygène (ORR) dans une solution 0.1 M KOH. Dans la deuxième partie de mon travail de thèse, nous décrivons la préparation d'un matériau hybride constitué d'oxyde de cobalt décoré sur MoS_2 dopé à l'azote supporté sur des fibres de carbone (CoO/N-MoS_2/CF) en combinant la technique hydrothermale et le dépôt électrochimique. Le CoO/N-MoS_2/CF a fourni une densité de courant de 10 mA cm^{-2} à une surtension de 78 mV pour la réaction de dégagement d'hydrogène (HER) et une densité de courant de 50 mA cm^{-2} à 458 mV pour la réaction de dégagement d'oxygène (OER) dans 1.0 M KOH. De plus, le CoO/N-MoS_2/CF a permis de générer une densité de courant maximale de 53 mA cm^{-2} à une tension de cellule appliquée de 1.5 V pour l'électrolyse d'eau dans un système à deux électrodes. Dans la troisième partie de mon travail de thèse, nous avons montré pour la première fois l'effet de plasmons de surface localisés pour accélérer la réaction électrochimique de dégagement d'hydrogène en utilisant un film mince d'or nanostructuré, sous un éclairage avec de la lumière dans le proche infrarouge. La génération d'un champ électromagnétique intense, sous l'éclairage de l'électrode perforée de nano-trous d'or (Au NH), facilite la dissociation de l'eau en H_2. La surtension nécessaire pour le dégagement d'hydrogène sur de telles électrodes plasmoniques

est de 205 mV pour produire une densité de courant de 100 mA cm^{-2}, largement améliorée par rapport au matériau de référence, le Pt. Le comportement électrocatalytique est aussi caractérisé par une faible pente de Tafel de 33 mV dec^{-1}. L'ensemble des matériaux préparés dans ce travail ont été caractérisés par une variété de techniques différentes, telles que la microscopie électronique à balayage (MEB), en transmission (MET), la diffractométrie de rayons X (DRX), spectrométrie photoélectronique X (XPS), la spectroscopie Raman et des mesures électrochimiques.

Mots clés : $PtRu_2$/PF, CoO/N-MoS_2/CF, Au NHs, HER, OER, fractionnement de l'eau.

Acknowledgments

My research work was performed in the Nano-Bio-Interfaces (NBI) group at the Institute of Electronics, Microelectronics and Nanotechnology (IEMN). Three years period is so short in our long journey of life. However, these three years are the most memorable postgraduate life. Our scientific research capability is improved here, and our innovative ability is also developed here. Therefore, I would like to thank all the teachers and friends who have helped me. You have given me the most selfless care and dedication. Thank you, because with you, I am full of confidence and gained a lot on the road of life.

From the beginning of the project to the successful completion of the dissertation, first and foremost, I would like to thank my supervisors, Dr. Rabah Boukherroub and Prof. Sabine Szunerits, for their patience and guidance over the past three years. With their enormous help and supervision, I have obtained a lot of precious research experience such as laboratory technique and knowledge in chemistry and materials. It was truly a great pleasure to study under their mentorships.

I would like to express my thanks to Dr. Bruno Fabre, Dr. François Ozanam, Prof. Alexandru Vlad and Prof. Henri Happy for accepting to be in my thesis defense committee. I truly appreciate your time and your helpful comments.

In the past three years, for the experimental tests, I thank Dr. Ahmed Addad and Dr. Pascal Roussel, because they gave me a lot of support and help in materials characterization and analysis. Here, I send my most sincere thanks to them.

My heartfelt thanks go to all my colleagues for all the help, discussions and sharing. To Alex, it is such a pleasure to work with you in the same lab for three years. Thanks for all those generous help and valuable advice. Also, many thanks go to Mathias, Vlad, Quentin,

Madjid, Tamazouzt, Léa, Chengnan Li, Tianlong Yu, Jing Zhang, Yuan Zhang, Min Li and Yuanyuan Miao… It is truly my honor to work with all of you.

I would like also to thank my friends, Shuie Sun, Ce Zheng, Ningkui Wang, Siyuan Wang, Hong Pan, Zhuojun Jiang and Xiya Ma… for their friendship and big support.

In particular, I wish to thank the China Scholarship Council (CSC), which offered me the opportunity to pursue my PhD study in France.

Thanks to my family and my beloved parents. From child to now, they gave me unlimited support and encouragement, and created the best learning and living conditions for me. Their simplicity, hard-working, strong, practical and humble will benefit me for life! Thanks to my boyfriend Xiao Jianfeng for his support and encouragement! Thanks to my other friends for their care and encouragement!

PANG Liuqing

Villeneuve d'Ascq, France

09th May, 2020

Table of Contents

List of Acronyms and Symbols

$RuCl_3$	ruthenium (III) chloride
K_2PtCl_4	potassium tetrachloroplatinate(II)
$FeCl_3•6H_2O$	iron chloride hexahydrate
DMF	dimethylformamide
CTAB	cetyltrimethylammonium bromide
$Co(NO_3)_2$	cobalt(II) nitrate
$(NH_4)_2S_2O_8$	ammonium persulfate
EDOT	ethylenedioxythiophene
KOH	potassium hydroxide
HCl	hydrochloric acid
NH_4F	ammonium fluoride
H_2SO_4	sulfuric acid
Na_2MoO_4	sodium molybdate
CF	carbon fiber
CO	carbon monoxide
H_3BO_3	boric acid
$FeCl_2•4H_2O$	iron(II) chloride tetrahydrate
$NaH_2PO_2·\ H_2O$	sodium hypophosphite monohydrate
$NaBH_4$	sodium borohydride
NPs	nanoparticles
CH_4N_2S	thiourea
NF	nickel foam
Au NHs	gold nanoholes

CVD	chemical vapor deposition
CV	cyclic voltammetry
GC	glassy carbon
SEM	scanning electron microscopy
TEM	transmission electron microscopy
TiO_2	titanium dioxide
UV	ultraviolet
XRD	X-ray diffraction
UV-Vis	ultraviolet-visible spectroscopy
XPS	X-ray photoelectron spectroscopy
ICP-OES	Inductively coupled plasma optical emission spectrometry

General Introduction

Hydrogen (H_2) has been considered as the most promising and renewable energy carrier. With the advantages of low cost and high efficiency, electrochemical water splitting is a promising approach to produce H_2 with high purity. However, the practical application of water splitting for mass production of H_2 is greatly hindered by the high applied bias voltage and electrode stability required in an electrolyzer arising from the two-half reactions in water splitting, namely, cathodic hydrogen evolution reaction (HER) and anodic oxygen evolution reaction (OER).

Currently, Pt-group metals are the most effective catalysts for HER, while the benchmark catalysts for OER are Ir/Ru-based compounds. However, high cost and scarcity of these metals limit their widespread use. Therefore, enormous efforts have been dedicated to the development of nano-scale non-noble metal catalysts with high dispersibility, large specific surface area, and electrocatalytic activity for water splitting.

CHAPTER 1

Introduction

1.1 Development of world energy structure

The current global energy crisis, including the rapid growth of total energy demand, high prices of non-renewable energy, shortages of coal and other fossil fuels, severe environmental pollution and the greenhouse effect, has a negative impact on the human being [1]. Therefore, people are gradually looking for renewable clean energy. The world's energy structure is currently undergoing a gradual transition from oil and gas to new energy sources. Therefore, various countries are actively developing renewable and clean energy sources other than fossil fuels [2].

Since 1979, Japan has successively launched the "Sunshine Plan" for the development of new energy technology research, the "Moonlight Plan" for the development of energy-saving technology research, and the "New Sunshine Plan" for accelerating the development of comprehensive technologies in the energy and environmental fields. In addition, in November 2008, the US government, the world's largest energy consumer, also launched a series of new energy policies, including attempts to stimulate awareness of investment in clean energy in the next 10 years. Furthermore, Europe also attaches great importance to the development of new energy, and has launched various projects such as "Clean Urban Transport for Europe", and invested a lot of financial resources in the development of new energy.

Due to the high energy conversion rate and low operating temperature of fuel cells, they are considered as an ideal renewable energy source to overcome future energy anxiety [3], even though they require electrocatalysts with good activity and stability [4].

At the same time, hydrogen (H_2), as a substitute for gasoline and diesel, has also received extensive attention from experts. The rational use of renewable clean energy is no longer just

a manifestation of human civilization and progress, but also an important way and long-term strategy to achieve sustainable development.

1.1.1 Significance to develop hydrogen (H_2)

H_2 is an important chemical raw material for a large number of applications such as ammonia production and petroleum refining, and represents the most ideal secondary energy source [5]. Compared with fossil energy, it has the following five advantages: (1) H_2 is the most common element in nature, and its density is the smallest compared to all elements; (2) H_2 is non-toxic. Compared with other fuels, H_2 combustion is the cleanest. The main product of combustion in the air is water, which is non-polluting.[6] And then water could split to produce H_2. This cycle makes H_2 a resource-constrained peaceful green energy; (3) The calorific value of H_2 is about 1.4×10^5 kJ/kg, which is the highest among all fuels except nuclear energy; (4) In the energy industry, H_2 is the best heat transfer carrier; (5) H_2 can not only generate thermal energy-mechanical work through combustion in a heat engine, but also convert non-storable renewable energy sources such as solar energy into storable H_2 energy by photoelectrochemical water splitting.[7] Furthermore, a large amount of H_2 is stored in water [8]. Because of the above-listed characteristics, H_2 is recognized as "the oil of the future" and the most promising clean energy source. However, because the generation of H_2 requires a large amount of energy along with its low efficiency and difficulty to transport, H_2 research and development is of great significance.

In fact, many researchers are working to achieve the goal of the widespread application of H_2, so that it can provide more convenience for human life and work [9]. To this end, mankind has made many achievements: (1) the artificial earth satellites used by soviet astronaut Gagarin in 1957 and the Apollo spacecraft that first landed on the moon in 1968 both recorded the contribution of H_2 fuel; (2) H_2 vehicles produced by using H_2 instead of gasoline can increase the fuel utilization efficiency by 20%, which is undoubtedly the most

ideal green vehicle; (3) H_2-oxygen (O_2) generators that use H_2 and O_2 combustion to generate electricity. In addition, H_2 has a simple structure and the power generation capacity is higher than that of ordinary power stations; (4) Application of H_2 fuel cell [10-12]. It can be used to build fixed power stations, vehicles, ships and mobile power; (5) H_2 can be used in human life. People can store H_2 and use it to turn on kitchen stoves and air conditioners, etc., which is expected to create more comfort for human beings.

1.2 H_2 development progress

Since the 1970s, H_2 energy has become a competitive candidate because of its environmental friendliness, green sustainability and high energy density [13-15]. Several methods have been applied to produce H_2 fuel. At present, scientists have been able to simulate the photosynthesis of plants to produce H_2, which is cheaper and safer than other methods, and is expected to be used for H_2 production on an industrial scale in the future [16-18]. H_2 production through photosynthesis of plants is a simple and non-polluting way, but it is very unstable (**Figure 1**). For example, hydrogenase activity in the chloroplasts of *Chlamydomonas reinhardtii* increases under low-oxygen environment, so that [H] is converted into H_2, and eukaryotic green algae can also produce H_2 under light conditions. These two are the prospect of biological H_2 production, however, under natural environment, this process will be affected by the outside world, so its H_2 production process is unstable.

Secondly, reducing protons H^+ is one of the methods that artificially simulated photosynthesis uses to convert and store solar energy. Using photo-electric decomposition of water is actually a process of photosynthesis in the natural world. The main components of photoelectrochemical (PEC) water splitting devices are the semiconductor light absorbing photoelectrodes, the electrolyte and the separation membrane. The basic principle behind PEC water splitting is the conversion of solar energy to hydrogen by applying an external bias on to the photovoltaic materials immersed in an electrolyte, which contains a semiconductor

exposed to light. The electricity is then used for water electrolysis [19-21]. Among them, the most critical is the efficiency of the semiconductor photocatalyst. Ultimately, to improve the conversion efficiency of solar energy to chemical energy, it is necessary to prevent the recombination of electron-hole pairs, generated upon light irradiation of the semiconductor. Scientists generally use a method of supporting a co-catalyst on the surface of a semiconductor catalyst, and therefore whether the catalytic performance of the supported co-catalyst is good or bad will directly affect the level of water decomposition efficiency [22-25]. With the rise of new energy sources, the use of solar energy and other energy sources for large-scale decomposition of water to produce H_2 energy has gradually become the goal of all countries in the world [26-28]. By photo-catalytic H_2 production technology, the goal of decomposing H_2 from aquatic products at lower temperatures can be achieved [29-31]. However, the photolectrochemical approaches have low efficiency (**Figure 1**) [32-35].

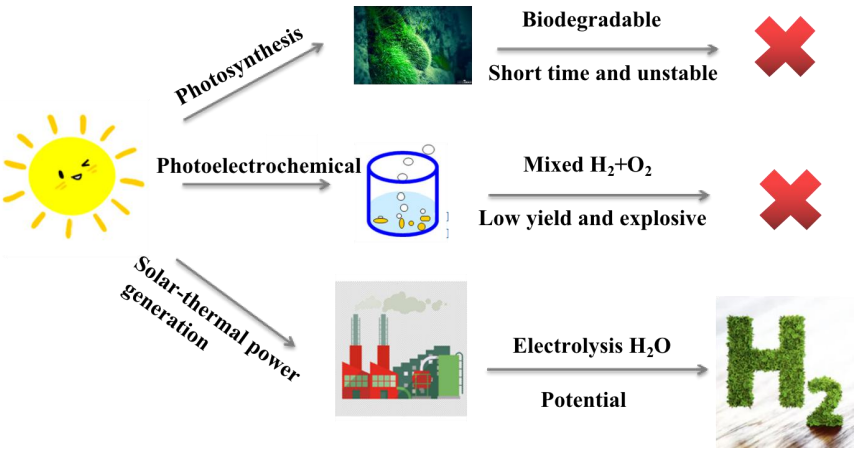

Figure 1. The three main ways of hydrogen production under the support of modern technology.

The third way for H_2 production is electrolysis of water. H_2, produced by the electrochemical water splitting, has been considered as the most promising and renewable energy carrier [36-40]. With the advantages of low cost and high efficiency, electrochemical

overall water splitting (OWP) is a promising approach to produce H_2 with high purity [41-43]. By far, this energy conversion technology has attracted extensive attention due to its high energy conversion efficiency, negligible environment pollution, and potentially wide range of applications [44-47]. However, the practical application of OWP for mass production of H_2 is greatly hindered by the large overpotential required for the two-half reactions in an electrolyzer for OWP [48-50], namely, the cathodic hydrogen evolution reaction (HER) and anodic oxygen evolution reaction (OER).

1.2.1 Photoelectrochemical (PEC) water splitting

Solar energy is highly regarded by people for its advantages of reproducibility and pollution-free [51-53]. There are three main ways to use solar energy: The first is solar-to-heat conversion. This is a simple and ancient method, but it is the most widely distributed method. Generally, people use solar water heaters, solar stoves and other methods [54-56]. The second is solar-to-electric conversion. That is, under light irradiation, the separation effect of electron and hole pairs occurs in the semiconductor p-n junction. Solar photovoltaic is the most promising way to use solar energy today [57-59]. The third is solar-to-chemical conversion. The conversion of solar to chemical energy generally refers to H_2 energy or storage of energy in organic matter. The way is mainly photosynthesis and chemical energy is transformed by plants in nature [60-63]. But the conversion efficiency is too low. Therefore, people use this idea to artificially convert solar energy into chemical energy.

PEC decomposition of water is a method of solar energy conversion and storage with great application prospects [64-66]. The environment in which human beings live is rich in water resources and solar energy is inexhaustible. If these two can be comprehensively used, this will solve the energy crisis. From the perspective of energy conversion, during the water decomposition, solar energy can be converted into chemical energy of H_2 fuel through semiconductor photoelectrodes [67-69]. PEC water splitting is initiated with photo-induced

charges of semiconductor electrodes under solar illumination [70-72]. Taking the water decomposition in an n-type semiconductor-based PEC unit as an example, the PEC water decomposition step can be summarized as follows (see **Figure 2A**). (i) When the n-type semiconductor electrode absorbs photons with energy higher than its band gap, electrons and holes are generated in the conduction and valence bands of the *n*-type semiconductor electrode, respectively. (ii) If the valence band edge of the *n*-type semiconductor is higher than the water oxidation potential (1.23 V *vs.* RHE), the water molecules will be split into oxygen molecules on the *n*-type photo-electrode *via* the theoretical oxidation ability of photo-induced holes. (iii) Meanwhile, the electrons of the *n*-type photo-electrode are directionally transferred to the counter electrode *via* bias driving through the outer circuit. When the conduction band edge of the *n*-type semiconductor or the applied bias on the counter electrode is lower than the proton reduction potential (0 V *vs.* RHE), the water mole protons are theoretically reduced into H_2 on the counter electrode. In the case of *p*-type semiconductor-based PEC cells, the water molecules or protons are photoelectrochemically reduced into H_2 on the surface of the *p*-type photo-electrode, while the water molecules are oxidized into O_2 on the counter electrode *via* photo-excited holes (**Figure 2B**). In addition, the water molecules could be reduced and oxidized simultaneously in a tandem system composed of an appropriate *n*-type photo-electrode and a *p*-type photo-electrode (**Figure 2C**). On the whole, the fundamental principles of PEC organic synthesis are similar to PEC water splitting. In essence, both of them involve solar-driven oxidation or reduction reactions on semiconductor electrodes [74].

For PEC water splitting, the semiconductor electrode is the heart of the PEC system; thus, its performance has a fundamental influence on the efficiency of the water splitting [74-76]. It is generally accepted that an effective PEC reaction involves seamless cooperation between light harvesting, charge separation, and the surface reaction of the semiconductor

electrode [77-79]. With consideration for the integral PEC reaction process, the ideal semiconductor electrode for PEC water splitting should exhibit the following properties: (i) suitable band gap for wide absorption of solar light; (ii) modest band edge position to straddle a specific oxidation or reduction reaction potential; (iii) satisfactory PEC reaction stability in electrolytes; (iv) high charge transfer and separation efficiency as well as fast PEC kinetic reaction; and (v) acceptable production cost and abundance of raw materials [80-82]. In the past few decades, almost all possible binary metal oxide semiconductors have been investigated as photo-electrode materials for PEC applications; however, a satisfactory photo-electrode remains elusive.

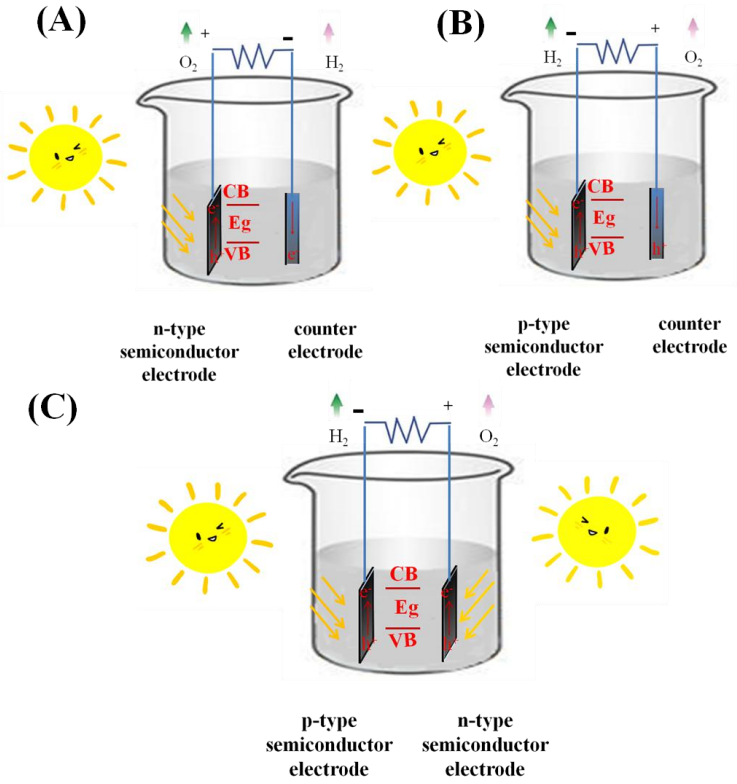

Figure 2. (A) Water decomposition in an *n*-type semiconductor-based PEC unit. (B) Water decomposition in a *p*-type semiconductor-based PEC unit. (C) Water decomposition in an *n*-type and a *p*-type semiconductor-based PEC unit [74].

1.2.2 Electrochemistry of water splitting

1.2.2.1 Current state of electrochemical water splitting

H_2 production by water electrolysis can be divided into alkaline water electrolysis, proton exchange membrane water electrolysis, and solid oxide water electrolysis.

The industrial application of water electrolysis technology began in the 1920s. The alkaline water electrolysis technology has achieved industrial scale H_2 production and is used in industrial needs such as ammonia production and petroleum refining. After the 1970s, energy shortage, environmental pollution, and space exploration requirements drove the development of proton exchange membrane electrolysis water technology. At the same time, the high-pressure compact alkaline electrolyzed water technology required for the development of special fields has also been developed accordingly. At present, the practical application of electrolyzed H_2 production technology mainly includes alkaline liquid water electrolysis and solid polymer water electrolysis.

The alkaline liquid water electrolysis technology uses KOH or NaOH aqueous solutions as electrolytes, and electrolyzes water under the action of direct current to generate H_2 and O_2. The alkaline liquid water electrolysis was industrialized in the mid-20^{th} century. The technology is relatively mature, with an operating life of up to 15 years.

1.2.2.2 Basic set-up for liquid water splitting systems

Water electrolysis produces H_2 and O_2 at the cathode and anode, respectively. At the anode, water is decomposed into O_2 along with protons and electrons, this is the oxygen evolution reaction (OER) [83, 84]. At the cathode, H_2 evolves by recombination of the protons and electrons, this is called hydrogen evolution reaction (HER) [85]. As shown in **Figure 3**, a typical electrolyzer consists of three parts: an aqueous electrolyte, an anode and a cathode [86]. The bifunctional HER-OER catalysts are applied on both the anode and cathode to speed up the overall water splitting reaction. When an external voltage is applied between

the two electrodes, the OER and HER occur at the anode and cathode, respectively [86-88]. Depending on the electrolytes in which water splitting proceeds, the water splitting reaction can be described as shown below.

Total reaction $$H_2O = H_2 + ½O_2 \quad (1)$$

In acidic solution

Cathode $$2H^+ + 2e^- = H_2 \quad (2)$$

Anode $$H_2O = 2H^+ + ½\,O_2 + 2e^- \quad (3)$$

In alkaline solution

Cathode $$2H_2O + 2e^- = H_2 + 2OH^- \quad (4)$$

Anode $$2OH^- = H_2O + ½\,O_2 + 2e^- \quad (5)$$

The thermodynamic voltage of water splitting is known to be 1.23 V regardless of the reaction medium [89]. In order to perform water decomposition at a practical rate, we must apply additional voltage to the cell and the overall operational voltage (V_{op}) for water splitting can be described as:

$$V_{op} = 1.23\,V + \eta_a + |\eta_c| + \eta_\Omega \quad (6)$$

where η_Ω represents the excess potential applied for compensating the system internal resistance, such as solution resistance and contact resistance [90-92]. η_a and η_c are the overpotentials required to overcome the intrinsic activation barriers of the anode and cathode, respectively. The intrinsic activation barriers can be minimized by using highly active OER and HER catalysts. In view of this, the primary challenge for research is to develop efficient bifunctional water splitting electrocatalysts, preferably based on low-cost and earth-abundant elements such that η_a and $|\eta_c|$ are minimized and the water splitting efficiency is improved [93-95].

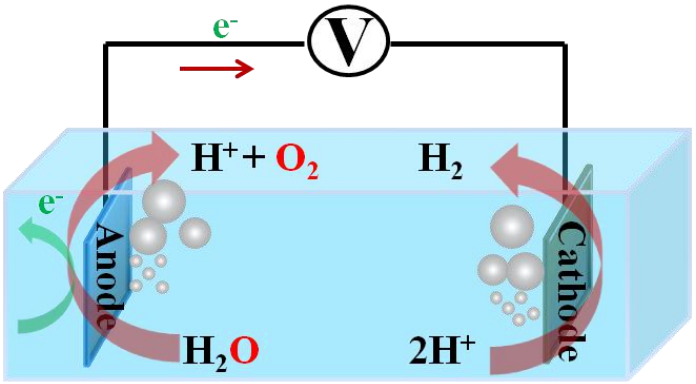

Figure 3. A typical electrolyzer consists of three parts: an aqueous electrolyte, an anode and a cathode.

According to theoretical calculations, when the voltage between the cathode and anode is greater than 1.23 eV, the production process of water splitting can be achieved. However, due to the overpotential, the required energy will increase, and the required applied voltage between the H_2 and O_2 electrodes will also increase, and the minimum voltage necessary to decompose water is 1.8 eV [96]. In the experimental process, Pt, Pd, and Ru are commonly used as catalysts to improve the efficiency of water splitting [97-99]. However, their price is high. Therefore, we need to understand the mechanism of water decomposition reaction, so as to select the appropriate material as a catalyst candidate [100].

1.3 Fundamentals of water electrolysis

1.3.1 Cathode: fundamentals of the hydrogen evolution reaction (HER)

Almost all common metals have undergone extensive research for HER [101-105]. Generally, the HER process involves three steps in acidic and alkaline media [106]:

Volmer reaction (electrochemical hydrogen adsorption)

$$H^+ + M + e^- \rightarrow MH_{ads} \quad \text{(in acidic medium)} \quad (7)$$

$$H_2O + M + e^- \rightarrow MH_{ads} + OH^- \quad \text{(in alkaline medium)} \quad (8)$$

Followed by Heyrovsky reaction (electrochemical desorption)

$$MH_{ads} + H^+ + e^- \rightarrow M + H_2 \quad \text{(in acidic medium)} \quad (9)$$

$$MH_{ads} + H_2O + e^- \rightarrow M + OH^- + H_2 \quad \text{(in alkaline medium)} \quad (10)$$

Or

Tafel reaction (chemical desorption)

$$2MH_{ads} \rightarrow 2M + H_2 \quad (11)$$

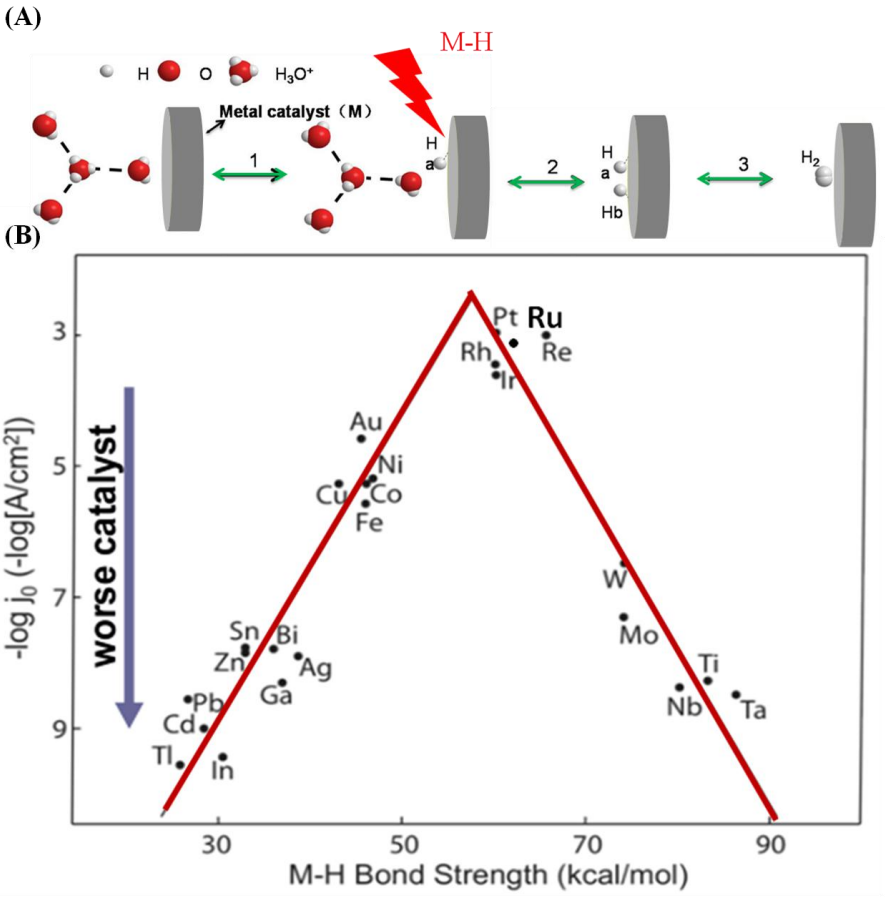

Figure 4. The mode of adsorption reaction on the metal cathode surface and volcano-like relationship between the negative logarithm for exchange current density and metal-hydrogen bond energy for hydrogen evolution reaction.

It is well known that the activity of the electrode material towards the HER depends on its electronic structure. As displayed in **Figure 4**, Trasatti plotted the logarithm of the

exchange current density, log j_0, on different metals against the metal-hydrogen (M-H) bond strength for the HER in acidic condition [107]. From the mechanism of HER, it can be divided into two steps, H_2 adsorption reaction (1) (Volmer reaction), electrochemical desorption reaction (Heyrovsky reaction) or composite adsorption reaction (2 or 3) (Tafel reaction), where reactions (2) and (3) are competing with each other [108-110]. It can be seen from the above reaction process that if the M-H bond is too weak, it will affect the formation of the intermediate product M-H. Conversely, if the M-H bond is too strong, it is not leading to the desorption reaction of this intermediate to produce the final product (**Figure 4B)**. In the volcanic relationship in the **Figure 4B**, Pt is closest to the volcanic mountain top compared to other metals, that is, the Pt-H bond energy is closer to the optimal M-H bond energy.

In combination with the overpotential values of different catalysts shown in **Figure 4A** for H_2 release, it turns out that Pt is the best H_2 electrode catalyst. This so-called volcano curve permits a quick comparison of the activities of different metals. However, the reported volcano plots for HER kinetics as a function of M-H bond energies (or metal properties) usually does not take into consideration other parameters such as solution pH. In fact, a three-dimensional (3D) volcano curve should be plotted with pH in the third axis. However, reliable data for alkaline solution kinetics are far from sufficient for drawing such a plot. Therefore, future efforts to advance the volcano plot for the HER under basic conditions will be valuable for the overall alkaline electrolysis reaction [111-114].

1.3.2 Anode: thermodynamics of the oxygen evolution reaction (OER)

Promotion of OER by transition metal oxides [115-117], hydroxides [118-120], and perovskites [121-123] has been extensively studied. Compared to HER mechanisms, the OER mechanisms and pathways are relatively more complex. O_2 is generally emitted from a surface of metal oxide, but not from the bare metal, and the OER mechanism is different for oxides with different surface structures. Due to the differences in thickness and structures of

their oxide layers and preparation methods, even oxides with identical compositions may produce different electro-kinetic profiles. In spite of this, a general mechanism for the OER on oxides has been proposed as follows:

$$M + H_2O \rightarrow MOH + H^+ + e^- \quad (12)$$

$$MOH \rightarrow MO + H^+ + e^- \text{ or } 2MOH \rightarrow MO + M + H_2O \quad (13)$$

$$2MO \rightarrow 2M + O_2 \text{ or } MO + H_2O \rightarrow M + O_2 + 2H^+ + 2e^- \quad (14)$$

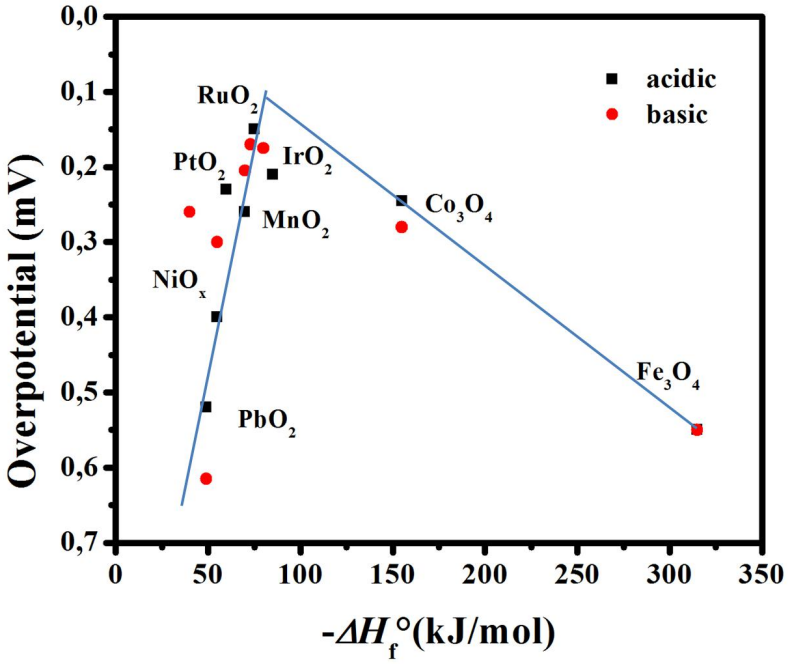

Fig. 5 Volcano-like relationship between overpotential at ~ 1 mA cm^{-2} and surface oxygen binding strength in acidic and basic media.

Figure 5 displays the volcano plot showing the activity of O_2 generation on first-row transition metal oxide surfaces against the transition enthalpy of the oxides in either acidic or basic conditions. As seen, noble metal oxides, RuO_2 and IrO_2, are located at the top of the plot because of their low redox potential and good electrical conductivity. However, their high price and limited HER activity make these precious-metal based oxides unsuitable for use as bifunctional catalysts in large scale water splitting. Conversely, cheaper and more sustainable

bifunctional transition metal compound catalysts have demonstrated high activity for both HER and OER with electrochemical stability.

1.4 Catalytic materials for water splitting

1.4.1 HER catalysts

As mentioned earlier, it is worthwhile to understand the effect of these electrocatalysts on improving the HER performance. Herein, we will provide an overview of the recent studies on noble metal, non-noble metal and metal-free catalysts. The HER performances of the reported electrocatalysts are listed in **Table 1**.

1.4.1.1 Noble metal catalysts

I. Pt-based materials

Noble metals including Pt, Ru, Rh, Ir and Pd, have been proven as excellent cathode catalysts for HER [124]. Among these metals, Pt is the best HER catalyst because it has an overpotential close to 0 V, however, its widespread use is restricted by scarcity and high price [124].

Currently, three major strategies have been considered to reduce the amount of Pt without compromising its electrocatalytic activity: (i) Increasing the number of reactive sites through the fabrication of a nanostructured Pt surface to expose more active sites [125-127]. Nanostructured metal catalysts are attracting significant attention in a variety of energy devices including fuel cells, sensors, Li-ion batteries, supercapacitors, thermoelectric devices and memory devices [128-132]. When the size of the metals reaches to the nanometer scale, new physical and chemical properties appear due to the existence of quantum size effect [133]. In addition, nanostructured metals could provide a much higher specific surface area than their bulk counterparts, which is advantageous for energy devices because the reaction/interaction between the electrodes' surface and the interacting media can be

significantly enhanced [134]. (ii) Apart from synthesizing metals at the nanometer scale, new, optimized and enhanced properties can also be achieved by alloying noble metals with other metals (e.g., with noble metals, metal oxides, carbon materials and so on) [135-137] to increase the site-specific activity. Single-component nanomaterials may not be able to meet the strict requirements of future electrocatalytic devices and their inherent physical properties, such as conductivity, recyclability, and stability need additional improvement [138-142].

Reasonably, introducing one or several different metals to contact with single-phase nanomaterials has brought great hope to alleviate the above challenges. For example, Zheng and coworkers designed Pt-decorated Ni_3N nanosheet electrocatalysts to achieve alkaline HER at a current density of 200 mA/cm^2 at an overpotential of 160 mV. Ni_3N species not only improved the electron conductivity, but also promoted water dissociation with the ultrathin surface oxidation layer formed under the ambient atmosphere [143].

Apart from interface engineering, the alloy structure provides another means for the construction of multiple sites. Lee and coworkers prepared hexapod Pt@Ni@Co alloy nanocatalysts that exhibited better HER activity than commercial Pt/C catalysts. The introduction of Co facilitated the H-OH cleavage reaction for better Volmer step kinetics [144].

Recently, doping was also employed in Pt-based materials for HER. Wang and coworkers prepared N-modified Pt-Ni nanowires to deliver ultralow over-potential of 13 mV at a current density of 10 mA/cm^2 [145]. The common goal of these developments is to minimize Pt loading for potential large-scale commercial applications.

II. Ru-based materials

Because of its relatively low cost (~4% the price of Pt) and a similar bond strength as Pt with hydrogen, Ru exhibits stronger water dissociation ability than that of Pt metal. Ru has

become the most promising water splitting catalyst among all the non-Pt noble metals [146-149].

Recent work has shown that combining Ru-based nanostructures or chelating metal atoms leads to a new class of catalysts for HER [150-153]. Qiao and coworkers reported anomalous $Ru/C_3N_4/C$ catalysts that exhibited small overpotential of 79 mV at a current density of 10 mA/cm^2 and 2.5 times higher TOF value than that of Pt/C catalyst [146]. In consideration of the relatively high price of Ru, it is meaningful to further reduce the particle size of Ru and improve the atomic utilization of Ru. In this regard, Feng and coworkers prepared single Ru atoms in an N-doped carbon matrix *via* the calcination of Ru^{3+} and polyaniline complex precursor on graphite foam (Ru/NC) under N_2 protection [147]. The obtained Ru/NC catalyst exhibited a geometric current density of 10 mA/cm^2 at an overpotential of 21 mV.

Recently, new insights were obtained with regard to accelerating water dissociation kinetics and obtaining optimal hydroxyl adsorption *via* isolating Co atoms into the Ru lattice. Li and coworkers prepared Co-substituted Ru nanosheets with an HER current density of 10 mA/cm^2 at a low overpotential of 13 mV [151]. Most of the Ru-based electrocatalysts showed remarkable HER catalytic performance with lower overpotential and longtime stability, and also exhibited better or comparable activity with commercial Pt/C electrocatalysts.

1.4.1.2 Non-noble metal HER electrocatalysts

In the past few decades, in order to find a suitable alternative for noble metals, researchers have studied various non-noble catalysts for the HER. However, non-noble metals always display poor activity and/or stability [136].

Currently, many efforts have been devoted to develop various strategies for designing active structures, such as components, interfaces, and defects [154-156]. Generally, metallic cathodes with a denser microstructure are detrimental to HER. Therefore, developing

cathodes with a nanostructured surface is a key method to improve the activity and reduce the overpotential [157].

Due to their high electrocatalytic activities, earth abundance and low cost, many earth-abundant transition-metal based compounds including transition metal sulfides, phosphides, nitrides, carbides and oxides have been widely explored [158-159].

I. Metal sulfides based HER catalysts

Metal sulfides are the largest class of materials for electrocatalysis due to their intriguing structural and electronic properties [159]. Metal sulfides can be divided into layered transition-metal disulfides and non-layered metal sulfides, according to their two-dimensional (2D) form [160]. Bulk transition-metal disulfides (non-layered metal sulfide) consist of monolayers stacked by van der Waals forces, whereas the general crystal structure of a transition-metal disulfide monolayer can be described as a sandwich structure where the 2D transition metal is situated between two layers of chalcogen [161]. The development of 2D transition-metal disulfide electrocatalysts has the greatest potential for achieving low-cost and high-performing electrocatalysts for clean energy conversion applications [162].

The representative 2D transition-metal disulfide material, molybdenum disulfide (MoS_2), has received widespread attention due to its fascinating physical and chemical properties and reduced dimensionality. It has been shown that the electrochemical catalytic activity of MoS_2 is highly dependent on the amount of sulfur-terminated edges, while the in-plane structure is catalytic inert [163, 164].

In recent years, to improve the performance of MoS_2 for HER, three approaches have been attempted. One possible approach is structural engineering i.e. manipulating the MoS_2 structure at the nanoscale, including nanotubes [165], nanowires [166], nanostructured films [167], and nanosheets [168]. Another efficient strategy is to enhance the intrinsic activity through introduction of structural defects and disorder, enhancing the activity of S edge sites

to activate the inert basal plane [169]. Nørskov et al. demonstrated that strained MoS_2 *via* the introduction of sulphur vacancies and strain exhibited an enhanced HER activity [170].

The third way is to increase the electrical conductivity through chemical exfoliation and coupling with an appropriate substrate. Chemical exfoliation is an efficient method to reduce charge transfer loss and lower the stacking between MoS_2 layers [170, 171]. Chhowalla proposed a solvent-free chemical stripping method, which subsequently eliminated surface charges, thereby constructing highly conductive 1T-MoS_2 nanosheets as HER catalysts [172]. In addition to chemical exfoliation, an electrocatalyst should be used in combination with a suitable support to overcome its poor conductivity and further enhancing its catalytic activity for HER. Dai's team firstly prepared reduced graphene oxide decorated with MoS_2 nanoparticles through a solvothermal method [173]. The MoS_2/rGO hybrid materials provided abundant active edge sites, resulting in high electrocatalytic activity for HER. Their work provided inspiration for the synthesis of an advanced MoS_2 electrocatalyst with highly conductive substrates.

II. Metal phosphides based HER catalysts

Given their structural similarities to hydrogenase, transition metal phosphides are of interest for HER catalysis. The negatively charged P atoms in the catalyst can capture protons and act as sites for H_2 dissociation [174]. In addition, anodic electrochemical treatment, including O_2 evolution, result in an amorphous transition metal oxyhydroxide shell on the surface of the catalysts which can act as catalytically active shell for O_2 evolution [175]. The combination of these properties and bifunctional character confer catalytic properties for transition metal phosphides that are appropriate for overall water splitting. Schaak *et al.* reported various transition metal phosphides obtained from commercially available metal foils (Fe, Co, Ni, Cu, and NiFe) with good HER and OER catalytic activities [176].

Recently, in order to enhance the density of exposed active sites, the design of nanostructured transition metal phosphides has become a hot topic. Tour *et al.* reported porous nanorods with a mixed-phase of Co phosphide/Co phosphate with superior activity for catalytic H_2 and O_2 evolution reactions [177]. Liu et al. developed sulfur-doped cobalt phosphide with an attractive performance for chemical water splitting [178]. Among the transition metal phosphides, nickel and cobalt phosphides are thought to be more active than other materials [176].

1.4.1.3 Metal-free catalysts

For most catalytic processes involving redox reactions, the active components of the catalyst are generally metals. Carbon materials are formed from carbon atoms through different bonding methods. In particular, due to the advantages of high electronic conductivity, ideal microstructure, good resistance to corrosion, functional carbon materials such as activated carbon, carbon nanotubes, carbon fibers, and graphene (including graphene oxide and reduced graphene oxide) have been widely used as substrates for the deposition of electrocatalytic materials [179]. Qu et al. have reviewed the use of graphene materials for the electrocatalytic splitting of water, indicating that graphene has been extensively researched and therefore has been implemented to play a variety of roles in electrochemistry field, such as being the electrochemical platform and/or as a functionalizable support [180]. However, pristine graphene-based composite electrodes often suffer from poor stability and low mass activity [180].

It is well known that carbon-based composites have a promising application potential in the electrochemical field of batteries, supercapacitors, and electrocatalysts [179]. Currently, replacing some carbon atoms of the original graphene by heteroatoms (N, P, or S) is a viable approach to fine-tune its electronic structure and chemical/electrochemical properties. In this way, the electrocatalytic properties of carbon materials for the HER can be significantly

improved by heteroatom doping [181]. Qiao's research team conducted a comprehensive study on the effect of heteroatom dopants in graphene on HER activity [182]. They designed and synthesized N, P, S, B, O, F doped or dual-doped graphene as metal-free electrocatalysts for the HER. Their results indicated that N and P could coactivate adjacent C atoms in the graphene matrix by adjusting the valence orbital energy level. It was found that the double-doped graphene has a higher HER activity than the corresponding single-doped one [182]. Besides graphene, other carbon materials such as N- and S-co-doped porous carbon materials [183], N-doped activated carbon fiber [184], and B-doped multi-walled carbon nanotubes [185] were also reported as effective water electrolysis catalysts, and some of them showed comparable properties to those of traditional metallic catalysts.

Table 1. Summary of the HER performance of some reported electrocatalysts.

Catalyst	Condition	E (V) at J =-10 mA cm^{-2}	Tafel slope ($mV\ dec^{-1}$)	Reference
Pt-Ni_3N	1 M KOH	0.05	36.5	[143]
Pt@Ni@Co	0.1 M KOH	0.022	/	[144]
N-Pt-Ni	1 M KOH	0.013	76	[145]
Ru/C_3N_4/C	0.1 M KOH	0.079	61	[146]
Ru NPs/NC	1 M KOH	0.112	31	[147]
$Ni_{43}Ru_{57}$	0.5 M H_2SO_4	0.041	31	[148]
Ru@CN-0.16	1 M KOH	0.05	53	[149]
Ru@C_2N	0.5 M H_2SO_4	0.02	30	[150]
Co-Ru NSs	1 M KOH	0.013	29	[151]
S-MoS_2@C	0.5 M H_2SO_4	136	/	[154]
$Fe_{0.54}Co_{0.46}S_{0.92}$/CNTs/CC	1 M KOH	70	55	[155]

Cu NDs/Ni_3S_2 NTs-CFs	1 M KOH	0.128	72.6	[156]
Cu-Mo-S	0.5 M H_2SO_4	0.096	52	[162]
$MoSe_2$	0.5 M H_2SO_4	/	105	[167]
O-MoS_2	0.5 M H_2SO_4	0.2	55	[171]
1T MoS_2	0.5 M H_2SO_4	0.2	40	[172]
MoS_2/RGO	0.5 M H_2SO_4	0.12	41	[173]
Co phosphide/phosphate	0.5 M H_2SO_4	0.15	53	[177]
CoS-P/CNT	0.5 M H_2SO_4	0.048	55	[178]
N-S/rGO	0.5 M H_2SO_4	0.27	81	[181]
N-S/C	0.5 M H_2SO_4	0.1	57	[183]

1.4.2 OER catalysts

As mentioned above, due to the complex four electron oxidation process, the OER has a more significant overpotential than HER. So far, the effective catalysts for decreasing the OER overpotential of water splitting are mainly Ru and Ir-based catalysts [186]. Just like other noble metals, the price and scarcity of Ru and Ir-based catalysts hinder their large-scale applications [186-188].

A large amount of effort and progress have been invested in developing OER catalysts with low cost materials or a reduced amount of Ir (Ru). Therefore, it is necessary to obtain an O_2 release catalyst with the advantages of simple preparation method, low price, low overpotential and good stability [189].

To date, remarkable progress has been made on non-noble metal catalysts, such as transition metal oxides, sulfides, phosphides etc [190-192]. The OER performances of the reported electrocatalysts are listed in **Table 2**.

1.4.2.1 Cobalt-based catalysts for OER

Co-based catalysts represent an interesting class of materials for electrocatalytic processes, owing to the high abundance of Co element on the earth, which is economically affordable and far lower price than precious metals such as Pt, Ru and Ir. And metallic Co is a promising catalyst selection for the OER [157].

In order to exploit highly efficient alternative OER electrocatalysts, numerous Co-based catalysts such as metal oxides, hydro(oxy)oxides, sulfides and phosphates have been studied [193]. Coupling Co-based catalysts with catalytic or conductive materials could further enhance the catalytic performance [194].

Recently, Co based catalysts with more rational 3D core/shell heterostructures have also attracted considerable attention due to their high surface area, and fast electron and electrolyte transfer ability [195]. Gu et al. fabricated a hierarchical $Co_3O_4@Co_xFe_{3-x}O_4$ core/shell structure on Ni foam, this kind of porous heterostructure had a large surface area and good conductivity, and revealed a high activity with an OER current density of 10 mA/cm^2 at a low overpotential of 200 mV [196]. Co-based catalysts have been recognized as highly efficient and economical O_2 release catalysts.

1.4.2.2 Layered double hydroxides (LDH)-based catalysts for OER

LDH, which belong to hydrotalcite-like compounds, are a large group of 2D anionic clay materials. In particular, metallic cations from the transition group can enhance the charge transport of the material [157]. To date, a large number of LDHs have been developed for electrochemical supercapacitors, electrochemical sensors, electrocatalysis and so on [197].

However, they usually show an unsatisfactory conductivity and their 2D microstructure limits the specific surface area per geometric area [198-200]. In order to solve these problems, the aid of nanoarray architectures on conductive substrates or assistance by conductive carbon materials or Ni foam was considered [201]. It has been found that with the help of a support, the conventional planar structure of LDH materials can be reconstructed into a 3D architecture with a high active surface area [202-204].

In addition, it should be noted that LDH materials have relatively weak interlayer bonding. Thus, it is possible to expand the interlayer distance in LDHs with the assistance of anions and some small organic molecules [205-207]. Song *et al.* reported that increasing the inter-layer distance is a prerequisite for improving OER performance [205]. Sun *et al.* reported a ternary LDH containing Ni, Fe and Mn cations, which exhibited better OER activity than NiFe LDH and commercial Ir/C catalysts [206]. Yang *et al.* synthesized multi-transition metal based LDHs *via* controlling the ratio of tri- and bi-valent ions. The as-prepared FeNiCo LDH showed advanced catalytic activity than binary metal NiFe or NiCo [207].

Table 2. Summary of the OER performances of some reported electrocatalysts.

Catalyst	Condition	E (V) at J =10 mA cm^{-2}	Tafel slope ($mV\ dec^{-1}$)	Reference
CoMn LDH	pH = 7	0.281	43	[191]
ex-situ Co	1 M KOH	/	61	[192]
CoV-UAH	1 M KOH	0.215	/	[193]
Co_3O_4/N-rmGO	1 M KOH	0.31	67	[194]
$Co_{1.8}Ni(OH)_{5.6}$@$Co_{1.8}NiS_{0.4}(OH)_{4.8}$	0.10 M KOH	0.274	45	[195]

Co_3O_4@ $CoxFe_{3-x}O_4$/NF	1 M KOH	<0.27	53	[196]
NiFe LDH	0.10 M KOH	0.26	55	[198]
Co_4Fe_2-LDHs/$Co(OH)_2$	1 M KOH	<0.2	/	[201]
NiCo-LDH/NF	1 M KOH	0.37	113	[202]
NiFe/3D-ErGO	1 M KOH	<0.27	39	[203]
CQD/NiFe-LDH	1 M KOH	0.24	30	[204]
NiFe-NS	1 M KOH	0.3	40	[205]
NiFeMn-LDH	1 M KOH	0.24	47	[206]
$FeNi_8Co_2$-LDH	1 M KOH	0.22	42	[207]

1.5 Oxygen reduction reaction (ORR) catalysts

The proton exchange membrane fuel cells (PEMFCs), built by the electrodes, electrolyte, catalyst, and gas diffusion layers, are able to transform the chemical energy liberated during the electrochemical reaction of H_2 and O_2 to electrical energy, as opposed to the direct combustion of H_2 and O_2 to produce thermal energy [208]. And the ORR plays an important role in PEMFCs [209]. The development of high-efficient catalysts for ORR is an important area of renewable energy research to cope with the rapidly growing energy demand [210]. Although a wide range of materials have been proposed theoretically and experimentally, most of them have not yet been implemented as potential catalysts from an industrial perspective [211]. **Table 3** summarizes some of the ORR performances of the reported electrocatalysts.

1.5.1 Noble metal ORR catalysts

Although significant achievements have been made on the non-Pt catalysts, Pt is well-supported by many experimental observations to provide large current densities and low ORR overpotentials, while being selective to the direct 4-electron reaction [212].

The ORR on a Pt electrode in acidic solutions is as follows:

$$O_2 + 2H^+ + 2e^- \rightarrow H_2O_2 \quad (15)$$

in alkaline solution, the reaction may proceed *via*:

$$O_2 + H_2O + 2e^- \rightarrow HO_2^- + OH^- \quad (16)$$

or

$$O_2 + 2H_2O + 4e^- \rightarrow 4OH^- \quad (17)$$

It is well-established that the ORR in acidic solutions is a very slow process and the final product is H_2O_2. Increasing the intrinsic activity and exposed active sites for Pt-based catalysts can be readily manipulated by alloying [213-215], constructing well-defined shapes [216] and reducing the particle size [217, 218]. For instance, Yamauchi and co-workers reported Pt-Pd hollow nanostructures with excellent electrocatalytic activities, due to their high surface area and the synergistic effect with secondary or ternary metals [217]. Adzic *et al.* reported the preparation of a core-shell structured catalyst with titanium nickel nitride as the core, and the Pt content was significantly reduced to 5% compared with commercial 20% Pt/C [219]. Presently, it appears that the ORR activity is not a challenge anymore, with ever-increasing mass activity reported by numerous works, whereas the cost and durability are the key challenging issues for the fuel cell commercialization.

1.5.2 Non-noble metal ORR catalysts

The major merits of non-noble metal catalysts include abundant reserves and low costs compared with the noble metals [220]. In general, it is known that transition metal nitrides are

more stable compared with oxides, because of the high energy of triple bonds between metal and N atoms [221]. Liao *et al.* described a binary titanium nickel nitride synthesized by doping Ni into the TiN nanocrystals with high ORR activity in acidic electrolytes; the activity was almost comparable to that of commercial Pt/C catalyst [222]. Transition metal phosphides and sulfides are also regarded as potential ORR electrocatalysts in view of the rich chemical valence of P and S atoms, which could lead to different redox couples in the catalytic processes [223-225], offering new opportunities to design active and durable ORR electrocatalysts. However, the current non-noble metal-based catalysts exhibit unsatisfactory intrinsic activities, in particular, their ORR activities are far more inferior compared with Pt/C catalysts in acidic electrolytes. There is still a long way to go for non-noble metal-based catalysts to be competitive for ORR [220].

1.5.3 Metal-free ORR catalysts

In the past few years, carbon nanomaterials also have become an alternative ORR electrocatalysts [220]. These are widely available nanomaterials with unique characteristics that make them ideal for several electrochemical applications. As catalyst supports, carbon materials have several advantages, such as increased active surface area, enhanced conductivity and so on [226]. These characteristics led to improved overall electrocatalytic properties and durability of carbon materials-based electrocatalysts. There are many types of carbon nanomaterials and the most famous are carbon nanotubes (CNTs), carbon fibers (CF) and graphene (G) [227-229].

The carbon-based materials can be broadly divided into two categories, transition metal-doped and heteroatom (non-metal)-doped carbon materials. For transition metal-doped carbon materials, for example, the FeN_x/C catalyst is one of the most desirable carbon-based ORR electrocatalysts. However, this class of ORR catalysts still suffer from insufficient activity in acidic media [223]. As non-metal-doped electrocatalysts, the most promising alternatives are

carbon nanomaterials doped with nitrogen, sulfur and phosphorus[230-232]. Xia *et al.* reported a highly porous hollow framework of N-doped CNTs with Co nanocrystals and the improved ORR activity is mainly ascribed to the beneficial composition and the robust hollow carbon matrix composed of interlaced N-doped CNTs [233].

Apart from the activity, the stability of carbon-based ORR catalysts is also a key challenge for researchers. The demetallation and carbon corrosion are believed to be the main degradation mechanisms for carbon-based catalysts/cathodes. Though various approaches for achieving high performance have been established for numerous carbon-based ORR catalysts, the evaluation at the large scale for these carbon-based catalysts appears less reported and is in fact urgently required.

Table 3. Summary of the ORR performances of some reported electrocatalysts.

Catalyst	Solution (O_2-saturated)	RDE (rpm)	Potential (V)	J (mA cm^{-2})	Ref.
GN–Pt–IL	0.5 M H_2SO_4	1600	0.6	4.4	[209]
PtAg	0.1 M KOH	1600	0.6	5	[211]
$Pt_{2ML}/Ni_{1ML}/Pt$	0.1 M $HClO_4$	1600	0.6	5.8	[215]
PtPd	0.1 M $HClO_4$	1600	0.6	6	[217]
TiNiN@Pt	0.1 M $HClO_4$	1600	0.6	5	[219]
Fe-N-rGO	0.5 M H_2SO_4	1600	0.6	2	[220]
$Ti_{0.95}Ni_{0.05}N$	0.1 M KOH	1600	0.6	5.5	[222]
PFA-P doped	0.5 M H_2SO_4	1500	0.2	2.5	[230]
PF-1000	0.5 M H_2SO_4	1600	0.6	6.2	[231]
NT-NG	0.1 M $HClO_4$	1600	0.6	5.5	[232]

1.6 Summary

As the global energy crisis and environmental pollution problems continue to intensify, people have gradually paid attention to the research of renewable and clean energy. H_2 has become an ideal energy carrier due to its high combustion value, clean and pollution-free products, and reproducible use. At present, the method of decomposing water into H_2 and O_2 is an ideal method for producing hydrogen. Therefore, the research on the decomposition of water to produce hydrogen has become a research hot spot in recent years.

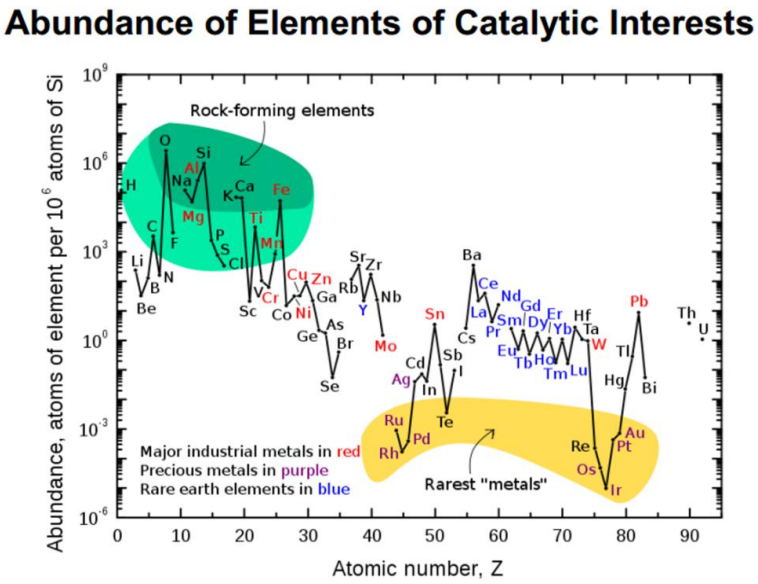

Figure 6. The relative content distribution of elements in the crust.

To promote the efficiency of water electrolysis and reduce the cost, the key is to develop highly-efficient, low cost electrocatalysts with a low overpotential as well as low Tafel slope for the HER and OER. At present, the best hydrogen-producing catalyst is Pt. However, as it can be seen from **Fig. 6**, the content of Pt in the earth's crust is low, so its price is quite high. To maximize the utilization of these rare resources, nanostructured noble metals have been widely studied to enhance the catalytic performance. Deposition of a small amount of noble metal on a low-cost support or alloying is another alternative way to reduce the amount while retaining or even enhancing the catalytic properties.

In recent years, more attention has been focused on the preparation of non-noble materials and metal-free materials. Especially, designing and fabricating nanostructured catalysts, and foreign element doping or alloying can increase the surface area, density of exposed active sites and conductivity. Furthermore, various conductive supports have been employed to prepare special non-noble metal micro-structured electrocatalysts with noble metal-like properties.

In order to reveal a good performance, the HER is generally conducted in acid solution, while the OER in an alkaline environment. Thus, when they are combined in a water electrolysis system, many serious problems could occur: low activity, poor stability or low corrosion resistance. Therefore, in future studies, it will be necessary to prepare water splitting catalysts that can operate in the same electrolytic solution. For other fuel cells, methanol oxidation and oxygen reduction reactions, the catalyst is the key influencing factor. In order to exploit more mature catalysts as the cathode and anode, research based on the requirement of practical applications need more attention.

1.7 Objectives

At present, the method of decomposing water into H_2 and O_2 can effectively solve environmental problems. In general, the cost of its catalytic equipment and technology has not yet reached the requirements for mass production. Additionally, H_2 is flammable and explosive, its storage represents also a big challenge. Therefore, the research on the generation and storage of H_2 is still the focus of academic research.

Through literature reports and research, it is found that the current research focus on catalytic decomposition of water to H_2 and O_2 is mainly targeted on designing and preparing low-cost, high-efficiency, pollution-free and highly stable catalysts or using PEC water splitting. We have studied and improved the following aspects: (1) Loading an appropriate amount of precious metal on the surface of a conductive carbon support. (2) Preparing

effective non-noble metal materials transition-metal chalcogenides and oxide for both HER and OER. (3) Enhancing H_2 production from electrolyzed water using the phenomenon of plasmon resonance.

Once the research on catalyzing the decomposition of water to produce H_2 can be put into practical application, it will fundamentally change the energy structure of the world.

1.8 References

1. Festus, M. O.; Ogoegbunam, B. Energy Crisis and its Effects on National Development: the Need for Environmental Education in Nigeria. British J. Education 2015, 3, 21-37.
2. Fattouh, B.; Poudineh, R.; West, R. The Rise of Renewables and Energy Transition: What Adaptation Strategy Exists for Oil Companies and Oil-Exporting Countries? Energy Transit 2019, 3 (1-2), 45-58.
3. Staffell, I.; Scamman, D.; Velazquez Abad, A.; Balcombe, P.; Dodds, P. E.; Ekins, P.; Shah, N.; Ward, K. R. The Role of Hydrogen and Fuel Cells in the Global Energy System. Energy Environ. Sci. 2019, 12 (2), 463-491.
4. Ren, X.; Lv, Q.; Liu, L.; Liu, B.; Wang, Y.; Liu, A.; Wu, G. Current Progress of Pt and Pt-Based Electrocatalysts Used for Fuel Cells. Sustainable Energy Fuels 2020, 4 (1), 15-30.
5. Sinigaglia, T.; Lewiski, F.; Santos Martins, M. E.; Mairesse Siluk, J. C. Production, Storage, Fuel Stations of Hydrogen and Its Utilization in Automotive Applications-A Review. Inter. J. Hydrogen Energy 2017, 42 (39), 24597-24611.
6. Cipriani, G.; Di Dio, V.; Genduso, F.; La Cascia, D.; Liga, R.; Miceli, R.; Ricco Galluzzo, G. Perspective on Hydrogen Energy Carrier and Its Automotive Applications. Inter. J. Hydrogen Energy 2014, 39 (16), 8482-8494.
7. Kreith, F.; West, R. Fallacies of a Hydrogen Economy: A Critical Analysis of Hydrogen Production and Utilization. J. Energy Resour. Technol. 2004, 126 (4), 249.

8. Shiva Kumar, S.; Himabindu, V. Hydrogen Production by PEM Water Electrolysis-A Review. Mater. Sci. Energy Technol. 2019, 2 (3), 442-454.
9. Mansilla, C.; Bourasseau, C.; Cany, C.; Guinot, B.; Le Duigou, A.; Lucchese, P. Hydrogen Applications: Overview of the Key Economic Issues and Perspectives. In Hydrogen Supply Chains, Elsevier 2018, 271–292.
10. Stambouli, A. B. Fuel Cells: The Expectations for an Environmental-Friendly and Sustainable Source of Energy. Renew. Sust. Energy Rev. 2011, 15 (9), 4507-4520.
11. Sengodan, S.; Lan, R.; Humphreys, J.; Du, D.; Xu, W.; Wang, H.; Tao, S. Advances in Reforming and Partial Oxidation of Hydrocarbons for Hydrogen Production and Fuel Cell Applications. Renew. Sust. Energy Rev. 2018, 82, 761–780.
12. Jain, I. P. Hydrogen the Fuel for 21st Century. Inter. J. Hydrogen Energy 2009, 34 (17), 7368-7378.
13. Momirlan, M.; Veziroglu, T.N. Current status of hydrogen energy. Renew. Sustain. Energy Rev. 2002, 6, 141-179.
14. Holladay, J. D.; Hu, J.; King, D. L.; Wang, Y., An overview of hydrogen production technologies. Catal. Today 2009, 139, 244-260.
15. Momirlan, M.; Veziroglu, T. Recent directions of world hydrogen production. Renew. Sustain. Energy Rev. 1999, 3, 219-231.
16. Yang, W.; Prabhakar, R. R.; Tan, J.; Tilley, S. D.; Moon, J. Strategies for Enhancing the Photocurrent, Photovoltage, and Stability of Photoelectrodes for Photoelectrochemical Water Splitting. Chem. Soc. Rev. 2019, 48 (19), 4979-5015.
17. Maldonado, M. I.; Saggioroc, E.; Perald, J.; Rodríguez-Castellóne, E.; Jiménez-Jiméneze, J.; Malato, S. Hydrogen generation by irradiation of commercial CuO + TiO_2 mixtures at solar pilot plant scale and in presence of organic electron donors. Appl. Catal. B 2019, 257, 117890.

18. Melis, A. Photosynthesis-to-Fuels: From Sunlight to Hydrogen, Isoprene, and Botryococcene Production. Energy Environ. Sci. 2012, 5 (2), 5531-5539.
19. Ahmad, H.; Kamarudin, S. K.; Minggu, L. J.; Kassim, M. Hydrogen from Photo-Catalytic Water Splitting Process: A Review. Renew. Sustain. Energy Rev. 2015, 43, 599-610.
20. Krishnan, A.; Beena, S.; Chandran, M. Fabrication and Evaluation of CeO_2-Fe_2O_3 Mixed Oxide for Hydrogen Evolution by Photo Water Splitting Reaction under Visible Light Irradiation. Mater. Today: Proc. 2019, 18, 4968-4976.
21. Yang, Q.; Dong, L.; Su, R.; Hu, B.; Wang, Z.; Jin, Y.; Wang, Y.; Besenbacher, F.; Dong, M. Nanostructured Heterogeneous Photo-Catalysts for Hydrogen Production and Water Splitting: A Comprehensive Insight. Appl. Mater. Today 2019, 17, 159-182.
22. Liu, L.; Corma, A. Metal Catalysts for Heterogeneous Catalysis: From Single Atoms to Nanoclusters and Nanoparticles. Chem. Rev. 2018, 118 (10), 4981-5079.
23. Tian, B.; Tian, B.; Smith, B.; Scott, M. C.; Hua, R.; Lei, Q.; Tian, Y. Supported Black Phosphorus Nanosheets as Hydrogen-Evolving Photocatalyst Achieving 5.4% Energy Conversion Efficiency at 353 K. Nat. Commun. 2018, 9 (1), 1397.
24. Shen, Y.; Cao, Z.; Xiao, Z. An Efficient Support-Free Nanoporous Co Catalyst for Reverse Water-Gas Shift Reaction. Catalysts 2019, 9 (5), 423.
25. Kim, H.; Kim, H.; Weon, S.; Moon, G.; Kim, J.-H.; Choi, W. Robust Co-Catalytic Performance of Nanodiamonds Loaded on WO_3 for the Decomposition of Volatile Organic Compounds under Visible Light. ACS Catal. 2016, 6 (12), 8350-8360.
26. Rosen, M. A.; Koohi-Fayegh, S. The Prospects for Hydrogen as an Energy Carrier: An Overview of Hydrogen Energy and Hydrogen Energy Systems. Energy Ecol. Environ. 2016, 1 (1), 10-29.

27. Tuller, H. L. Solar to Fuels Conversion Technologies: A Perspective. Mater. Renew. Sustain. Energy 2017, 6 (1), 3.
28. Rao, C. N. R.; Dey, S. Solar Thermochemical Splitting of Water to Generate Hydrogen. Proc. Natl. Acad. Sci. USA 2017, 114 (51), 13385-13393.
29. An, S. The Reaction Mechanisms of H_2S Decomposition into Hydrogen and Sulfur: Application of Classical and Biological Thermodynamics. J. Thermodyn. Catal. 2017, 08 (02), 1000186.
30. Mukherjee, S.; Devaguptapu, S. V.; Sviripa, A.; Lund, C. R. F.; Wu, G. Low-Temperature Ammonia Decomposition Catalysts for Hydrogen Generation. Appl. Catal. B 2018, 226, 162-181.
31. Choudhary, V. R.; Banerjee, S.; Rajput, A. M. Continuous Production of H_2 at Low Temperature from Methane Decomposition over Ni-Containing Catalyst Followed by Gasification by Steam of the Carbon on the Catalyst in Two Parallel Reactors Operated in Cyclic Manner. J. Catal. 2001, 198 (1), 136-141.
32. Fountaine, K. T.; Lewerenz, H. J.; Atwater, H. A. Efficiency Limits for Photoelectrochemical Water-Splitting. Nat. Commun. 2016, 7 (1), 13706.
33. Varadhan, P.; Fu, H.-C.; Kao, Y.-C.; Horng, R.-H.; He, J.-H. An Efficient and Stable Photoelectrochemical System with 9% Solar-to-Hydrogen Conversion Efficiency via InGaP/GaAs Double Junction. Nat. Commun. 2019, 10 (1), 5282.
34. Hossain, A.; Sakthipandi, K.; Atique Ullah, A. K. M.; Roy, S. Recent Progress and Approaches on Carbon-Free Energy from Water Splitting. Nano-Micro Lett. 2019, 11 (1), 103.
35. Park, K.; Kim, Y. J.; Yoon, T.; David, S.; Song, Y. M. A Methodological Review on Material Growth and Synthesis of Solar-Driven Water Splitting Photoelectrochemical Cells. RSC Adv. 2019, 9 (52), 30112-30124.

36. Hosseini, S. E.; Wahid, M. A. Hydrogen Production from Renewable and Sustainable Energy Resources: Promising Green Energy Carrier for Clean Development. Renew. Sustain. Energy Rev. 2016, 57, 850-866.
37. Møller, K. T.; Jensen, T. R.; Akiba, E.; Li, H. Hydrogen - A Sustainable Energy Carrier. Prog. Nat. Sci. 2017, 27 (1), 34-40.
38. Staffell, I.; Scamman, D.; Velazquez Abad, A.; Balcombe, P.; Dodds, P. E.; Ekins, P.; Shah, N.; Ward, K. R. The Role of Hydrogen and Fuel Cells in the Global Energy System. Energy Environ. Sci. 2019, 12 (2), 463-491.
39. Conte, M.; Di Mario, F.; Iacobazzi, A.; Mattucci, A.; Moreno, A.; Ronchetti, M. Hydrogen as Future Energy Carrier: The ENEA Point of View on Technology and Application Prospects. Energies 2009, 2 (1), 150-179.
40. Eppinger, J.; Huang, K.-W. Formic Acid as a Hydrogen Energy Carrier. ACS Energy Lett. 2017, 2 (1), 188-195.
41. Ji, Y.; Yang, L.; Ren, X.; Cui, G.; Xiong, X.; Sun, X. Full Water Splitting Electrocatalyzed by $NiWO_4$ Nanowire Array. ACS Sustainable Chem. Eng. 2018, 6, 9555–9559.
42. Zeng, L.; Sun, K.; Chen, Y.; Liu, Z.; Chen, Y.; Pan, Y.; Zhao, R.; Liu, Y.; Liu, C. Neutral-PH Overall Water Splitting Catalyzed Efficiently by a Hollow and Porous Structured Ternary Nickel Sulfoselenide Electrocatalyst. J. Mater. Chem. A 2019, 7 (28), 16793-16802.
43. Liu, Z.; Tan, H.; Liu, D.; Liu, X.; Xin, J.; Xie, J.; Zhao, M.; Song, L.; Dai, L.; Liu, H. Promotion of Overall Water Splitting Activity Over a Wide pH Range by Interfacial Electrical Effects of Metallic NiCo-Nitrides Nanoparticle/$NiCo_2O_4$ Nanoflake/Graphite Fibers. Adv. Sci. 2019, 6 (5), 1801829.

44. Liang, K.; Guo, L.; Marcus, K.; Zhang, S.; Yang, Z.; Perea, D. E.; Zhou, L.; Du, Y.; Yang, Y. Overall Water Splitting with Room-Temperature Synthesized NiFe Oxyfluoride Nanoporous Films. ACS Catal. 2017, 7 (12), 8406-8412.

45. An, Y.; Xu, B.; Liu, Y.; Wang, Z.; Wang, P.; Dai, Y.; Qin, X.; Zhang, X.; Huang, B. Photocatalytic Overall Water Splitting over MIL-125(Ti) upon CoPi and Pt Co-Catalyst Deposition. ChemistryOpen 2017, 6 (6), 701-705.

46. Baker, M.; Constantinides, G.; Polychronopoulou, K.; Rebholz, C.; Gupta, R. Electrodeposited Nanostructured $CoFe_2O_4$ for Overall Water Splitting and Supercapacitor Applications. Catalysts 2019, 9 (2), 176.

47. Wu, S.; Shen, Y.; Gao, X.; Ma, Y.; Zhou, Z. Novel Two-Dimensional Photocatalyst SnN_3 for Overall Water Splitting with Enhanced Visible-Light Absorption. Nanoscale 2019, 11, 18628-18639.

48. Arzi, Z.; Yehudai, N.; Halabi, M.; Gal, N.; Hadari, N.; Cohen, C.; Rothschild, A.; Grader, G. S. Decoupled Hydrogen and Oxygen Evolution by a Two-Step Electrochemical-Chemical Cycle for Efficient Overall Water Splitting. Nat. Energy 2019, 4 (9), 786-795.

49. Zhu, Y.; Zhou, W.; Zhong, Y.; Bu, Y.; Chen, X.; Zhong, Q.; Liu, M.; Shao, Z. A Perovskite Nanorod as Bifunctional Electrocatalyst for Overall Water Splitting. Adv. Energy Mater. 2017, 7 (8), 1602122.

50. Pang, L.; Barras, A.; Zhang, Y.; Amin, M. A.; Addad, A.; Szunerits, S.; Boukherroub, R. CoO Promoted the catalytic Activity of Nitrogen-Doped MoS_2 Supported on Carbon Fibers for Overall Water Splitting. ACS Appl. Mater. Interfaces 2019, 11, 35, 31889-31898.

51. Yan, C.; Wang, Y.; Du, H.; Zhu, L.; Jiang, T.; Jiang, H.; Wu, H.; Wang, B. Solar Thermal Electrochemical Process (STEP) action to biomass: Solar thermo-coupled

electrochemical synergy for efficient breaking of biomass to biofuels and hydrogen. Energy Convers. Manage. 2019, 180, 1249-1257.

52. Li, G.; Gao, X. Low-Cost Counter-Electrode Materials for Dye-Sensitized and Perovskite Solar Cells. Adv. Mater. 2020, 32, 1806478.
53. Yamada, T.; Domen, K. Development of Sunlight Driven Water Splitting Devices towards Future Artificial Photosynthetic Industry. Chem. Eng. J. 2018, 2 (3), 36.
54. Liu, H.; Huang, Z.; Liu, K.; Hu, X.; Zhou, J. Interfacial Solar-to-Heat Conversion for Desalination. Adv. Energy Mater. 2019, 9 (21), 1900310.
55. Shang, M.; Li, N.; Zhang, S.; Zhao, T.; Zhang, C.; Liu, C.; Li, H.; Wang, Z. Full-Spectrum Solar-to-Heat Conversion Membrane with Interfacial Plasmonic Heating Ability for High-Efficiency Desalination of Seawater. ACS Appl. Energy Mater. 2018, 1 (1), 56-61.
56. Meir, S.; Stephanos, C.; Geballe, T. H.; Mannhart, J. Highly-Efficient Thermoelectronic Conversion of Solar Energy and Heat into Electric Power. J. Renew. Sustain. Energy 2013, 5 (4), 043127.
57. Lee, K.; Lee, J.; Mazor, B. A.; Forrest, S. R. Transforming the Cost of Solar-to-Electrical Energy Conversion: Integrating Thin-Film GaAs Solar Cells with Non-Tracking Mini-Concentrators. Light Sci. Appl. 2015, 4 (5), e288-e288.
58. Vijayakumar, M.; Adduru, J.; Rao, T. N.; Karthik, M. Conversion of Solar Energy into Electrical Energy Storage: Supercapacitor as an Ultrafast Energy-Storage Device Made from Biodegradable Agar-Agar as a Novel and Low-Cost Carbon Precursor. Global Challenges 2018, 2 (10), 1800037.
59. Hasselman, G. M.; Watson, D. F.; Stromberg, J. R.; Bocian, D. F.; Holten, D.; Lindsey, J. S.; Meyer, G. J. Theoretical Solar-to-Electrical Energy-Conversion Efficiencies of

Perylene-Porphyrin Light-Harvesting Arrays. J. Phys. Chem. B 2006, 110 (50), 25430-25440.

60. Meyer, T. J. Chemical approaches to artificial photosynthesis. Acc. Chem. Res. 1989, 22, 5, 163-170.
61. Chen, M.; Blankenship, R. E. Expanding the solar spectrum used by photosynthesis. Trends in Plant Sci. 2011, 16, 427-431.
62. Lee, Y. W.; Boonmongkolras, P.; Son, E. J.; Kim, J.; Lee, S. H.; Kuk, S. K.; Ko, J. W.; Shin, B.; Park, C. B. Unbiased Biocatalytic Solar-to-Chemical Conversion by FeOOH/$BiVO_4$/Perovskite Tandem Structure. Nat. Commun. 2018, 9 (1), 4208.
63. Lassen, L. M.; Nielsen, A. Z.; Ziersen, B.; Gnanasekaran, T.; Møller, B. L.; Jensen, P. E. Redirecting Photosynthetic Electron Flow into Light-Driven Synthesis of Alternative Products Including High-Value Bioactive Natural Compounds. ACS Synth. Biol. 2014, 3, 1-12.
64. Kim, S.; Nguyen, N.; Bark, C. Ferroelectric Materials: A Novel Pathway for Efficient Solar Water Splitting. Appl. Sci. 2018, 8 (9), 1526.
65. Yu, M.; McCulloch, W. D.; Huang, Z.; Trang, B. B.; Lu, J.; Amine, K.; Wu, Y. Solar-Powered Electrochemical Energy Storage: An Alternative to Solar Fuels. J. Mater. Chem. A 2016, 4 (8), 2766-2782.
66. Chen, X.; Zhang, Z.; Chi, L.; Nair, A. K.; Shangguan, W.; Jiang, Z. Recent Advances in Visible-Light-Driven Photoelectrochemical Water Splitting: Catalyst Nanostructures and Reaction Systems. Nano-Micro Lett. 2016, 8 (1), 1-12.
67. Kim, J. H.; Hansora, D.; Sharma, P.; Jang, J.-W.; Lee, J. S. Toward Practical Solar Hydrogen Production - an Artificial Photosynthetic Leaf-to-Farm Challenge. Chem. Soc. Rev. 2019, 48 (7), 1908-1971.

68. Aroutiounian, V. M.; Arakelyan, V. M.;Shahnazaryan, G. E. Metal oxide photoelectrodes for hydrogen generation using solar radiation-driven water splitting. Solar Energy 2005, 78, 581-592.
69. Ueno, K.; Oshikiri, T.; Shi, X.; Zhong, Y.; Misawa, H. Plasmon-Induced Artificial Photosynthesis. Interface Focus 2015, 5 (3), 20140082.
70. Minegishi, T.; Nishimura, N.; Kubota, J.; Domen, K. Photoelectrochemical properties of $LaTiO_2N$ electrodes prepared by particle transfer for sunlight-driven water splitting. Chem. Sci. 2013, 4(3), 1120.
71. Rongé, J.; Bosserez, T.; Huguenin, L.; Dumortier, M.; Haussener, S.; Martens, J. A. Solar Hydrogen Reaching Maturity. Oil Gas Sci. Technol. -Rev. IFP Energies nouvelles 2015, 70 (5), 863-876.
72. Hassan, M. A.; Kim, M.-W.; Johar, M. A.; Waseem, A.; Kwon, M.-K.; Ryu, S.-W. Transferred Monolayer MoS_2 onto GaN for Heterostructure Photoanode: Toward Stable and Efficient Photoelectrochemical Water Splitting. Sci. Rep. 2019, 9 (1), 20141.
73. Jacobsson, T. J. Photoelectrochemical Water Splitting: An Idea Heading towards Obsolescence. Energy Environ. Sci. 2018, 11 (8), 1977-1979.
74. Jiang, C.; Moniz, S. J. A.; Wang, A.; Zhang, T.; Tang, J. Photoelectrochemical Devices for Solar Water Splitting-Materials and Challenges. Chem. Soc. Rev. 2017, 46 (15), 4645-4660.
75. Liu, M.; Nam, C.-Y.; Black, C. T.; Kamcev, J.; Zhang, L. Enhancing Water Splitting Activity and Chemical Stability of Zinc Oxide Nanowire Photoanodes with Ultrathin Titania Shells. J. Phys. Chem. C 2013, 117 (26), 13396-13402.
76. Liu, R.; Zheng, Z.; Spurgeon, J.; Yang, X. Enhanced photoelectrochemical water-splitting performance of semiconductors by surface passivation layers. Energy Environ. Sci. 2014, 7(8), 2504-2517.

77. Su, F.; Wang, T.; Lv, R.; Zhang, J.; Zhang, P.; Lu, J.; Gong, J. Dendritic Au/TiO_2 nanorod arrays for visible-light driven photoelectrochemical water splitting. Nanoscale 2013, 5, 9001.

78. Wang, Z.; Qi, Y.; Ding, C.; Fan, D.; Liu, G.; Zhao, Y.; Li, C. Insight into the Charge Transfer in Particulate Ta_3N_5 Photoanode with High Photoelectrochemical Performance. Chem. Sci. 2016, 7 (7), 4391-4399.

79. Yang, J.; Wang, D.; Han, H.; Li, C. Roles of Cocatalysts in Photocatalysis and Photoelectrocatalysis. Acc. Chem. Res. 2013, 46 (8), 1900-1909.

80. Faraji, M.; Yousefi, M.; Yousefzadeh, S.; Zirak, M.; Naseri, N.; Jeon, T. H.; Choi, W.; Moshfegh, A. Z. Two-Dimensional Materials in Semiconductor Photoelectrocatalytic Systems for Water Splitting. Energy Environ. Sci. 2019, 12 (1), 59-95.

81. Lee, D. K.; Lee, D.; Lumley, M. A.; Choi, K.-S. Progress on Ternary Oxide-Based Photoanodes for Use in Photoelectrochemical Cells for Solar Water Splitting. Chem. Soc. Rev. 2019, 48 (7), 2126-2157.

82. Dau, H.; Limberg, C.; Reier, T.; Risch, M.; Roggan, S.; Strasser, P. The Mechanism of Water Oxidation: From Electrolysis via Homogeneous to Biological Catalysis. ChemCatChem 2010, 2 (7), 724-761.

83. Xu, X.-T.; Pan, L.; Zhang, X.; Wang, L.; Zou, J.-J. Rational Design and Construction of Cocatalysts for Semiconductor-Based Photo-Electrochemical Oxygen Evolution: A Comprehensive Review. Adv. Sci. 2019, 6 (2), 1801505.

84. Ray, K.; Heims, F.; Schwalbe, M.; Nam, W. High-Valent Metal-O_{xo} Intermediates in Energy Demanding Processes: From Dioxygen Reduction to Water Splitting. Curr. Opin. Chem. Biol. 2015, 25, 159-171.

85. Zeng, K.; Zhang, D. Recent Progress in Alkaline Water Electrolysis for Hydrogen Production and Applications. Prog. Energy Combust. Sci. 2010, 36 (3), 307-326.

86. Yan, Y.; Xia, B. Y.; Zhao, B.; Wang, X. A Review on Noble-Metal-Free Bifunctional Heterogeneous Catalysts for Overall Electrochemical Water Splitting. J. Mater. Chem. A 2016, 4 (45), 17587-17603.
87. Li, J.; Zheng, G. One-Dimensional Earth-Abundant Nanomaterials for Water-Splitting Electrocatalysts. Adv. Sci. 2017, 4 (3), 1600380.
88. Li, W.; Gao, X.; Xiong, D.; Xia, F.; Liu, J.; Song, W.-G.; Xu, J.; Thalluri, S. M.; Cerqueira, M. F.; Fu, X.; Liu, L. Vapor-Solid Synthesis of Monolithic Single-Crystalline CoP Nanowire Electrodes for Efficient and Robust Water Electrolysis. Chem. Sci. 2017, 8 (4), 2952-2958.
89. Alfaifi, B. Y.; Ullah, H.; Alfaifi, S.; Tahir, A. A.; Mallick, T. K. Photoelectrochemical Solar Water Splitting: From Basic Principles to Advanced Devices. Veruscript Funct. Nanomater. 2018, 2, BDJOC3.
90. Yan, Y.; Xia, B. Y.; Zhao, B.; Wang, X. A Review on Noble-Metal-Free Bifunctional Heterogeneous Catalysts for Overall Electrochemical Water Splitting. J. Mater. Chem. A 2016, 4 (45), 17587-17603.
91. Ohlmann, J.; Sanchez, J. F. M.; Lackner, D.; Förster, P.; Steiner, M.; Fallisch, A.; Dimroth, F. Recent Development in Direct Generation of Hydrogen Using Multi-Junction Solar Cells. Freiburg, Germany, 2016, 080004.
92. Kageshima, Y.; Shinagawa, T.; Kuwata, T.; Nakata, J.; Minegishi, T.; Takanabe, K.; Domen, K. A Miniature Solar Device for Overall Water Splitting Consisting of Series-Connected Spherical Silicon Solar Cells. Sci. Rep. 2016, 6 (1), 24633.
93. Kang, Z.; Guo, H.; Wu, J.; Sun, X.; Zhang, Z.; Liao, Q.; Zhang, S.; Si, H.; Wu, P.; Wang, L.; Zhang, Y. Engineering an Earth-Abundant Element-Based Bifunctional Electrocatalyst for Highly Efficient and Durable Overall Water Splitting. Adv. Funct. Mater. 2019, 29 (9), 1807031.

94. Sharifi, T.; Gracia-Espino, E.; Jia, X.; Sandström, R.; Wågberg, T. Comprehensive Study of an Earth-Abundant Bifunctional 3D Electrode for Efficient Water Electrolysis in Alkaline Medium. ACS Appl. Mater. Interfaces 2015, 7 (51), 28148-28155.

95. Du, P.; Eisenberg, R. Catalysts Made of Earth-Abundant Elements (Co, Ni, Fe) for Water Splitting: Recent Progress and Future Challenges. Energy Environ. Sci. 2012, 5 (3), 6012.

96. Katz, M. J.; Riha, S. C.; Jeong, N. C.; Martinson, A. B. F.; Farha, O. K.; Hupp, J. T. Toward Solar Fuels: Water Splitting with Sunlight and "Rust". Coord. Chem. Rev. 2012, 256, 2521-2529.

97. Li, C.; Xu, Y.; Yang, D.; Qian, X.; Chai, X.; Wang, Z.; Li, X.; Wang, l.; Wang, H. Boosting Electrocatalytic Activities of Pt-Based Mesoporous Nanoparticles for Overall Water Splitting by a Facile Ni, P Co-Incorporation Strategy. ACS Sustainable Chem. Eng. 2019, 7, 10, 9709-9716

98. Creus, J.; De Tovar, J.; Romero, N.; García-Antón, J.; Philippot, K.; Bofill, R.; Sala, X. Ruthenium Nanoparticles for Catalytic Water Splitting. ChemSusChem. 2019, 12, 2493.

99. Sarkar, S.; Peter, S. C. An overview on Pd-based electrocatalysts for the hydrogen evolution reaction. Inorg. Chem. Front. 2018, 5, 2060-2080.

100. Li, Y.; Chen, J.; Cai, P.; Wen, Z. An Electrochemically Neutralized Energy-Assisted Low-Cost Acid-Alkaline Electrolyzer for Energy-Saving Electrolysis Hydrogen Generation. J. Mater. Chem. A 2018, 6 (12), 4948-4954.

101. Choi, W.; Choudhary, N.; Han, G. H.; Park, J.; Akinwande, D.; Lee, Y. H. Recent Development of Two-Dimensional Transition Metal Dichalcogenides and Their Applications. Mater. Today 2017, 20 (3), 116-130.

102. Liang, C.; Zou, P.; Nairan, A.; Zhang, Y.; Liu, J.; Liu, K.; Hu, S.; Kang, F.; Fan, H. J.; Yang, Cheng. Exceptional performance of hierarchical Ni-Fe oxyhydroxide@NiFe alloy

nanowire array electrocatalysts for large current density water splitting. Energy Environ. Sci. 2020, 13, 86-95.

103. Vogiatzis, K. D.; Polynski, M. V.; Kirkland, J. K.; Townsend, J.; Hashemi, A.; Liu, C.; Pidko, E. A. Computational Approach to Molecular Catalysis by 3d Transition Metals: Challenges and Opportunities. Chem. Rev. 2019, 119 (4), 2453-2523.

104. Labhasetwar, N.; Saravanan, G.; Kumar Megarajan, S.; Manwar, N.; Khobragade, R.; Doggali, P.; Grasset, F. Perovskite-Type Catalytic Materials for Environmental Applications. Sci. Technol. Adv. Mater. 2015, 16 (3), 036002.

105. Kadam, S. R.; Enyashin, A.; Houben, L.; Bar-Ziv, R.; Bar Sadan, M. Ni-WSe_2 nanostructures as efficient catalysts for electrochemical hydrogen evolution reaction (HER) in acidic and alkaline media. J. Mater. Chem. A 2020,8, 1403-1416.

106. Danilovic, N.; Subbaraman, R.; Strmcnik, D.; Stamenkovic, V.; Markovic, N. Electrocatalysis of the HER in Acid and Alkaline Media. J. Serb. Chem. Soc. 2013, 78 (12), 2007-2015.

107. Zeng, M.; Li, Y. Recent Advances in Heterogeneous Electrocatalysts for Hydrogen Evolution Reaction. J. Mater. Chem. A 2015, 3 (29), 14942-14962.

108. Dubouis, N.; Grimaud, A. The Hydrogen Evolution Reaction: From Material to Interfacial Descriptors. Chem. Sci. 2019, 10 (40), 9165-9181.

109. Kucernak, A. R.; Zalitis, C. General Models for the Electrochemical Hydrogen Oxidation and Hydrogen Evolution Reactions: Theoretical Derivation and Experimental Results under Near Mass-Transport Free Conditions. J. Phys. Chem. C 2016, 120 (20), 10721-10745.

110. De Chialvo; M. R. G.; Chialvo, A. C. Hydrogen evolution reaction: Analysis of the Volmer-Heyrovsky-Tafel mechanism with a generalized adsorption model. J. Electroanaly. Chem. 1994, 372, 209-223.

111. Sapountzi, F. M.; Gracia, J. M.; Weststrate, C. J.; Kees-J.; Fredriksson, H. O. A.; Niemantsverdriet, J. W. (Hans). Electrocatalysts for the Generation of Hydrogen, Oxygen and Synthesis Gas. Prog. Energy Combust. Sci. 2017, 58, 1-35.

112. Mahmood, N.; Yao, Y.; Zhang, J.-W.; Pan, L.; Zhang, X.; Zou, J.-J. Electrocatalysts for Hydrogen Evolution in Alkaline Electrolytes: Mechanisms, Challenges, and Prospective Solutions. Adv. Sci. 2018, 5 (2), 1700464.

113. Colli, A. N.; Girault, H. H.; Battistel, A. Non-Precious Electrodes for Practical Alkaline Water Electrolysis. Materials 2019, 12 (8), 1336.

114. Quaino, P.; Juarez, F.; Santos, E.; Schmickler, W. Volcano plots in hydrogen electrocatalysis-uses and abuses. Beilstein J. Nanotechnology 2014, 5, 846–854.

115. Burke, M. S.; Enman, L. J.; Batchellor, A. S.; Zou, S.; Boettcher, S. W. Oxygen Evolution Reaction Electrocatalysis on Transition Metal Oxides and (Oxy)Hydroxides: Activity Trends and Design Principles. Chem. Mater. 2015, 27 (22), 7549-7558.

116. Matsumoto, Y.; Sato, E. Electrocatalytic Properties of Transition Metal Oxides for Oxygen Evolution Reaction. Mater. Chem. Phys. 1986, 14 (5), 397-426.

117. Lu, Z.; Wang, H.; Kong, D.; Yan, K.; Hsu, P.-C.; Zheng, G.; Yao, H.; Liang, Z.; Sun, X.; Cui, Y. Electrochemical Tuning of Layered Lithium Transition Metal Oxides for Improvement of Oxygen Evolution Reaction. Nat. Commun. 2014, 5 (1), 4345.

118. Long, X.; Xiao, S.; Wang, Z.; Zheng, X.; Yang, S. Co Intake Mediated Formation of Ultrathin Nanosheets of Transition Metal LDH-an Advanced Electrocatalyst for Oxygen Evolution Reaction. Chem. Commun. 2015, 51 (6), 1120-1123.

119. Morales-Guio, C. G.; Liardet, L.; Hu, X. Oxidatively Electrodeposited Thin-Film Transition Metal (Oxy)Hydroxides as Oxygen Evolution Catalysts. J. Am. Chem. Soc. 2016, 138 (28), 8946-8957.

120. Burke, M. S.; Zou, S.; Enman, L. J.; Kellon, J. E.; Gabor, C. A.; Pledger, E.; Boettcher, S. W. Revised Oxygen Evolution Reaction Activity Trends for First-Row Transition-Metal (Oxy)Hydroxides in Alkaline Media. J. Phys. Chem. Lett. 2015, 6 (18), 3737-3742.

121. Grimaud, A.; May, K. J.; Carlton, C. E.; Lee, Y.-L.; Risch, M.; Hong, W. T.; Zhou, J.; Shao-Horn, Y. Double Perovskites as a Family of Highly Active Catalysts for Oxygen Evolution in Alkaline Solution. Nat. Commun. 2013, 4 (1), 2439.

122. Suntivich, J.; May, K. J.; Gasteiger, H. A.; Goodenough, J. B.; Shao-Horn, Y. A Perovskite Oxide Optimized for Oxygen Evolution Catalysis from Molecular Orbital Principles. Science 2011, 334 (6061), 1383-1385.

123. Rincón, R. A.; Masa, J.; Mehrpour, S.; Tietz, F.; Schuhmann, W. Activation of Oxygen Evolving Perovskites for Oxygen Reduction by Functionalization with Fe-N_x/C Groups. Chem. Commun. 2014, 50 (94), 14760-14762.

124. Fei, H.; Dong, J.; Arellano-Jiménez, M. J.; Ye, G.; Dong Kim, N.; Samuel, E. L. G.; Peng, Z.; Zhu, Z.; Qin, F.; Bao, J.; Yacaman, M. J.; Ajayan, P. M.; Chen, D.; Tour, J. M. Atomic Cobalt on Nitrogen-Doped Graphene for Hydrogen Generation. Nat. Commun. 2015, 6 (1), 8668.

125. Duan, S.; Du, Z.; Fan, H.; Wang, R. Nanostructure Optimization of Platinum-Based Nanomaterials for Catalytic Applications. Nanomaterials 2018, 8 (11), 949.

126. Bai, L.; Ouyang, Y.; Song, J.; Xu, Z.; Liu, W.; Hu, J.; Wang, Y.; Yuan, F. Synthesis of Metallic Nanocrystals: From Noble Metals to Base Metals. Materials 2019, 12 (9), 1497.

127. Rioux, R. M.; Song, H.; Hoefelmeyer, J. D.; Yang, P.; Somorjai, G. A. High-Surface-Area Catalyst Design: Synthesis, Characterization, and Reaction Studies of Platinum Nanoparticles in Mesoporous SBA-15 Silica. J. Phys. Chem. B 2005, 109 (6), 2192-2202.

128. Lu, Q.; Hutchings, G. S.; Yu, W.; Zhou, Y.; Forest, R. V.; Tao, R.; Rosen, J.; Yonemoto, B. T.; Cao, Z.; Zheng, H.; Xiao, J. Q.; Jiao, F.; Chen, J. G. Highly Porous Non-Precious Bimetallic Electrocatalysts for Efficient Hydrogen Evolution. Nat. Commun. 2015, 6 (1), 6567.

129. Lin, J.; Wang, P.; Wang, H.; Li, C.; Si, X.; Qi, J.; Cao, J.; Zhong, Z.; Fei, W.; Feng, J. Defect-Rich Heterogeneous MoS_2/NiS_2 Nanosheets Electrocatalysts for Efficient Overall Water Splitting. Adv. Sci. 2019, 1900246.

130. Khan, A. H.; Ghosh, S.; Pradhan, B.; Dalui, A.; Shrestha, L. K.; Acharya, S.; Ariga, K. Two-Dimensional (2D) Nanomaterials towards Electrochemical Nanoarchitectonics in Energy-Related Applications. BCSJ 2017, 90 (6), 627-648.

131. Theerthagiri, J.; Karuppasamy, K.; Durai, G.; Rana, A.; Arunachalam, P.; Sangeetha, K.; Kuppusami, P.; Kim, H.-S. Recent Advances in Metal Chalcogenides (MX; X = S, Se) Nanostructures for Electrochemical Supercapacitor Applications: A Brief Review. Nanomaterials 2018, 8 (4), 256.

132. Lai, C.-H.; Lu, M. -Y.; Chen, L.-J. Metal sulfide nanostructures: synthesis, properties and applications in energy conversion and storage. J. Mater. Chem. 2012, 22, 19-30.

133. Jeevanandam, J.; Barhoum, A.; Chan, Y. S.; Dufresne, A.; Danquah, M. K. Review on Nanoparticles and Nanostructured Materials: History, Sources, Toxicity and Regulations. Beilstein J. Nanotechnol. 2018, 9, 1050-1074.

134. Ren, Z.; Guo, Y.; Liu, C.-H.; Gao, P.-X. Hierarchically Nanostructured Materials for Sustainable Environmental Applications. Front. Chem. 2013, 1, 1-22.

135. Kobayashia, S.; Trykb, D. A.; Uchidaa, H. Enhancement of hydrogen evolution activity on Pt-skin/Pt_3Co [(111), (100), and (110)] single crystal electrodes. Electrochem. Commun. 2020, 110, 106615.

136. Li, J.; Zhao, T.; Chen, T.; Liu, Y.; Ong, C. N.; Xie, J. Engineering Noble Metal Nanomaterials for Environmental Applications. Nanoscale 2015, 7 (17), 7502-7519.

137. Zhang, Q.; Li, Y.; Kuang, Y.; Jiang, M.; Cai, Z.; Chang, Z.; Pang, Y.; Sun, X. Synthesis and Performance Optimization of Ultrathin Two-Dimensional CoFePt alloy Materials via in-situ Topotactic Conversion for Hydrogen Evolution Reaction. J. Mater. Chem. A 2019, 7, 9517-9522.

138. Kong, W.; Luan, X.; Du, H.; Xia, L.; Qu, F. Enhanced electrocatalytic activity of water oxidation in an alkaline medium via Fe doping in CoS_2 nanosheets. Chem. Commun. 2019, 55, 2469-2472.

139. Dai, X.; Du, K.; Li, Z.; Liu, M.; Ma, Y.; Sun, H.; Zhang, X.; Yang, Y. Co-Doped MoS_2 Nanosheets with the Dominant CoMoS Phase Coated on Carbon as an Excellent Electrocatalyst for Hydrogen Evolution. ACS Appl. Mater. Interfaces 2015, 7, 49, 27242-27253.

140. Wu, L.; Xu, X.; Zhao, Y.; Zhang, K.; Sun, Y.; Wang, T.; Wang, Y; Zhong, W.; Du, Y. Mn doped MoS_2/reduced graphene oxide hybrid for enhanced hydrogen evolution. Appl. Sur. Sci. 2017, 425, 470-477.

141. Jiang, K.; Liu, B.; Luo, M.; Ning, S.; Peng, M.; Zhao, Y.; Lu, Y.-R.; Chan, T.-S.; Groot, F. M. F.; Tan, Y. Single platinum atoms embedded in nanoporous cobalt selenide as electrocatalyst for accelerating hydrogen evolution reaction. Nature Commun. 2019, 10(1), 1743.

142. Shi, Y.; Zhou, Y.; Yang, D.-R.; Xu, W.-X.; Wang, C.; Wang, F.-B.; Xu, J.-J.; Xia, X.-H.; Chen, H.-Y. Energy Level Engineering of MoS_2 by Transition-Metal Doping for Accelerating Hydrogen Evolution Reaction. J. Am. Chem. Soc. 2017, 139, 43, 15479-15485.

143. Wang, Y.; Chen, L.; Yu, X.; Wang, Y.; Zheng, G. Superb Alkaline Hydrogen Evolution and Simultaneous Electricity Generation by Pt-Decorated Ni_3N Nanosheets. Adv. Energy Mater. 2017, 7, 1601390.

144. Oh, A.; Sa, Y. J.; Hwang, H.; Baik, H.; Kim, J.; Kim, B.; Joo, S. H.; Lee, K. Rational design of Pt-Ni-Co ternary alloy nanoframe crystals as highly efficient catalysts toward the alkaline hydrogen evolution reaction. Nanoscale 2016, 8, 16379-16386.

145. Xie, Y.; Cai, J.; Wu, Y.; Zang, Y.; Zheng, X.; Ye, J.; Cui, P.; Niu, S.; Liu, Y.; Zhu, J.; Liu, X.; Wang, G.; Qian, Y. Boosting Water Dissociation Kinetics on Pt-Ni Nanowires by N-Induced Orbital Tuning. Adv. Mater. 2019, 31, 1807780.

146. Zheng, Y.; Jiao Y.; Zhu, Y.; Li, L. H.; Han, Y.; Chen Y.; Jaroniec, M.; Qiao, S-Z. High Electrocatalytic Hydrogen Evolution Activity of an Anomalous Ruthenium Catalyst. J. Am. Chem. Soc. 2016, 138 (49), 16174-16181.

147. Zhang, J.; Liu, P.; Wang, G.; Zhang, P. P.; Zhuang, X. D.; Chen, M. W.; Weidinger, I. M.; Feng, X. L. Ruthenium/Nitrogen-Doped Carbon as an Electrocatalyst for Efficient Hydrogen Evolution in Alkaline Solution. J. Mater. Chem. A 2017, 5 (48), 25314-25318.

148. Zhang, C.; Liu, Y.; Chang, Y.; Lu, Y.; Zhao, S.; Xu, D.; Dai, Z.; Han, M.; Bao, J. Component-Controlled Synthesis of Necklace-Like Hollow Ni_XRu_y Nanoalloys as Electrocatalysts for Hydrogen Evolution Reaction. ACS Appl. Mater. Interfaces 2017, 9 (20), 17326-17336.

149. Wang, J.; Wei, Z.; Mao, S.; Li, H.; Wang, Y. Highly Uniform Ru Nanoparticles over N-Doped Carbon: PH and Temperature-Universal Hydrogen Release from Water Reduction. Energy Environ. Sci. 2018, 11 (4), 800-806.

150. Li, C.; Baek, J.-B. Recent Advances in Noble Metal (Pt, Ru, and Ir)-Based Electrocatalysts for Efficient Hydrogen Evolution Reaction. ACS Omega 2020, 5 (1), 31-40.

151. Mao, J.; He, C. T.; Pei, J.; Chen, W.; He, D.; He, Y.; Zhuang, Z.; Chen, C.; Peng, Q.; Wang, D.; Li, Y. Accelerating water dissociation kinetics by isolating cobalt atoms into ruthenium lattice. Nat. Commun. 2018, 9(1), 4958.

152. Lee, J. W.; Popov, B. N. Ruthenium-Based Electrocatalysts for Oxygen Reduction Reaction-a Review. J. Solid State Electrochem. 2007, 11 (10), 1355-1364.

153. Zeng, L.; Gupta, P.; Chen, Y.; Wang, E.; Ji, L.; Chao, H.; Chen, Z.-S. The Development of Anticancer Ruthenium(ii) Complexes: From Single Molecule Compounds to Nanomaterials. Chem. Soc. Rev. 2017, 46 (19), 5771-5804.

154. Xu, Q.; Liu, Y.; Jiang, H.; Hu, Y.; Liu, H.; Li, C. Unsaturated Sulfur Edge Engineering of Strongly Coupled MoS_2 Nanosheet-Carbon Macroporous Hybrid Catalyst for Enhanced Hydrogen Generation. Adv. Energy Mater. 2019, 9, 1802553.

155. Xiong, W.; Guo, Z.; Li, H.; Zhao, R.; Wang, X. Rational Bottom-Up Engineering of Electrocatalysts by Atomic Layer Deposition: A Case Study of $Fe_xCo_{1-x}S_y$-Based Catalysts for Electrochemical Hydrogen Evolution. ACS Energy Lett. 2017, 2, 2778-2785.

156. Feng, J. X.; Wu, J. Q.; Tong Y. X.; Li, G. R. Efficient Hydrogen Evolution on Cu Nanodots-Decorated Ni_3S_2 Nanotubes by Optimizing Atomic Hydrogen Adsorption and Desorption. J. Am. Chem. Soc. 2018, 140, 610-617.

157. Li, X.; Hao, X.; Abudulaa, A.; Guan, G. Nanostructured catalysts for electrochemical water splitting: current state and prospects. J. Mater. Chem. A 2016, 4, 11973-12000.

158. Chen, Z.; Duan, X.; Wei, W.; Wang S.; Ni, B. Recent advances in transition metal-based electrocatalysts for alkaline hydrogen evolution. J. Mater. Chem. A 2019, 7, 14971-15005.

159. Sumesh, C. K.; Peter, S. C. Two-dimensional semiconductor transition metal-based chalcogenide based heterostructures for water splitting applications. Dalton Trans. 2019, 48, 12772-12802.

160. Chen, H.; Chen, Z.; Ge, B.; Chi, Z.; Chen, H.; Wu, H.; Cao, C.; Duan, X. General Strategy for Two-Dimensional Transition Metal Dichalcogenides by Ion Exchange. Chem. Mater. 2017, 29, 10019-10026.

161. Jing, Y.; Liu, B.; Zhu, X.; Ouyang, F.; Sun, J.; Zhou, Y. Tunable electronic structure of two-dimensional transition metal chalcogenides for optoelectronic applications. Nannphotonics 2020, 04, https://doi.org/10.1515/nanoph-2019-0574.

162. Tiwari, A.; Kim, D.; Kim, Y.; Lee, H. Highly active and stable layered ternary transition metal chalcogenide for hydrogen evolution reaction. Nano Energy 2016, 28, 366-372.

163. Zhang, J.; Wu, J.; Guo, H.; Chen, W.; Yuan, J.; Martinez, U.; Gupta, G.; Mohite, A.; Ajayan, P. M.; Lou, J. Unveiling Active Sites for the Hydrogen Evolution Reaction on Monolayer MoS_2. Adv. Mater. 2017, 29, 1701955.

164. Gao, G.; Sun, Q.; Du, A. Activating Catalytic Inert Basal Plane of Molybdenum Disulfide to Optimize Hydrogen Evolution Activity via Defect Doping and Strain Engineering. J. Phys. Chem. C 2016, 120 (30), 16761-16766.

165. Zhuo, S.; Xu, Y.; Zhao, W.; Zhang, J.; Zhang, B. Hierarchical Nanosheet-Based MoS_2 Nanotubes Fabricated by an Anion-Exchange Reaction of MoO_3-Amine Hybrid Nanowires. Angew. Chem. Int. Ed. 2013, 52 (33), 8602-8606.

166. Ling, C.; Ouyang, Y.; Shi, L.; Yuan, S.; Chen, Q.; Wang, J. Template-Grown MoS_2 Nanowires Catalyze Hydrogen Evolution Reaction: Ultra-Low Kinetic Barriers with High Active Site Density. ACS Catal. 2017, 7, 8, 5097-5102.

167. Kong, D.; Wang, H.; Cha, J. J.; Pasta, M.; Koski, K. J.; Yao, J.; Cui, Y. Synthesis of MoS_2 and $MoSe_2$ Films with Vertically Aligned Layers. Nano Lett. 2013, 13 (3), 1341-1347.

168. Jayabal, S.; Saranya, G.; Wu, J.; Liu, Y.; Geng, D.; Meng, X. Understanding the High-Electrocatalytic Performance of Two-Dimensional MoS_2 Nanosheets and Their Composite Materials. J. Mater. Chem. A 2017, 5 (47), 24540-24563.

169. Ouyang, Y.; Ling, C.; Chen, Q.; Wang, Z.; Shi, L.; Wang, J. Activating Inert Basal Planes of MoS_2 for Hydrogen Evolution Reaction through the Formation of Different Intrinsic Defects. Chem. Mater. 2016, 28, 4390-4396.

170. Li, H.; Tsai, C.; Koh, A. L.; Cai, L.; Contryman, A. W.; Fragapane, A. H.; Zhao, J.; Han, H. S.; Manoharan, H. C.; Abild-Pedersen, F.; Nørskov, J. K.; Zheng, X. Erratum: Corrigendum: Activating and Optimizing MoS_2 Basal Planes for Hydrogen Evolution through the Formation of Strained Sulphur Vacancies. Nature Mater. 2016, 15 (3), 364-364.

171. Xie, J.; Zhang, J.; Li, S.; Grote, F.; Zhang, X.; Zhang, H.; Wang, R.; Lei, Y.; Pan, B.; Xie, Y. Controllable Disorder Engineering in Oxygen-Incorporated MoS_2 Ultrathin Nanosheets for Efficient Hydrogen Evolution. J. Am. Chem. Soc. 2013, 135 (47), 17881-17888.

172. Voiry, D.; Salehi, M.; Silva, R.; Fujita, T.; Chen, M.; Asefa, T.; Shenoy, V. B.; Eda, G.; Chhowalla, M. Conducting MoS_2 Nanosheets as Catalysts for Hydrogen Evolution Reaction. Nano Lett. 2013, 13 (12), 6222-6227.

173. Li, Y.; Wang, H.; Xie, L.; Liang, Y.; Hong, G.; Dai, H. MoS_2 Nanoparticles Grown on Graphene: An Advanced Catalyst for the Hydrogen Evolution Reaction. J. Am. Chem. Soc. 2011, 133 (19), 7296-7299.

174. Xiao, X.; Tao, L.; Li, M.; Lv, X.; Huang, D.; Jiang, X.; Pan, H.; Wang, M.; Shen, Y. Electronic modulation of transition metal phosphide via doping as efficient and pH-universal electrocatalysts for hydrogen evolution reaction. Chem. Sci. 2018, 9, 1970-1975.

175. Song, J.; Wei, C.; Huang, Z. F.; Liu, C.; Zeng, L.; Wang, X.; Xu, Z. J. A review on fundamentals for designing oxygen evolution electrocatalysts. Chem. Soc. Rev. 2020, 49, 2196-2214.

176. Read, C. G.; Callejas, J. F.; Holder, C. F.; Schaak, R. E. General Strategy for the Synthesis of Transition Metal Phosphide Films for Electrocatalytic Hydrogen and Oxygen Evolution. ACS Appl. Mater. Interfaces 2016, 8, 12798-12803.

177. Yang, Y.; Fei, H.; Ruan, G.; Tour, J. M. Porous cobalt-based thin film as a bifunctional catalyst for hydrogen generation and oxygen generation. Adv. Mater. 2015, 27, 3175-3180.

178. Liu, W.; Hu, E.; Jiang, H.; Xiang, Y.; Weng, Z.; Li, M.; Fan, Q.; Yu, X.; Altman, E. I.; Wang, H. A highly active and stable hydrogen evolution catalyst based on pyrite-structured cobalt phosphosulfide. Nat. Commun. 2016, 7, 10771.

179. Ma, Y.; Han, J.; Wang, M.; Chen, X.; Jia, S. Electrophoretic deposition of graphene-based materials: A review of materials and their applications. J. Materiomics 2018, 4, 108-120.

180. Li, J.; Zhao, Z.; Ma, Y.; Qu, Y. Graphene and Their Hybrid Electrocatalysts for Water Splitting. ChemCatChem 2017, 9, 1554-1568.

181. Ito, Y.; Cong, W.; Fujita, T.; Tang, Z.; Chen, M. High Catalytic Activity of Nitrogen and Sulfur Co-Doped Nanoporous Graphene in the Hydrogen Evolution Reaction. Angew. Chem. Int. Ed. 2015, 54, 2131-2136.

182. Zheng, Y.; Jiao .; Li L. H.; Xing T.; Chen, Y.; Jaroniec, M.; Qiao, S. Z. Toward design of synergistically active carbon-based catalysts for electrocatalytic hydrogen evolution. ACS Nano 2014, 8, 5290-5296.

183. Liu, X.; Zhou, W.; Yang, L.; Li, L.; Zhang, Z.; Ke Y.; Chen, S. Correction: Nitrogen and sulfur co-doped porous carbon derived from human hair as highly efficient metal-free electrocatalysts for hydrogen evolution reactions. J. Mater. Chem. A 2015, 3, 8840-8846.

184. Zhang, B.; Wen, Z.; Ci, S.; Chen J.; He, Z. Nitrogen-doped activated carbon as a metal free catalyst for hydrogen production in microbial electrolysis cells. RSC Adv. 2014, 4, 49161-49164.

185. Cheng, Y.; Tian, Y.; Fan, X.; Liu J.; Yan, C. Boron Doped Multi-walled Carbon Nanotubes as Catalysts for Oxygen Reduction Reaction and Oxygen Evolution Reactionin in Alkaline Media. Electrochim. Acta 2014, 143, 291-296.

186. Paoli, E. A.; Masini, F.; Frydendal, R.; Deiana, D.; Schlaup, C.; Malizia, M.; Hansen, T. W.; Horch, S.; Stephens, I. E. L.; Chorkendorff, Ib. Oxygen evolution on well-characterized mass-selected Ru and RuO_2 nanoparticles. Chem. Sci. 2015, 6, 190-196

187. Reier, T.; Mehtap Oezaslan, M.; Strasser, P. Electrocatalytic Oxygen Evolution Reaction (OER) on Ru, Ir, and Pt Catalysts: A Comparative Study of Nanoparticles and Bulk Materials. ACS Catal. 2012, 2, 8, 1765-1772.

188. Danilovic, N.; Subbaraman, R.; Chang, K. C.; Chang, S. H.; Kang, Y.; Snyder, J.; Paulikas, A. P.; Strmcnik, D.; Kim, Y. T.; Myers, D.; Stamenkovic, V. R.; Markovic, N. M. Using Surface Segregation To Design Stable Ru-Ir Oxides for the Oxygen Evolution Reaction in Acidic Environments. Angew. Chem. Int. Ed. 2014, 53, 14016-14021.

189. Song, F.; Bai, Li.; Moysiadou, A.; Lee, S.; Hu, C.; Liardet, L.; Hu, X. Transition Metal Oxides as Electrocatalysts for the Oxygen Evolution Reaction in Alkaline Solutions: An Application-Inspired Renaissance. J. Am. Chem. Soc. 2018, 140, 25, 7748-7759.

190. Song, F.; Hu, X. Ultrathin cobalt-manganese layered double hydroxide is an efficient oxygen evolution catalyst. J. Am. Chem. Soc. 2014, 136, 16481-4.

191. Gerken, J. B.; McAlpin, J. G.; Chen, J. Y.; Rigsby, M. L.; Casey, W. H.; Britt, R. D.; Stahl, S. S. Electrochemical water oxidation with cobalt-based electrocatalysts from pH 0-14: the thermodynamic basis for catalyst structure, stability, and activity. J. Am. Chem. Soc. 2011, 133, 14431-42.

192. Zhang, Q.; Duan, Z.; Li, M.; Guan, J. Atomic cobalt catalysts for the oxygen evolution reaction. Chem. Commun. 2020, 56, 794-797.

193. Liu, J.; Ji, Y.; Nai, J.; Niu, X.; Luo, Y.; Guo L.;Yang S. Ultrathin amorphous cobalt-vanadium hydr(oxy)oxide catalysts for the oxygen evolution reaction. Energy Environ. Sci. 2018, 11, 1736-1741.

194. Liang, Y.; Li, Y.; Wang, H.; Zhou, J.; Wang, J.; Regier, T.; Dai, H. Co_3O_4 nanocrystals on graphene as a synergistic catalyst for oxygen reduction reaction. Nat. Mater. 2011, 10, 780-786.

195. Wang, B.; Tang, C.; Wang, H. F.; Chen, X.; Cao, R.; Zhang, Q. A Nanosized CoNi Hydroxide@Hydroxysulfide Core-Shell Heterostructure for Enhanced Oxygen Evolution. Adv. Mater. 2019, 31, 1805658.

196. Gu, Y.; Jia, D.; Peng, Y,; Song, S.; Zhao, Y.; Zhang J.; Wang, D. Hierarchical porous Co_3O_4@$CoxFe_{3-x}O_4$ film as an advanced electrocatalyst for oxygen evolution reaction. RSC Adv. 2015, 5, 8882-8886.

197. Shao, M.; Zhang, R.; Li, Z.; Wei, M.; Evans, D. G.; Duan, X. Layered double hydroxides toward electrochemical energy storage and conversion: design, synthesis and applications. Chem. Commun. 2015, 51(88), 15880-15893.

198. Rosa, M.; Bassetto, V. C.; Girault, H.; Lesch, A.; Esposito, V. Assembling Ni-Fe Layered Double Hydroxide 2D Thin Films for Oxygen Evolution Electrodes. ACS Appl. Energy Mater. 2020, 3, 1, 1017-1026.

199. Trotochaud, L.; Young, S. L.; Ranney, J. K.; Boettcher, S. W. Nickel-iron oxyhydroxide oxygen-evolution electrocatalysts: the role of intentional and incidental iron incorporation. J. Am. Chem. Soc. 2014, 136, 6744-6753.

200. Li, Z.; Shao, M.; An, H.; Wang, Z.; Xu, S.; Wei, M.; Evans D. G. Duan, X. Fast electrosynthesis of Fe-containing layered double hydroxide arrays toward highly efficient electrocatalytic oxidation reactions. Chem. Sci. 2015, 6, 6624-6631.

201. Zhou, L.; Guo, M.; Li, Y.; Gu, Q.; Zhang, W.; Li, C.; Xie, F.; Lin, D.; Zheng, Q. One-step synthesis of wire-in-plate nanostructured materials made of CoFe-LDH nanoplates coupled with $Co(OH)_2$ nanowires grown on a Ni foam for a high-efficiency oxygen evolution reaction. Chem. Commun. 2019, 55, 4218-4221.

202. Yoon, S.; Yun, J. Y.; Lim, J. M.; Yoo, M. Enhanced electrocatalytic properties of electrodeposited amorphous cobalt-nickel hydroxide nanosheets on nickel foam by the formation of nickel nanocones for the oxygen evolution reaction. J. Alloy. Comp. 2017, 693, 964-969.

203. Yu, X.; Zhang, M.; Yuan W.; Shi, G. A high-performance three-dimensional Ni-Fe layered double hydroxide/graphene electrode for water oxidation. J. Mater. Chem. A 2015, 13, 6921-6928.

204. Tang, D.; Liu, J.; Wu, X.; Liu, R.; Han, X.; Han, Y.; Huang, H.; Liu, Y.; Kang, Z. Carbon Quantum Dot/NiFe Layered Double-Hydroxide Composite as a Highly Efficient Electrocatalyst for Water Oxidation. ACS Appl. Mater. Interfaces 2014, 6, 7918-7925.

205. Song F.; Hu, X. Exfoliation of layered double hydroxides for enhanced oxygen evolution catalysis. Nat. Commun. 2014, 5, 4477.

206. Lu, Z.; Qian, L.; Tian, Y.; Li, Y.; Sun, X.; Duan, X. Ternary NiFeMn Layered Double Hydroxides as High efficient Oxygen Evolution Catalysts. Chem. Commun. 2016, 52, 908-911.

207. Long, X.; Xiao, S.; Wang, Z.; Zheng X.; Yang, S. Co Intake Mediated Formation of Ultrathin Nanosheets of Transition Metal LDH-an Advanced Electrocatalyst for Oxygen Evolution Reaction. Chem. Commun. 2015, 51, 1120-1123.

208. Qin, C.; Wang, J.; Yang, D.; Li, B.; Zhang C. Proton Exchange Membrane Fuel Cell Reversal: A Review. Catalysts 2016, 6, 197.

209. Tan, Y.; Xu, C.; Chen, G.; Zheng, N.; Xie, Q. A Graphene-Platinum Nanoparticles-Ionic Liquid Composite Catalyst for Methanol-Tolerant Oxygen Reduction Reaction. Energy Environ. Sci. 2012, 5 (5), 6923.

210. Dai, L.; Xue, Y.; Qu, L.; Choi, H.-J.; Baek, J.-B. Metal-Free Catalysts for Oxygen Reduction Reaction. Chem. Rev. 2015, 115 (11), 4823-4892.

211. Weng, X.; Liu, Q.; Feng, J.-J.; Yuan, J.; Wang, A.-J. Dendrite-like PtAg Alloyed Nanocrystals: Highly Active and Durable Advanced Electrocatalysts for Oxygen Reduction and Ethylene Glycol Oxidation Reactions. J. Colloid Interface Sci. 2017, 504, 680-687.

212. Mahata, A.; Nair, A. S.; Pathak, B.; Recent advancements in Pt-nanostructure-based electrocatalysts for the oxygen reduction reaction. Catal. Sci. Technol. 2019, 9, 4835-4863.

213. Shinozaki, K.; Morimoto, Y.; Pivovar, B. S.; Kocha, S. S. Suppression of Oxygen Reduction Reaction Activity on Pt-Based Electrocatalysts from Ionomer Incorporation. J. Power Sources 2016, 325, 745-751.

214. Paulus, U. A.; Wokaun, A.; Scherer, G. G.; Schmidt, T. J.; Stamenkovic, V.; Markovic, N. M.; Ross, P. N. Oxygen Reduction on High Surface Area Pt-Based Alloy Catalysts in

Comparison to Well Defined Smooth Bulk Alloy Electrodes. Electrochim. Acta 2002, 47, 3787-3798.

215. Todoroki, N.; Dasai, T.; Asakimori, Y.; Wadayama, T. Microscopic Surface Structures and ORR Activities for Vacuum-Deposited Pt/Ni/Pt(111) and Pt/Ni/Pt(110) Sandwich Structures. J. Electroanal. Chem. 2014, 724, 15-20.

216. Zhang, Y.; Ma, C.; Zhu, Y.; Si, R.; Cai, Y.; Wang, J. X.; Adzic, R. R. Hollow Core Supported Pt Monolayer Catalysts for Oxygen Reduction. Catal. Today 2013, 202, 50-54.

217. Wang, L.; Yamauchi, Y. Metallic Nanocages: Synthesis of Bimetallic Pt-Pd Hollow Nanoparticles with Dendritic Shells by Selective Chemical Etching. J. Am. Chem. Soc. 2013, 135, 45, 16762-16765.

218. Sui, S.; Wang, X.; Zhou, X.; Su, Y.; Riffatc, S.; Liu, C. A comprehensive review of Pt electrocatalysts for the oxygen reduction reaction: Nanostructure, activity, mechanism and carbon support in PEM fuel cells. J. Mater. Chem. A 2017, 5, 1808-1825.

219. Tian, X.; Luo, J.; Nan, H.; Zou, H.; Chen, R.; Shu, T.; Li, X.; Li, Y.; Song, H.; Liao, S.; Adzic, R. R. Transition Metal Nitride Coated with Atomic Layers of Pt as a Low Cost, Highly Stable Electrocatalyst for the Oxygen Reduction Reaction. J. Am. Chem. Soc. 2016, 138, 1575-1583.

220. Hye, R. B.; Jin, S.; Yang, S. H. Graphene-Based Non-Noble-Metal Catalysts for Oxygen Reduction Reaction in Acid. Chem. Mater. 2011, 23, 15, 3421-3428.

221. Liu, F.; Yang, X.; Dang, D.; Tian, X. Engineering of hierarchical and three dimensional architectures constructed by titanium nitride nanowire assemblies for efficient electrocatalysis. ChemElectroChem 2019, 6, 2208–2214.

222. Tian, X.; Luo, J.; Nan, H.; Fu, Z.; Zeng, J.; Liao, S. Binary transition metal nitrides with enhanced activity and durability for the oxygen reduction reaction. J. Mater. Chem. A 2015, 3, 16801-16809.

223. Tian, X.; Lu, X. F.; Xia, B. Y.;Lou, X. W. Advanced Electrocatalysts for the Oxygen Reduction Reaction in Energy Conversion Technologies. Joule 2020, 4, 45-68.

224. Tao, H.; Liu, S.; Luo, J.-L.; Choi, P.; Liu, Q.; Xu, Z. Descriptor of catalytic activity of metal sulfides for oxygen reduction reaction: a potential indicator for mineral flotation. J. Mater. Chem. A 2018, 6(20), 9650-9656.

225. Parra-Puerto, A.; NG, K. L.; Fahy, K.; Goode, A. E.; Ryan, M. P.; Kucernak, A. Supported Transition Metal Phosphides: Activity Survey for HER, ORR, OER and Corrosion Resistance in Acid and Alkaline Electrolytes. ACS Catal. 2019, 2019, 9, 12, 11515-11529.

226. Yang, L.; Zeng, X.; Wang, W.; Cao, D. Recent progress in MOF-derived, heteroatom-doped porous carbons as highly efficient electrocatalysts for oxygen reduction reaction in fuel cells. Adv. Funct. Mater. 2018, 28, 1704537.

227. Singh, S. K.; Takeyasu, K.;Nakamura, J. Active sites and mechanism of oxygen reduction reaction electrocatalysis on nitrogen-doped carbon materials. Adv. Mater. 2019, 31, 1804297.

228. Wu, K. H.; Wang, D. W.; Su, D. S.; Gentle, I. R. A discussion on the activity origin in metal-free nitrogen-doped carbons for oxygen reduction reaction and their mechanisms. ChemSusChem 2015, 8, 2772-2788.

229. Zhou, M.; Wang, H.-L.; Guo, S. Towards High-Efficiency Nanoelectrocatalysts for Oxygen Reduction through Engineering Advanced Carbon Nanomaterials. Chem. Soc. Rev. 2016, 45 (5), 1273-1307.

230. Kobayashi1, R.; Ishii, T.; Imashiro, Y.; Ozaki, J. Synthesis of P- and N-doped carbon catalysts for the oxygen reduction reaction via controlled phosphoric acid treatment of folic acid. J. Nanotechnol. 2019, 10, 1497-1510.

231. Bhange, S. N.; Unni, S. M.; Kurungot, S. Nitrogen and sulphur co-doped crumbled graphene for the oxygen reduction reaction with improved activity and stability in acidic medium. J. Mater. Chem. A 2016, 4, 6014-6020.

232. Li, Y.; Zhou, W.; Wang, H.; Xie, L.; Liang, Y.; Wei, F.; Idrobo, J.-C.; Pennycook, S. J.; Dai, H. An Oxygen Reduction Electrocatalyst Based on Carbon Nanotube Nanographene Complexes. Nature Nanotechnology 2012, 7(6), 394-400.

233. Zhang, L.; Xia, Z. Mechanisms of Oxygen Reduction Reaction on Nitrogen-Doped Graphene for Fuel Cells. J. Phys. Chem. C 2011, 115, 11170.

CHAPTER 2

The Ultimate Limit of Pt Electrocatalytic Activity in PtRu/Nitrogen- and Sulphur-co-doped Crumbled Graphene in Acid and Alkaline Media

2.1 Introduction

Pt supported on carbon (Pt/C) is a widely used electrocatalyst for hydrogen evolution reaction (HER), owing to its low overpotential and enhanced stability in harsh environment [1-3]. Despite these favorable properties, the extremely high price and low natural abundance have severely constrained Pt large-scale industrial application [4-6]. In order to make fuel cells commercially viable, several strategies have been attempted through the reduction of Pt amount or using non-noble metal electrocatalysts without sacrificing their performance. The best performing non-noble metal electrocatalysts reported often contain a transition metal cation such Fe [7-8], Co [9- 10] or Ni [11-12]. Unfortunately, their Tafel slopes (thus kinetics) and overpotential values are still higher than those of common Pt-based catalysts for HER and methanol oxidation reaction (MOR). To achieve low Tafel slopes and small overpotentials, high loadings of these non-precious catalysts are required [13], preventing their widespread usage in fuel cells.

Reduction of Pt amount while preserving the electrocatalytic efficiency is another viable alternative. Over the past decade, countless attempts have been devoted to research for the reduction of the amount of Pt, which in turn allows reducing the cost [14]. From the literature survey, Pt alloy catalysts are well adapted to reach this goal, owing to their dramatic enhancement of the electrocatalytic properties and stability, as compared to single element Pt catalyst. Li et al. demonstrated that Pt-Zn nanowires are suitable for methanol and formic acid electrooxidation [15]. Birss et al. synthesized $Ir_{core}@Pt_{shell}$ nanostructures with controlled Pt shell coverages for enhanced MOR and found that the Ir_{core} enhances the activity of the Pt_{shell}

primarily through the bifunctional effect [16]. Liu et al. prepared controlled Pt monolayer catalyst on complex 3D structures for superior HER [17-19]. In general, in most of these methods, a similar strategy was adopted, consisting of Pt loading onto large specific surface area materials and highly dispersible nanomaterials with the aim to reduce the Pt amount [20-24]. However, these approaches need strict technical requirements and are often associated with expensive production costs. Additionally, the low stability of these catalysts also restricts their performance for fuel cell applications, because this could eventually lead to a substantial catalytic activity loss, meaning that these catalysts need to be replaced soon upon their utilization. In order to increase the efficiency, the electrocatalyst should exhibit good stability, high activity, and low cost.

In this study, we describe the synthesis of high-performance Pt-Ruthenium (Ru) nanoparticles loaded on PF (sulphur- and nitrogen-co-doped crumbled graphene derived from polyethylenedioxythiophene with trace amount of Fe) [25]. These catalysts have several merits as the amount of Pt used was reduced to a minimum, and Ru being relatively cheap (~ 4% the price of Pt) and displaying a comparable bond strength as Pt for hydrogen. PF was investigated as the support owing to its corrosion resistance and high surface area (**Figure 1**). Interestingly, the $PtRu_2$/PF catalyst, with a small amount of Pt, displayed improved performance than the catalyst with higher Pt loading (Pt_2Ru/PF) for catalyzing HER and MOR under acidic conditions. Additionally, the catalyst also had an excellent performance for oxygen reduction reaction (ORR) and oxygen evolution reaction (OER) in alkaline media compared to many reported noble-metal catalysts.

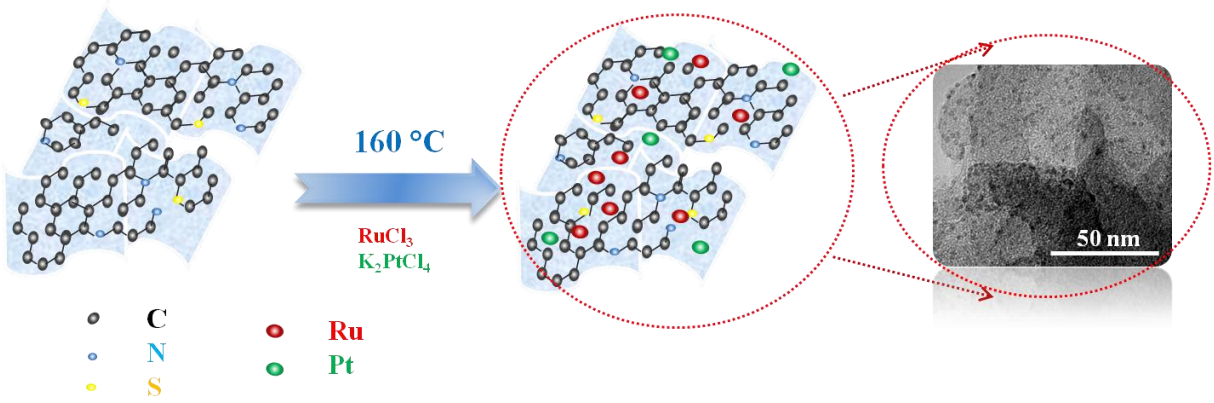

Figure 1. Fabrication process of Pt and Ru nanoparticles supported on PF electrocatalysts.

2.2 Experimental section

2.2.1 Synthesis of sulphur- and nitrogen-co-doped crumbled graphene (PF)

Briefly, 2 mL of ethylenedioxythiophene (EDOT) monomer were dissolved in 80 mL of 1 M hydrochloric acid (HCl) solution using 1 g of cetyltrimethylammonium bromide (CTAB) surfactant at room temperature. A solution of 5 g of ammonium persulfate [$(NH_4)_2S_2O_8$] in 20 mL of 1 M HCl was added dropwise to the EDOT solution, followed by the addition of 9.1 g of iron chloride hexahydrate ($FeCl_3 \cdot 6H_2O$) solution in 20 mL of 1 M HCl solution. The resulting mixture was kept under constant stirring for a period of 24 h. The suspension containing the polymer and transition metal salt was dried at 80 °C with stirring. This product is termed as PEDOT-Fe. The PEDOT-Fe was annealed for 1 h at 900 °C in an argon atmosphere for the carbonization. The resulting black powder was dispersed in 0.5 M H_2SO_4 and stirred at 80 °C for 8 h. The acid-washed sample was further annealed at 900 °C for 1 h in argon atmosphere to yield the final product. The product, named as PF, represents the annealed PEDOT-Fe.

2.2.2 Synthesis and characterization of Pt_mRu_n/PF electrocatalysts

A mixture of n mg of ruthenium (III) chloride (RuCl3) (n=30, 20, 15, 0), m mg of potassium tetrachloroplatinate (II) (K_2PtCl_4) (m=0, 10, 15, 30), 60 mg of PF, 36 mL of DMF,

and 9 mL of methanol was heated for 15 h at 160 °C. The products (using the original mass ratio of K_2PtCl_4 and $RuCl_3$ named as Pt_mRu_n/PF) were collected and dried at 60 °C for overnight.

2.2.3 Electrochemical measurements

The electrocatalytic activity was assessed in a three-electrode system using an electrochemical workstation (Solartron, France). The Ag/AgCl electrode was used as the reference, graphene rod as the counter electrode, and a modified glassy electrode (GC) as the working electrode. The working electrode was prepared as follows: (1) 1 mg of Pt_mRu_n/PF sample and 80 μL of a Nafion solution (5 wt.%) were dispersed in 1 mL MQ water using sonication for 1 h to form a homogeneous ink, (2) 10 μL portion of the resulting solution was drop casted onto a GC electrode (3 mm in diameter) by a microliter syringe and dried at room temperature. The potential was calibrated to a reversible hydrogen electrode (RHE). The measured potentials were converted to that relative to the reversible hydrogen electrode (RHE) according to $E_{RHE} = E_{Ag/AgCl} + 0.059 * pH + E°_{Ag/AgCl}$, with $E°_{Ag/AgCl} = 0.2046$ V (25°C).

2.3 Results and discussion

2.3.1 Surface analysis of $PtRu_2$/PF

Scanning electron microscopy (SEM) was applied to analyze the microstructure of PF and $PtRu_2$/PF samples. **Figure 2A** displays the SEM image of PF, exhibiting a highly porous nature of the material. It consists of nanoflakes of graphene sheets assembled in an interconnected fashion, leading to the establishment of open pores in the matrix. After deposition of Pt and Ru, no obvious change of the surface morphology of PF can be seen. This is most likely ascribed to the small size of Pt and Ru particles (**Fig. 2B**). At the same time, small amounts of Pt and Ru are loaded onto the surface of PF substrate or intercalated between PF layers.

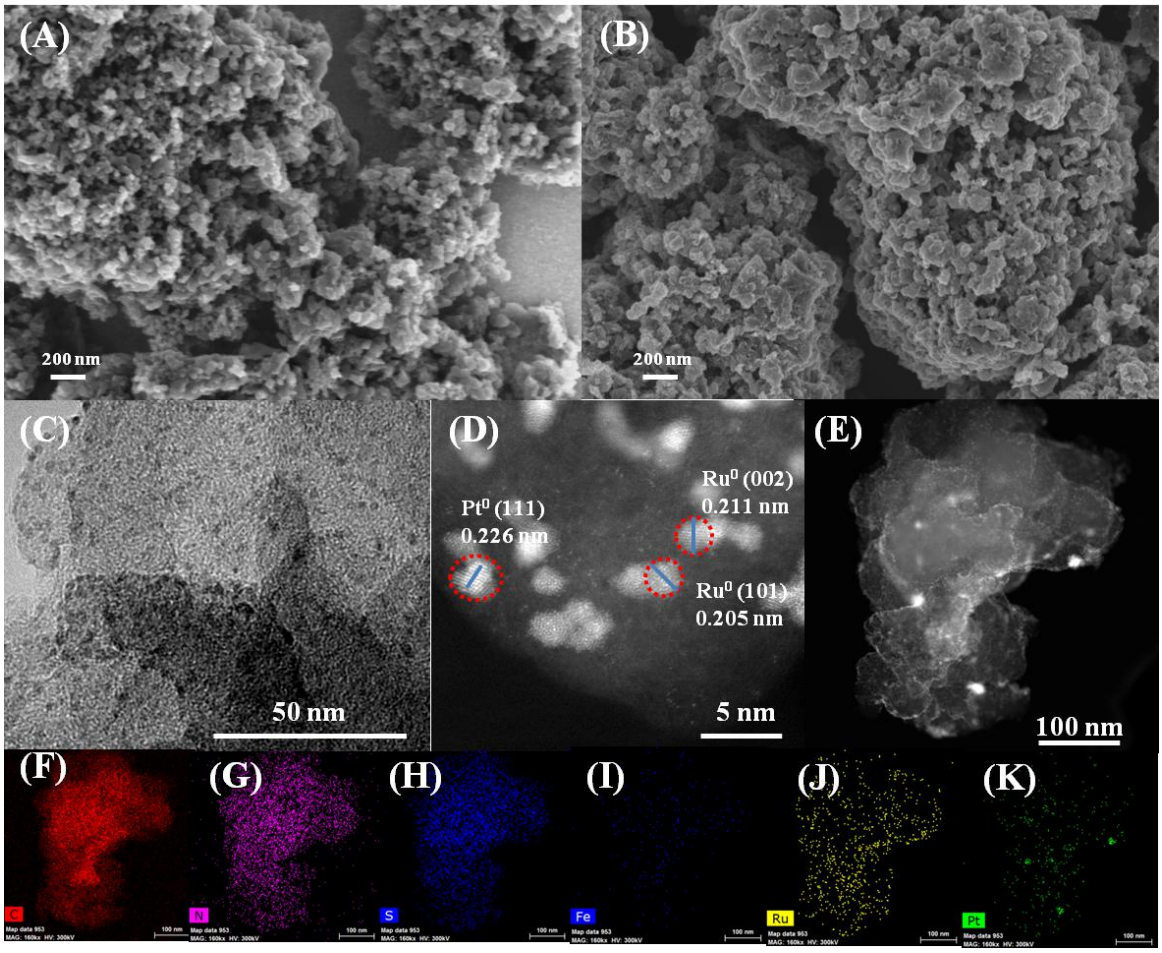

Figure 2. Typical SEM images of (A) PF and (B) $PtRu_2$/PF. (C) TEM image and (D) HRTEM of $PtRu_2$/PF. (E) HAADF-STEM image of $PtRu_2$/PF. (F-K) the corresponding EDX maps of (F) C, (G) N, (H) S, (I) Fe, (J) Ru and (K) Pt obtained from the region in (E).

Additionally, the edges of graphene sheets from the PF were further observed from the transmission electron microscopy (TEM) images.**Figure 2C** depicts the high-resolution TEM image of $PtRu_2$/PF. It shows a uniform structure consisting of thin graphene sheets, and not many large particles are found. Small nanoparticles (2-3 nm) of Ru and Pt can be easily identified with lattice spacings of 0.205, 0.211 and 0.226 nm, which are consistent with the (101) and (002) facets of the Ru^0 crystal (PDF 06-0663) and the (111) facet of the Pt^0 crystal (PDF 87-0646), respectively (**Fig. 2D**). **Figure 2E** shows a transparent graphene sheet structure, implying that no large particles were formed under these experimental conditions.

Furthermore, energy-dispersive X-ray spectroscopy (EDX)mapping was performed to study the distribution of the C, N, S, Fe, Ru and Pt elements in $PtRu_2$/PF sample. All the mapping images (**Fig. 2F-K**) present the same profile as that shown in the rectangular area (**Fig. 2E**), indicating that these elements are homogeneously distributed on the PF surface. In addition, the spots originating from Pt particles are fairly less as compared to Ru particles, and are spread randomly throughout the PF, suggesting that the Pt content is lower than that of Ru, and Ru and Pt are finely dispersed (**Fig. 2J** and **2K**).

2.3.2 Structural analysis of $PtRu_2$/PF

Figure 3A depicts the X-ray diffraction (XRD) patterns of PF and $PtRu_2$/PF electrocatalyst. The XRD pattern of PF depicts a broad peak at 25.3° ascribed to the (002) plane of graphitic carbon, and a relatively weak diffraction peak at 44.1° assigned to the (101) plane, in good agreement with earlier report [26].The XRD pattern of $PtRu_2$/PF reveals the presence of an intense and large peak located at ~25.3° assigned to C (002), and another broad peak between 38° ~ 46° corresponding to an overlap of Ru (100) (38.4°), Ru (002) (42.2°), Ru (101) (44.0°), Pt (111) (40.1°) and Pt (200) (45.38°) in $PtRu_2$/PF (PDF 87-0646 for Pt and PDF 06-0663 for Ru).This is due to the broadening of the main Ru peak, indicating that Ru nanoparticles contain still much more crystallites than Pt.

The Raman spectra of both PF and $PtRu_2$/PF display two bands at ~1340 and 1580 cm^{-1} (**Fig. 3B**) assigned respectively to the disorder-induced D band and the tangential mode G band from PF.It was found that $PtRu_2$/PF had a lower I_D/I_G (0.81) than PF (1.03), signifying that $PtRu_2$/PF has structural low defects.

X-ray photoelectron spectroscopy (XPS) analysis revealed the expected C, N, S, Ru and Pt in $PtRu_2$/PF composite (**Fig. 3C**). In **Figure 3D**, the high-resolution XPS spectrum of the Pt_{4f} of the catalyst showed doublet peaks at 71.8 and 75.2 eV, which can be deconvoluted into two bands. The deconvoluted doublet bands at 71.2 and 74.6 eV, and 72.1 and 76.0 eV can be

ascribed to the Pt^0 and Pt^{2+}, respectively [27]. In the C_{1s} and Ru_{3d} XPS core level spectrum (**Fig. 3E**), the bands at 279.9 and 283.6 eV can be attributed to $Ru_{3d5/2}$ and $Ru_{3d3/2}$ of Ru(0), respectively [28].The C_{1s} peak can be deconvoluted into three peaks centered at 284.5, 286.1 and 287.6 eV, corresponding to the C=C/C-C, C-O and C=O bonds, respectively.The core level XPS spectrum of the Ru_{3p} can be curve-fitted with two bands at 461.4 and 483.8 eV, respectively (**Fig. 3F**), confirming the metallic character of Ru(0) in $PtRu_2$/PF nanocomposite [29].

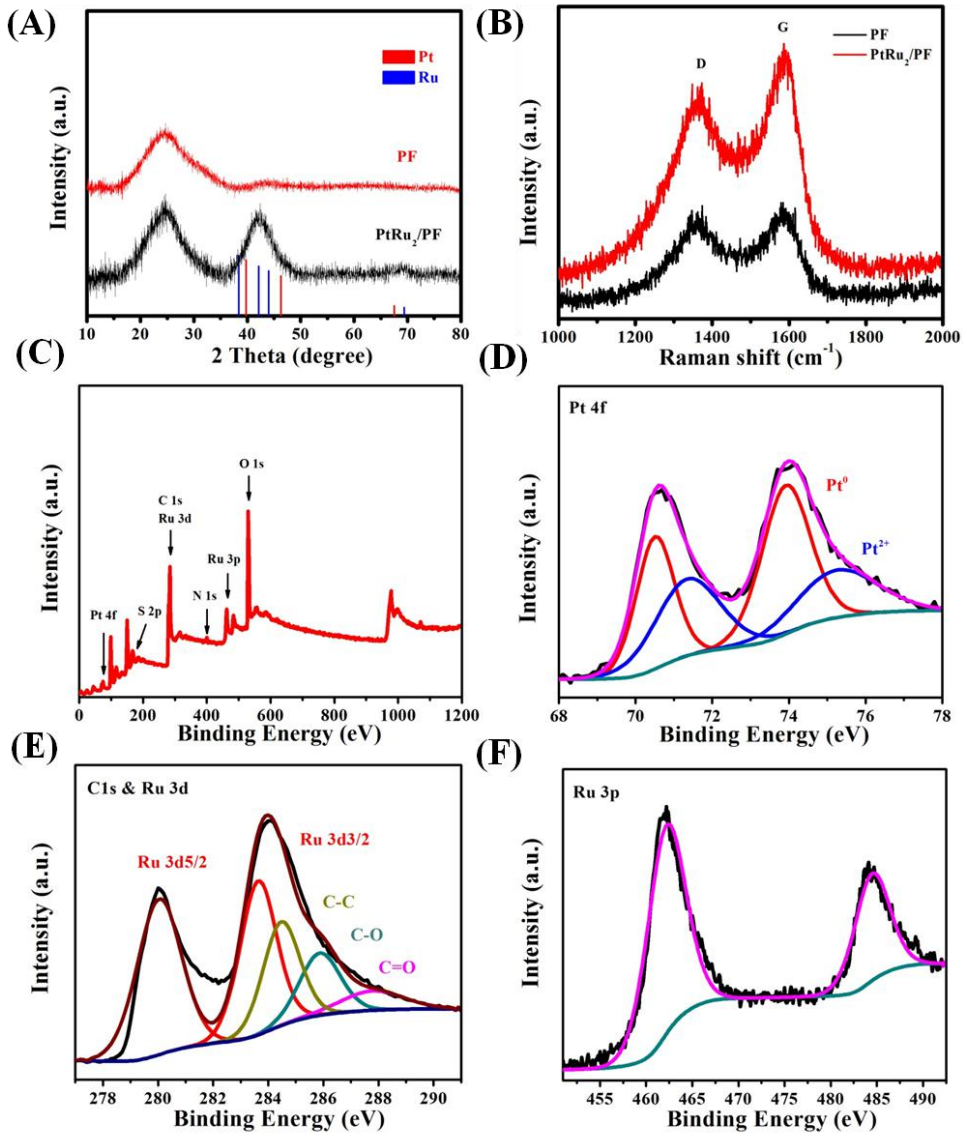

Figure 3. (A) XRD patterns, (B) Raman spectra of PF and $PtRu_2$/PF, (C) XPS full scan and core level spectra of (D) Pt 4f, (E) C 1s and Ru 3d, and (F) Ru 3p of $PtRu_2$/PF.

To further determine the Pt and Ru content in the $PtRu_2$/PF sample, we performed inductive coupled plasma emission spectrometry (ICP-AES) measurements. The results confirmed the prevalence of Ru (72.4 mg/g) over Pt (28.3 mg/g) content in the $PtRu_2$/PF sample. The Ru/Pt mass ratio is ~2.6, which is slightly higher than the theoretical value of 2. In addition, the average precious metal mass per square centimeter of the working electrode is 4.0 μg/cm^2 for Pt and 10.4 μg/cm^2 for Ru.

2.3.3 Electrocatalytic activity for HER

The electrocatalytic HER activity of the synthesized Pt-based catalysts (PF, Ru/PF, $PtRu_2$/PF, PtRu/PF, Pt/PF and 20% Pt/C) was tested in H_2SO_4 (0.5 M) aqueous solution using linear sweep voltammetry (LSV) measurements (**Figure 4A**). For comparison to the literature, the measured potentials were converted to that relative to the reversible hydrogen electrode (RHE) according to equation:

$$E_{RHE} = E_{Ag/AgCl} + E°Ag/AgCl + 0.059 \times pH \quad (1)$$

pH=0 and $E^{\circ}_{Ag/AgCl}$= 0.2046 (25°C)

From the first sight, it seems that the investigated catalysts are very effective for hydrogen evolution. This is clear from their low HER onset potential (E_{HER}, the potential at which the current starts to rise and a reaction starts taking place) values in **Table 1** and steep cathode polarization curves beyond E_{HER}. The results identified that the $PtRu_2$/PF, PtRu/PF, Pt/PF and 20% Pt/C catalysts exhibited low E_{HER} values, all around -0.02 V_{RHE}, and high cathode currents beyond E_{HER}. These findings revealed the ability of these catalysts to generate significant amount of hydrogen gas at low overpotentials, thus reflecting their high catalytic HER activity. On the contrary, Ru/PF and PF exhibited inferior catalytic activity for the HER, as they recorded significantly higher E_{HER}, namely -0.06 and -0.16 V_{RHE}, respectively. Moreover, by comparing the current density changes at any applied overpotential, the $PtRu_2$/PF exhibited clear advantages over the potential range from 0.05 to -0.30 V_{RHE}. For

instance, the $PtRu_2$/PF catalyst achieved a current density of -76 $mA \cdot cm^{-2}$ at E = -0.2 V_{RHE}, higher than that derived from the PtRu/PF catalyst (-57 $mA \cdot cm^{-2}$) at the same overpotential. The current densities from other catalysts, namely PF, Ru/PF, Pt/PF and 20% Pt/C are markedly much smaller: -0.5, -13, -33 and -35 $mA \cdot cm^{-2}$, respectively. At any given current density, the overpotential was shifted toward less negative values (active direction), following the sequence: Ru/PF > Pt/PF > 20% Pt/C ≥ PtRu/PF ≥ $PtRu_2$/PF. The overpotential necessary to achieve a current density of -10 $mA \cdot cm^{-2}$ (η_{10}), an important electrochemical parameter to evaluate and compare the HER performance of electrocatalysts [30], was determined for all investigated materials. For instance, $PtRu_2$/PF recorded the least η_{10} value (101 mV) among other studied catalysts i.e. PtRu/PF, Pt/PF, Ru/PF and 20% Pt/C. This anodic shift in E_{HER} refers generally to accelerated HER kinetics at low overpotential [31]. Therefore, the results confirmed the superior HER activity of the $PtRu_2$/PF catalyst.

The active drift in E_{HER} is also translated into increased exchange current density (J_o), i.e., enhanced HER kinetics [32]. This is clear from **Table 1**; the promising catalytic activity of $PtRu_2$/PF catalyst is also confirmed, as it recorded the highest J_o value among the tested catalysts.

Table 1. Comparison of Pt HER electrocatalysts in 0.5 M H_2SO_4 solution.

Catalysts	**Onset potential (mV)**	**Overpotential (mV) (J=-10 mA/cm^2)**	**Tafel slope (mV dec^{-1})**	**Exchange current density -log$_{10}$j$_0$/(A cm^{-2})**
PF	-160	-486	340	3.22
Ru/PF	-60	-87	64	2.90
$PtRu_2$/PF	-10	-22	30	2.81
PtRu/PF	-10	-22	30	2.81
Pt/PF	-15	-31	32	2.82

Commercial Pt/C	-12	-30	31	2.81

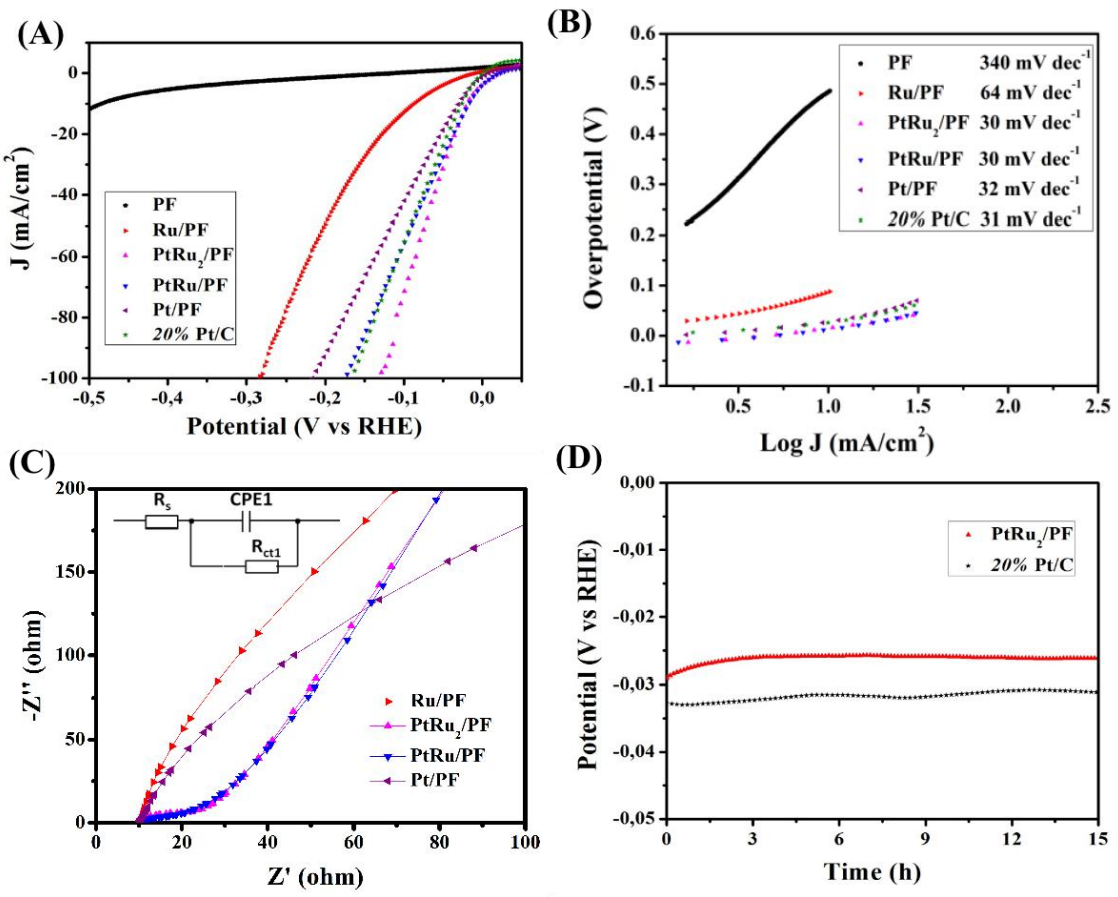

Figure 4. Electrochemical characterization. (A) HER polarization curves, scan rate = 20 mV s^{-1}, (B) Tafel plots, and (C) EIS Nyquist plots of Ru/PF, $PtRu_2$/PF, PtRu/PF, Pt/PF, and 20% Pt/C in 0.5 M H_2SO_4 aqueous solution; the inset is the equivalent circuit, (D) HER stability test of $PtRu_2$/PF at J= -10 mA/cm^2 in H_2SO_4 (0.5 M) aqueous solution.

The Tafel slope (β_c), calculated by fitting the linear segments of the Tafel plots, gives a good measure of the intrinsic properties of electrocatalytic materials [33]. As shown in **Figure 4B**, Pt/PF and Ru/PF catalysts recorded β_c values of 32 and 64 mV dec^{-1}, respectively, which are very close to those reported for Pt/C (30 mV dec^{-1}) and Ru/MeOH/THF (46 mV dec^{-1}), respectively [34]. In contrast, a high β_c value of 340 mV dec^{-1} was measured for PF, revealing

its inferior catalytic activity. For $PtRu_2$/PF and PtRu/PF catalysts, the measured β_c values are around 30 mV dec^{-1}, signifying much improved HER activity, as lower β_c values reveal increased number of catalytically active sites [35].

The overall HER reaction mechanism in acidic media could occur through a discharge step (Volmer-reaction, 120 mV dec^{-1}), followed by ion or atom reaction (Heyrovsky reaction, 40 mV dec^{-1}) or a combination reaction (Tafel reaction, 30 mV dec^{-1}) [36]. It was proposed that, at a very high surface coverage of adsorbed hydrogen (H_{ads}), the HER on the Pt surface is controlled by the Volmer-Tafel mechanism, with the recombination step being the slowest (rate-determining) step, as evidenced from the recorded Tafel slope (30 mV dec^{-1}) [37]. Based on this, the small Tafel slope (~ 30 mV dec^{-1}) recorded for $PtRu_2$/PF and PtRu/PF catalysts suggests a HER mechanism similar to that occurred on Pt.

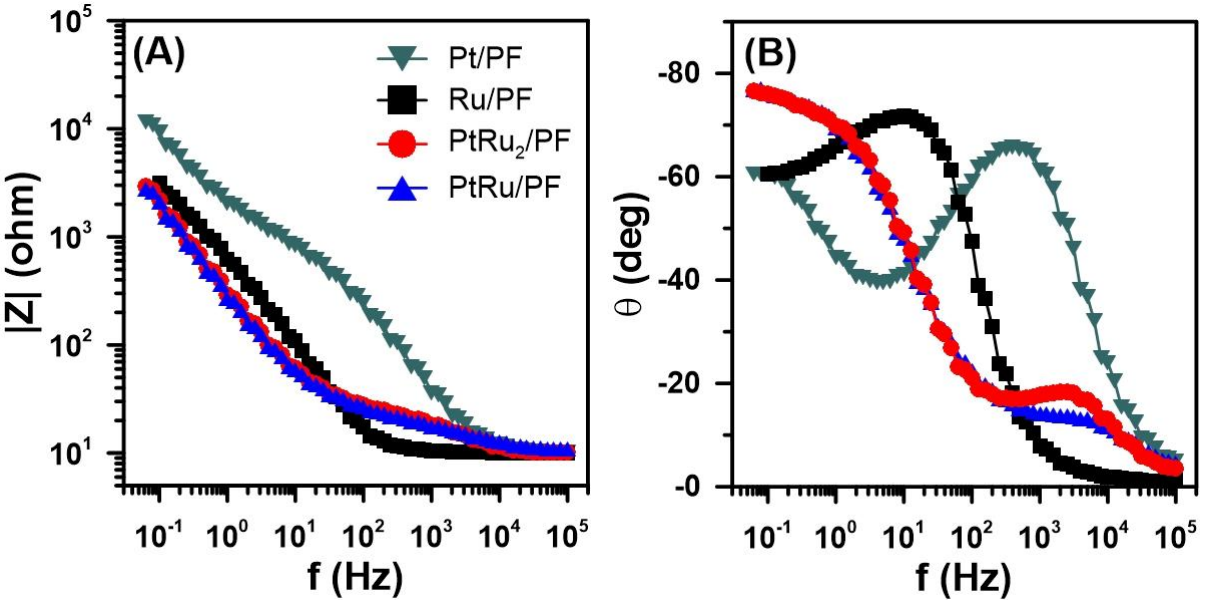

Figure 5. Bode (A) impedance modulus |Z| and (B) phase angle θ plots of Pt/PF, Ru/PF, PtRu/PF and $PtRu_2$/PF electrodes. Measurements were carried out at a stationary potential with a perturbation amplitude of 0.1 V in the 100 kHz - 0.1 Hz frequency range.

The Electrochemical Impedance Spectroscopy (EIS) studies corroborate previously presented results (**Figure 5)**. The Bode plots (**Figure 5A, B**) revealed the presence of two

relaxation times. The total impedance |Z| remains the smallest for analyzed Ru-enriched materials, with negligible differences between PtRu/PF and $PtRu_2$/PF samples. On the other hand, its value is nearly an order of magnitude higher for Pt/PF sample at a wide frequency range. Both PtRu/PF and $PtRu_2$/PF electrodes demonstrate the decrease of the phase angle and its shift into higher frequency range as compared to Pt/PF electrode, testifying the enhanced electron transfer kinetics. In addition, the charge transfer kinetics appears to be the most sluggish through the Ru/Pt electrode. Similar characteristics are often seen when studying the catalysts at increased overpotentials [38,39].

The Nyquist plots in **Figure 4C** confirm the above conclusions. The high frequency semicircle present on the analyzed spectra reflects the charge transfer process of hydrogen evolution reaction [39,40]. The inclined line, at low frequencies, indicates the electron diffusion behavior on the electrode interface, representative of a diffusion-controlled process [41-43]. The value of the charge transfer resistance R_{ct} was determined to be ~15 and 20 Ω/cm^2 for PtRu/PF and $PtRu_2$/PF electrodes, respectively [44]. For comparison, the R_{ct} of Ru-free Pt/PF electrode is roughly 800 Ω/cm^2. The significant decrease of the charge transfer resistance as a result of Ru incorporation testifies the faster reaction rates and the enhanced electrocatalytic properties of the material. The enhanced activity towards HER resulting from Ru incorporation was also reported in previous studies [45]. The reduced R_{ct} of $PtRu_2$/PF and PtRu/PF may be explained by the interaction and synergy of the two metals. The better electron transfer ability of $PtRu_2$/PF and PtRu/PF are also expected to contribute to their enhanced HER catalytic activity [46].

The stability is an important feature for the HER catalysts. Therefore, the stability of $PtRu_2$/PF and *20%* Pt/C catalysts was assessed at a controlled current density ($J = -10\ mA \cdot cm^{-2}$) for 15 h in H_2SO_4 (0.5 M) aqueous solution (**Fig. 4D**); the overpotential of the $PtRu_2$/PF

catalyst was more stable than that of *20%* Pt/C under our experimental conditions, suggesting its good stability [17, 21].

The electrochemical active surface area (ECSA) of these catalysts was estimated from cyclic voltammetry (CV) measurements, conducted in H_2SO_4 (0.5 M) aqueous solution at various potential scan rates (ca. 30 - 80 mV s^{-1}) from 0.15 to 0.45 V *vs.* RHE (**Figure 6 A-E**). The CVs display a pseudo-rectangular shape without any apparent Faradic processes.

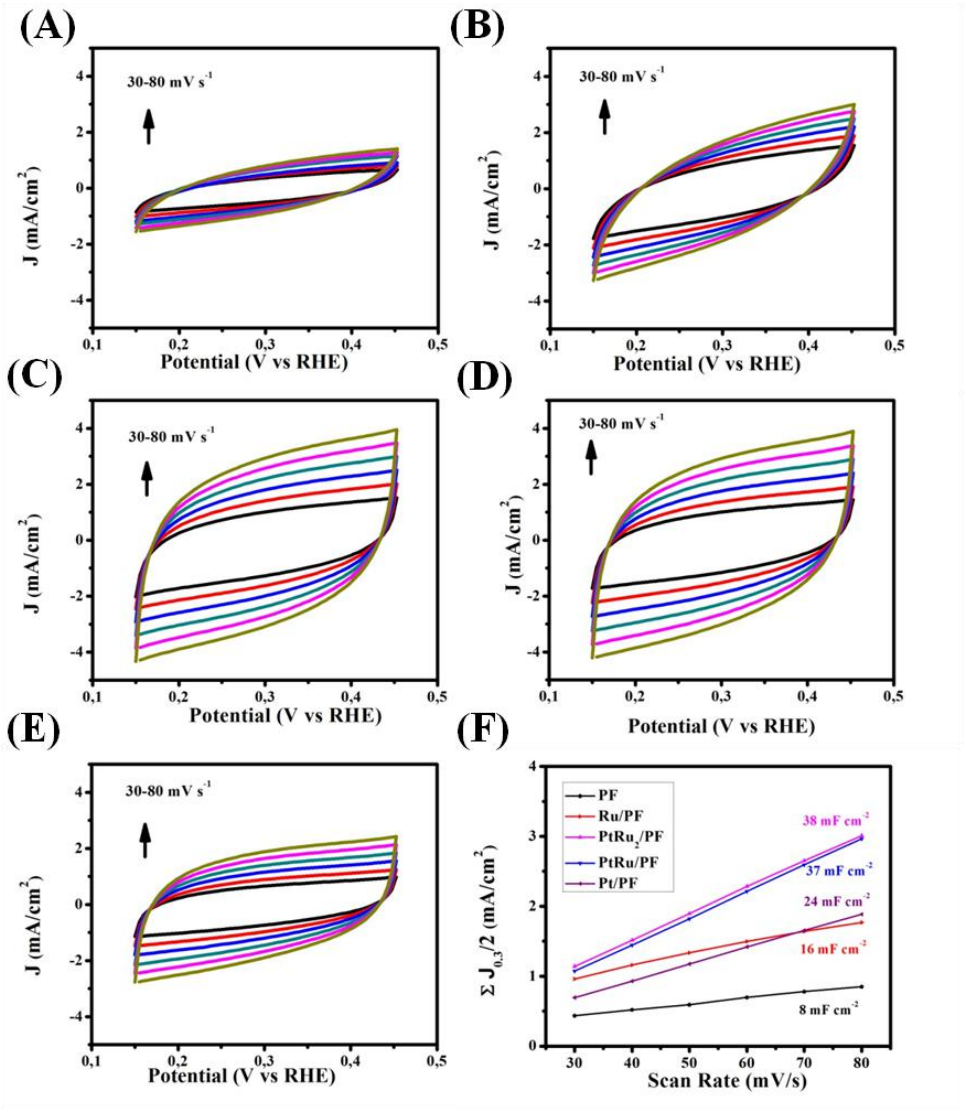

Figure 6. Cyclic voltammograms of (A) PF, (B) Ru/PF, (C) $PtRu_2$/PF, (D) PtRu/PF and (E) Pt/PF in the 0.15 ~ 0.45 V potential range *vs.* RHE. (F) Double-layer charging currents of PF, Ru/PF, $PtRu_2$/PF, PtRu/PF, Pt/PF recorded at 0.10 V at various scan rates (30 ~ 80 mV s^{-1}) in 0.5 M H_2SO_4.

The current density values, determined at 0.10 V (vs SCE) from the CV, were then plotted as a function of the scan rate. From the results in **Figure 6F**, the C_{dl} of $PtRu_2$/PF and PtRu/PF were determined to be as 38 and 37 mF cm^{-2}, larger than the other catalysts: Pt/PF (24 mF cm^{-2}), Ru/PF (16 mF cm^{-2}) and PF (8 mF cm^{-2}). A higher C_{dl} value correlates with more exposed active sites, which is favorable for electrochemical processes. From the above results, we can conclude that $PtRu_2$/PF exhibits more active sites than PtRu/PF [47].

The values of C_{dl} were inserted in Eq. (2) to calculate the ECSA values [48]:

$$ECSA = C_{dl} / C_s \quad (2)$$

C_s is the electrode's specific capacitance with a flat standard surface area of 1.0 cm^{-2}, typically between 20 and 60 μF cm^{-2} [48]. Using 40 μF cm^{-2} as the average capacitance value for the flat electrode, ECSA values of 200, 400, 600, 925, and 950 cm^{-2} were determined for PF, Ru/PF, Pt/PF, PtRu/PF, and $PtRu_2$/PF, respectively.

2.3.4 Active sites density calculations

Figure 7 depicts typical cyclic voltammetry measurements for PF, Ru/PF, Pt/PF, PtRu/PF, and $PtRu_2$/PF catalysts conducted in 0.5 M H_2SO_4 aqueous solution at a scan rate of 100 mV s^{-1} at room temperature. The number of active sites (n) in PtRu/PF and $PtRu_2$/PF catalysts was calculated from such measurements, using Eq. (3) [49]:

$$n = (Q/2F) \times N_A \quad (3)$$

N_A = 6.022 × 10^{23} mol^{-1} is the Avogadro's number, the number 2 is the stoichiometric number of electrons consumed during the HER reaction, and F is the Faraday constant (96485 C/mol). Q is the net voltammetry charge of the catalyst, estimated by subtracting charges resulting from the bare PF electrode (the black cyclic voltammogram in **Figure 5**). Q values of 4.05 × 10^{-2} and 5.8 × 10^{-2} C were recorded for PtRu/PF and $PtRu_2$/PF catalysts, respectively. Inserting such Q values into Eq. (3) gives n values of 1.26 × 10^{17} and 1.81 × 10^{17} Ru sites per cm^2, respectively.

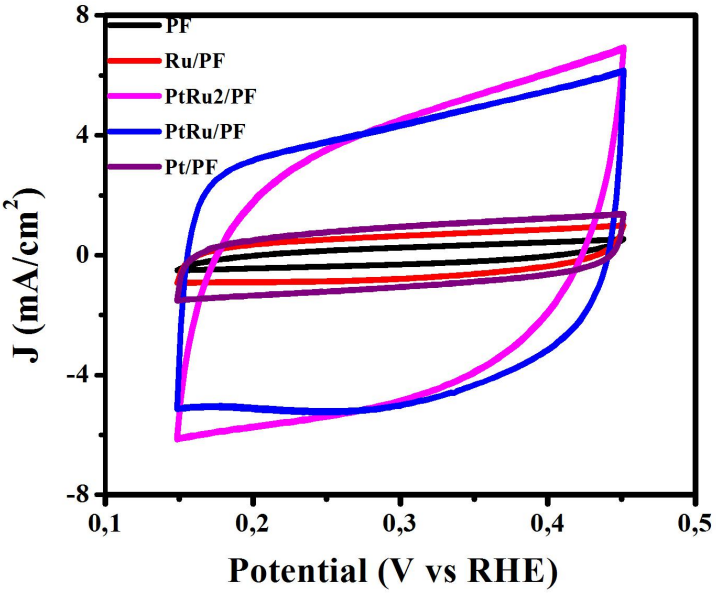

Figure 7. Cyclic voltammograms of the synthesized catalysts acquired in the 0.15 ~ 0.45 V potential range *vs.* RHE in 0.5 M H_2SO_4 aqueous solution; scan rate=100 mV s^{-1} at room temperature.

The averaged area ($A_{average}$) to find one Ru center (cm^2 per site) can be calculated by dividing the PtRu/PF and $PtRu_2$/PF catalysts' ECSA values by the value of n (Ru sites per cm^2). This gives $A_{average}$ values of 7.34×10^{-15} and 5.25×10^{-15} cm^2 per Ru for PtRu/PF and $PtRu_2$/PF, respectively. The reciprocal of $A_{average}$ per site gives the active sites density (sites / cm^2) [50]. Based on this, active sites density values of 1.36×10^{13} and 1.9×10^{14} sites/cm^2 were estimated for PtRu/PF and $PtRu_2$/PF, respectively. Following the same sequence of calculations for the two catalysts with the individual active materials, namely Ru/PF and Pt/PF (where Q values of 0.88×10^{-3} and 1.36×10^{-3} C were recorded for Ru/PF and Pt/PF, respectively) gave active sites density values of 6.89×10^{11} and 7.04×10^{12} sites/cm^2, respectively. These results provide an additional evidence for the effective catalytic impact of Ru in the PtRu/PF catalyst, which further enhanced with increasing Ru content, as in the $PtRu_2$/PF catalyst which exhibited the best catalytic performance amongst the prepared electrocatalysts.

2.3.5 Direct methanol oxidation

Direct methanol fuel cells (DMFCs) are efficient energy conversion systems operating at ambient temperature. As methanol oxidation reaction (MOR) is the common anode reaction in DMFCs, the design of highly efficient catalysts for MOR is very important to achieve high energy/power density fuel cells. **Figure 8** shows the MOR catalytic activity of the developed catalysts acquired in H_2SO_4 (0.5 M) aqueous solution + CH_3OH (0.5 M) at a sweep rate of 20 mV s^{-1}. In the anodic polarization, the MOR should display two evident oxidation peaks: one is ascribed to methanol oxidation at higher potential (I_f), and another one assigned to carbonaceous species oxidation at lower potential (I_b). The MOR peak current density of $PtRu_2$/PF catalyst was found to be 35 mA/cm^2, which is higher than that of PtRu/PF catalyst (32 mA/cm^2) with more Pt content (**Figure 8A**). The higher I_f/I_b ratio correlates with methanol effective oxidation into CO_2 during the forward potential scan, generating limited amount of poisoning species. The $PtRu_2$/PF catalyst has an appreciable I_f/I_b ratio of 2.4, which is larger than that of the standard 20% Pt/C (2.1) catalyst.

Evaluation of the current density change with continuous potential cycling further confirmed the excellent stability of the $PtRu_2$/PF catalyst. **Figure 8B** displays the long-term accelerated durability test of the $PtRu_2$/PF catalyst under continuous potential cycling (scan rate = 100 mV s^{-1}). The CVs, recorded after 500 and 1000 potential cycles, clearly indicate that there is no apparent loss in the current density up to 1000 potential cycles for $PtRu_2$/PF catalyst. The excellent long-term catalytic stability was also confirmed by the chronoamperometry test at +0.72 V *vs.* SCE for 6 h (**inset Figure 8B**). The inset showed a current density retention of 95.8% after 2 h, which slightly decreased to ~91% after 6 h.

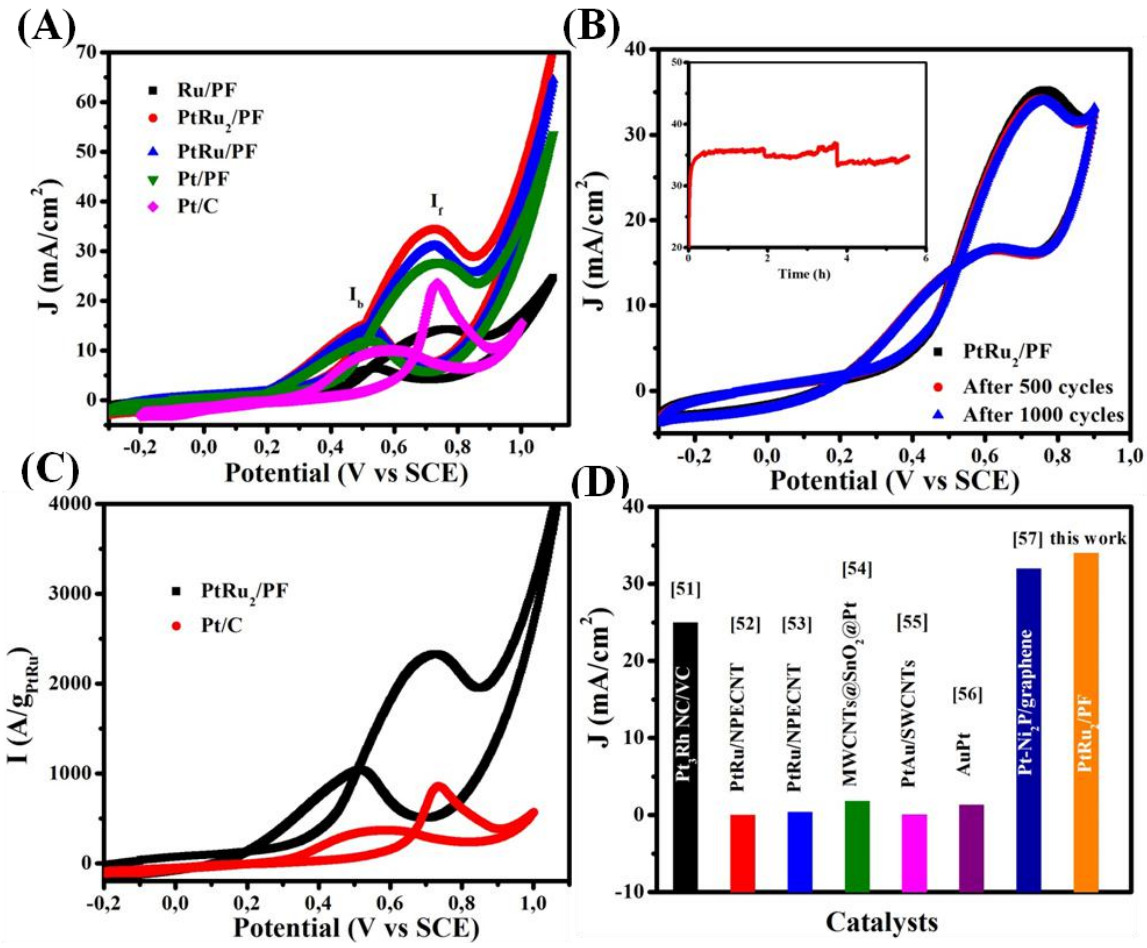

Figure 8. Electrocatalytic performance of the prepared $PtRu_2$/PF, PtRu/PF, Ru/PF, Pt/PF, and commercial 20% Pt/C catalysts. (A) CV curves acquired in H_2SO_4 (0.5 M) + CH_3OH (0.5 M) solution, sweep rate=20 mV s^{-1}. (B) CVs of the $PtRu_2$/PF catalyst before and after 500 and 1000 potential cycles, sweep rate=100 mV s^{-1}; the inset is the chronoamperometry (CA) curve measured in H_2SO_4 (0.5 M) + CH_3OH (0.5 M) at +0.72 V *vs.* SCE for 6 h. (C) Mass activity plots for $PtRu_2$/PF and 20% Pt/C with respect to the loading of the active metal Pt. (D) Comparison of mass activities of MOR for Pt-based catalysts [51-57].

Figure 8C reveals that the $PtRu_2$/PF catalyst had a peak mass activity of 2327 A/g (for the loading noble metal mass Ru and Pt), which is ~ 3.2 times larger than that of the commercial 20% Pt/C catalyst. Meanwhile, the forward scanning peak potential toward methanol oxidation of the $PtRu_2$/PF (+0.72 V) is lower than that of commercial 20% Pt/C (+0.76 V)

catalyst, which further indicates that $PtRu_2$/PF is capable to efficiently decrease the overpotential of methanol oxidation. More importantly, the onset potential of $PtRu_2$/PF (0.21 V), is obviously much lower than that of commercial 20% Pt/C catalyst (0.32 V), indicating its suitability for methanol electro-oxidation.

Figure 8D compares the MOR activity of $PtRu_2$/PF catalyst with respect to other Pt-based MOR benchmark catalysts [51-57]. The $PtRu_2$/PF catalyst exhibits the highest current value even though most of these electrocatalysts are known to display high loading amounts or large surface areas. The results clearly highlight the favorable features of $PtRu_2$/PF catalyst for MOR.

2.3.6 OER and ORR tests

Oxygen evolution reaction (OER) and oxygen reduction reaction (ORR) are also the key processes in electrochemical energy storage and energy conversion applications. In this line, the electrocatalytic performance of $PtRu_2$/PF catalyst was investigated for OER in KOH (1.0 M) aqueous solution. **Figure 9A** depicts the LSV curves of Ru/PF, $PtRu_2$/PF, PtRu/PF, Pt/PF and commercial 20% Pt/C catalysts at 5 mV s^{-1}. In a comparison with Ru/PF (305 mV), Pt/PF (390 mV), and RuO_2 (280 mV) catalysts at 10 mA cm^{-2}, PtPtRu/PF and $PtPtRu_2$/PF catalysts achieved enhanced OER activity with overpotential values close to 270 mV at the same current density. These results reveal the promising OER catalytic performance of PtPtRu/PF and $PtPtRu_2$/PF catalysts thus, highlighting the effective catalytic influence of Ru on the OER too. According to the literature, the OER mechanism in alkaline electrolytes over a catalytically active site (*S**) can be represented by Eqs. 4-7 [58].

$$OH^- + S^* \rightarrow S^*OH + e^- \quad (4)$$

$$S^*OH + OH^- \rightarrow S^*O^- + H_2O \quad (5)$$

$$S^*O^- \rightarrow S^*O + e^- \quad (6)$$

$$S^*O + S^*O \rightarrow S^* + S^* + O_2 \quad (7)$$

OH^- adsorption on S^* is found to play a fundamental role in enhancing the OER kinetics [M1]. Such catalytically active site (S^*) is proven to accelerate the adsorption and desorption of the OH^- anions [58]. Electrochemical characterizations shown above revealed the efficacious catalytic role of Ru in the PtRu/PF catalyst, which further enhanced with increase in Ru content, in accelerating the OER kinetics. Based on this, the Ru atoms in the PtRu/PF catalyst are expected to act as active catalytic sites for the OER *via* hastening the adsorption and desorption of the OH^- anions. This, in turn, boosts the kinetics of the OER, resulting in reduced Tafel slopes values [58]. PtRu/PF and $PtRu_2$/PF catalysts recorded reduced Tafel slope values of 79 mV dec^{-1}. This value is very close to that measured here for the OER state-of-the-art electrocatalyst, namely RuO_2 (78 mV dec^{-1}), suggesting fast OER kinetics on PtRu/PF and $PtRu_2$/PF catalysts (**Fig. 9B**).

The PtRu/PF and $PtRu_2$/PF catalysts' OER mass activities were also calculated to further confirm their outstanding catalytic performance compared with the other tested electrocatalysts. Mass activity of the OER is given by the ratio j/c, where j is the current density produced at a specific potential and c is the catalyst loading density on the GC electrode, 0.143×10^{-3} g cm^{-2}. Pt/PF, Ru/PF, PtRu/PF, and $PtRu_2$/PF catalysts generated an anodic current density of 0.057, 0.094, 0.16, 0.18 A cm^{-2} at 1.8 V *vs.* RHE, respectively. Based on this, OER mass activities of 398.6, 657.3, 1119, and 1259 A g^{-1} were calculated for Pt/PF, Ru/PF, PtRu/PF, and $PtRu_2$/PF catalysts, respectively. The PtRu/PF, and $PtRu_2$/PF catalysts's mass activities (1119, and 1259 A g^{-1} @ 1.8 V *vs.* RHE) exceeded that of the state-of-the-art RuO_2 catalyst (807 A g^{-1}, with 0.115 A cm^{-2} generated @ 1.8 V *vs.* RHE), thus confirming the outstanding catalytic activity of the PtRu/PF, and $PtRu_2$/PF catalysts for the OER.

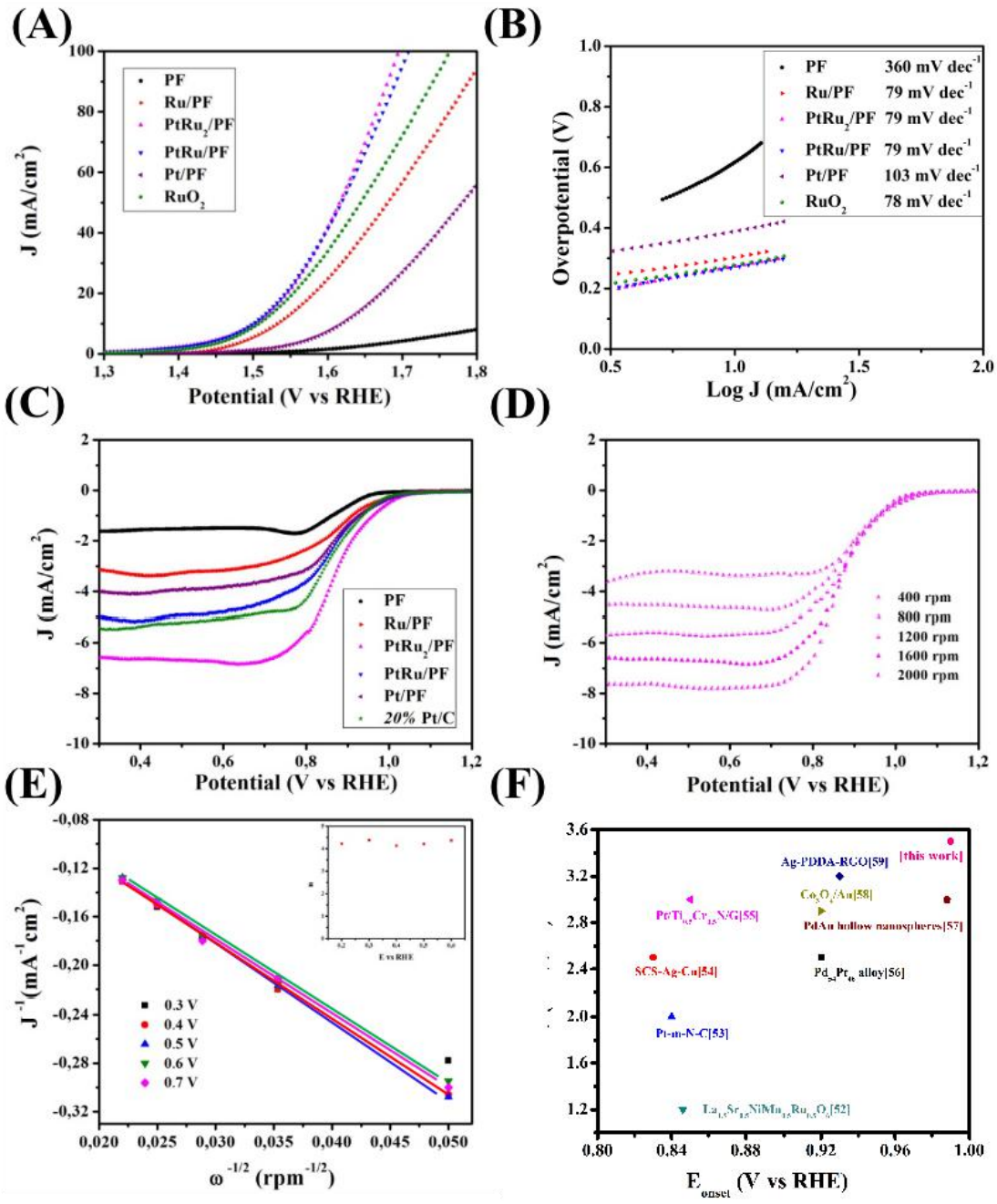

Figure 9. (A) OER polarization curves of Ru/PF, $PtRu_2$/PF, PtRu/PF, Pt/PF, and commercial 20% Pt/C catalysts. (B) The corresponding Tafel plots calculated from LSV curves in (A). (C) ORR polarization curves of different catalysts with RDE speed =1600 rpm in O_2-saturated KOH (0.1 M) solution, scan rate =20 mV s^{-1}. (D) RDE polarization curves for ORR on $PtRu_2$/PF in O_2-saturated KOH (0.1 M), n=20 mV s^{-1}. (E) K-L plots for ORR in KOH (0.1 M); the inset shows the potential dependence of n. (F) Comparison of the onset potential and current density values of recent reports in KOH (0.1 M) aqueous solution.

The LSV measurements are also conducted in O_2-saturated 0.1 M KOH electrolyte without rotation at a sweeping rate of 20 mV s^{-1} (**Figure 9C**). The $PtRu_2$/PF displayed the highest current intensity and onset potential among all the catalysts. The onset potential (E_{onset}) is regarded as the potential recorded at a current density of -1 mA cm^{-2} in the LSV. The E_{onset} of $PtRu_2$/PF (0.96 V) is positive than those of PtRu/PF (0.93 V), Pt/PF catalyst (0.92 V), 20% Pt/C (0.94 V), and Ru/PF (0.91 V) *vs.* RHE.

Furthermore, we performed the rotating disk electrode (RDE) polarization curves of the $PtRu_2$/PF catalyst in 0.1 M KOH to gain more insights about the ORR kinetics and catalytic mechanism in alkaline medium from 400-2000 rpm (**Figure 9D**). The limit current density increases from 3.4 to 7.7 mA·cm^{-2} as the rotating speed was varied from 400 to 2000 rpm; it is well established that the high speeds shorten the O_2 diffusion distance in the O_2-saturated electrolyte. The corresponding Koutecky-Levich (K-L) plots (**Figure 9E**) within the 0.2 to 0.6 V potential range *vs.* RHE display good linearity, which confirms first-order reaction kinetics, and the number of electrons transferred (n) during the reaction are the same at different potentials. Additionally, the value of n is 3.9 ~ 4.1 over the investigated potential window, suggesting that the $PtRu_2$/PF catalyst follows the 4 electrons-transfer pathway, which corresponds to a complete reduction of oxygen into water and only little peroxide is formed.

Figure 9F summarizes the ORR [59-66] kinetic data of recent electrodes in 0.1 M KOH alkaline solution. It is obvious that $PtRu_2$/PF electrode represents one of the most active electrocatalysts even though most of these noble metal electrocatalysts consist of nanomaterials with high loading amounts, and display large surface areas.

2.4 Conclusion

We have successfully assessed the ultimate limit of Pt in PtRu/PF catalysts *via* a facile hydrothermal approach. The high dispersibility and bimetallic synergy make the $PtRu_2$/PF catalyst have an outstanding HER and MOR electrocatalytic activity in acid conditions,

considerably better than those reported using a regular Pt-based and commercial 20% Pt/C catalysts. Furthermore, the $PtRu_2$/PF displayed excellent ORR performance with an onset potential of 0.96 V *vs.* RHE, and a limit current density of 6.5 $mA \cdot cm^{-2}$, which is better than that of commercial 20% Pt/C (5.3 $mA \cdot cm^{-2}$). Additionally, the $PtRu_2$/PF also has a superior OER activity. Given that Pt is the most commonly investigated catalyst for many catalytic applications, the results obtained in the present study provide an interesting alternative route to prepare Pt-based catalysts with minimal Pt loading and enhanced electrocatalytic activity. This holds promise for the development of highly efficient and cost-effective electrocatalysts for various electrocatalytic applications.

2.5 References

[1] Bai, S.; Wang, C.; Deng, M.; Gong, M.; Bai, Y.; Jiang, J.; Xiong, Y. Surface polarization matters: enhancing the hydrogen-evolution reaction by shrinking Pt shells in Pt-Pd-graphene stack structures. Angew. Chem. Int. Ed. 2014, 53, 12120-12124.

[2] Zhang, L.; Wang, L.; Holt, C. M. B.; Zahiri, B.; Li, Z.; Malek, K.; Navessin, T.; Eikerling, M. H.; Mitlin, D. Highly corrosion resistant platinum-niobium oxide-carbon nanotube electrodes for the oxygen reduction in PEM fuel cells. Energy Environ. Sci. 2012, 5, 6156-6172.

[3] Yang, C.; Zhou, M.; Xu, Q. Confining Pt nanoparticles in porous carbon structures for achieving durable electrochemical performance. Nanoscale 2014, 6, 11863-11870.

[4] Lin, H.; Li, H.; Li, Y.; Liu, J.; Wang, X.; Wang, L. Hierarchical CoS/MoS_2 and Co_3S_4/MoS_2/Ni_2P nanotubes for efficient electrocatalytic hydrogen evolution in alkaline media. J. Mater. Chem. A 2017, 5, 25410-25419.

[5] Ren, X.; Pang, L.; Zhang, Y.; Ren, X.; Fan, H.; Liu, S. One-step hydrothermal synthesis of monolayer MoS_2 quantum dots for highly efficient electrocatalytic hydrogen evolution. J. Mater. Chem. A 2015, 3, 10693-10697.

[6] Pang, L.; Barras, A.; Zhang, Y.; Amin, M. A.; Addad, A.; Szunerits, S.; Boukherroub, R. CoO Promoted the Catalytic Activity of Nitrogen-doped MoS_2 Supported on Carbon Fiber Mats for Overall Water Splitting. ACS Appl. Mater. Interfaces 2019, 11, 31889-31898.

[7] Liu, Y.; Jiang, S.; Li, S.; Zhou, L.; Li, Z.; Li, J.; Shao, M. Interface engineering of (Ni, Fe)S_2@MoS_2 heterostructures for synergetic electrochemical water splitting. Appl. Catal. B 2019, 247, 107-114.

[8] Isarain-Chavez, E.; Baro, M. D.; Alcantara, C.; Pane, S.; Sort, J.; Pellicer, E. Micelle-Assisted Electrodeposition of Mesoporous Fe-Pt Smooth Thin Films and their Electrocatalytic Activity towards the Hydrogen Evolution Reaction. ChemSusChem 2018, 11, 367-375.

[9] Dai, Z.; Geng, H.; Wang, J.; Luo, Y.; Li, B.; Zong, Y.; Yang, J.; Guo, Y.; Zheng, Y.; Wang, X.; Yan, Q. Hexagonal-Phase Cobalt Monophosphosulfide for Highly Efficient Overall Water Splitting. ACS Nano 2017, 11, 11031-11040.

[10] Liu, Z.; Qi, J.; Liu, M.; Zhang, S.; Fan, Q.; Liu, H.; K. Liu, Zheng, H.; Yin, Y.; Gao, C. Aqueous Synthesis of Ultrathin Platinum/Non-Noble Metal Alloy Nanowires for Enhanced Hydrogen Evolution Activity. Angew. Chem. Int. Ed. 2018, 57, 11678-11682.

[11] Zhang, Z.; Liu, G.; Cui, X.; Chen, B.; Zhu, Y.; Gong, Y.; Saleem, F.; Xi, S.; Du, Y.; Borgna, A.; Lai, Z.; Zhang, Q.; Li, B.; Zong, Y.; Han, Y.; Gu, L.; Zhang, H. Crystal Phase and Architecture Engineering of Lotus-Thalamus-Shaped Pt-Ni Anisotropic Superstructures for Highly Efficient Electrochemical Hydrogen Evolution. Adv. Mater. 2018, 30, 1801741.

[12] Kuang, P.; Tong, T.; Fan, K.; Yu, J. In Situ Fabrication of Ni-Mo Bimetal Sulfide Hybrid as an Efficient Electrocatalyst for Hydrogen Evolution over a Wide pH Range. ACS Catal. 2017, 7, 6179-6187.

[13] Zeng, M.; Li, Y.; Recent Advances in Heterogeneous Electrocatalysts for Hydrogen Evolution Reaction. J. Mater. Chem. A 2015, 3, 14942-14962.

[14] Chaudhari, N. K.; Hong, Y.; Kim, B.; Choi, S. -I.; Lee, K. Pt-Cu based nanocrystals as promising catalysts for various electrocatalytic reactions. J. Mater. Chem. A 2019, 7, 17183-17203.

[15] Pei, J.; Mao, J.; Liang, X.; Zhuang, Z.; Chen, C.; Peng, Q.; Wang, D.; Li, Y. Ultrathin Pt-Zn Nanowires: High-Performance Catalysts for Electrooxidation of Methanol and Formic Acid. ACS Sustain. Chem. Eng. 2017, 6, 77-81.

[16] El Sawy, E. N.; Birss, V. I. Nanoengineered $Ir_{core}@Pt_{shell}$ Nanoparticles with Controlled Pt Shell Coverages for Direct Methanol Electro-Oxidation. ACS Appl. Mater. Interfaces 2018, 10, 3459-3469.

[17] Pang, L.; Li, M.; Ma, Q.; Zhang, Y.; Ren, X.; Zhang, D.; Liu, S. F. Controlled Pt Monolayer Fabrication on Complex Carbon Fiber Structures for Superior Catalytic Applications. Electrochim. Acta 2016, 222, 1522-1527.

[18] Pang, L.; Zhang, Y.; Liu, S. Monolayer-by-monolayer growth of platinum films on complex carbon fiber paper structure. Appl. Sur. Sci. 2017, 407, 386-390.

[19] Li, M.; Ma, Q.; Liu, X.; Zhu, X.; Liu, S. Pt monolayer coating on complex network substrate with high catalytic activity for the hydrogen evolution reaction. Sci. Adv. 2015, 1, e1400268.

[20] Chi, J. Q.; Xie, J. Y.; Zhang, W. W.; Dong, B.; Qin, J. F.; Zhang, X. Y.; Lin, J. H.; Chai, Y. M.; Liu, C. G. N-Doped Sandwich-Structured $Mo_2C@C@Pt$ Interface with Ultralow Pt Loading for pH-Universal Hydrogen Evolution Reaction. ACS Appl. Mater. Interfaces 2019, 11, 4047-4056.

[21] Liao, F.; Shen, W.; Sun, Y.; Li, Y.; Shi, H.; Shao, M. Nanosponge Pt Modified Graphene Nanocomposites Using Silicon Monoxides as a Reducing Agent: High Efficient Electrocatalysts for Hydrogen Evolution. ACS Sustain. Chem. Eng. 2018, 6, 15238-15244.

[22] Shang, X.; Liu, Z. Z.; Lu, S. S.; Dong, B.; Chi, J. Q.; Qin, J. F.; et al. Pt-C Interfaces Based on Electronegativity-Functionalized Hollow Carbon Spheres for Highly Efficient Hydrogen Evolution. ACS Appl. Mater. Interfaces 2018, 10, 43561-43569.

[23] Theerthagiri, J.; Cardoso, E. S. F.; Fortunato, G. V.; Casagrande, G. A.; Senthilkumar, B.; Madhavan, J.; Maia, G. Highly Electroactive Ni Pyrophosphate/Pt Catalyst toward Hydrogen Evolution Reaction, ACS Appl. Mater. Interfaces 2019, 11, 4969-4982.

[24] Zhang, L.; Doyle-Davis, K.; Sun, X. Pt-Based electrocatalysts with high atom utilization efficiency: from nanostructures to single atoms. Energy Environ. Sci. 2019, 12, 492-517.

[25] Bhange, S. N.; Unni, S. M.; Kurungot, S. Nitrogen and sulphur co-doped crumbled graphene for the oxygen reduction reaction with improved activity and stability in acidic medium. J. Mater. Chem. A 2016, 4, 6014-6020.

[26] Liu, X.; Zhou, W.; Yang, L.; Li, L.; Zhang, Z.; Ke, Y.; Chen, S. Nitrogen and sulfur co-doped porous carbon derived from human hair as highly efficient metal-free electrocatalysts for hydrogen evolution reactions. J. Mater. Chem. A 2015, 3, 8840-8846.

[27] Xu, Y.; Yin, S.; Li, C.; Deng, K.; Xue, H.; Li, X.; Wang, H.; Wang, L. Low-ruthenium-content NiRu nanoalloys encapsulated in nitrogen-doped carbon as highly efficient and pH-universal electrocatalysts for the hydrogen evolution reaction. J. Mater. Chem. A 2018, 6, 1376-1381.

[28] Liu, J.; Zheng, Y.; Zhu, D.; Vasileff, A.; Ling, T.; Qiao, S. Z. Identification of pH-dependent synergy on Ru/MoS_2 interface: a comparison of alkaline and acidic hydrogen evolution. Nanoscale 2017, 9, 16616-16621.

[29] Shi, J.; Zhao, M.; Wang, Y.; Fu, J.; Lu, X.; Hou, Z.; Upgrading of aromatic compounds in bio-oil over ultrathin graphene encapsulated Ru nanoparticles. J. Mater. Chem. A 2016, 4, 5842-5848.

[30] Benson, J.; Li, M.; Wang, S.; Wang, P.; Papakonstantinou, P. Electrocatalytic Hydrogen Evolution Reaction on Edges of a Few Layer Molybdenum Disulfide Nanodots. ACS Appl. Mater. Interfaces 2015, 7, 14113-22.

[31] Sapountzia, F. M.; Gracia, J. M.; Weststrate, C. J.; Fredriksson, H. O. A.; Niemantsverdriet, J. W. Electrocatalysts for the generation of hydrogen, oxygen and synthesis gas. Prog. Energy Combust. Sci. 2017, 58, 1-35.

[32] Safizadeh, F.; Ghali, E.; Houlachi, G. Electrocatalysis developments for hydrogen evolution reaction in alkaline solutions-A Review. Inter. J. Hydrogen Energy 2015, 40, 256-274.

[33] Fang, Y.-H.; Liu, Z.-P. Tafel Kinetics of Electrocatalytic Reactions: From Experiment to First-Principles. ACS Catal. 2014, 4, 4364-4376.

[34] Drouet, S.; Creus, J.; Colliere, V.; Amiens, C.; Garcia-Anton, J.; Sala, X.; Philippot, K. A porous Ru nanomaterial as an efficient electrocatalyst for the hydrogen evolution reaction under acidic and neutral conditions. Chem. Commun. 2017, 53, 11713-11716.

[35] Murthy, A. P.; Theerthagiri, J.; Madhavan, J. Insights on Tafel Constant in the Analysis of Hydrogen Evolution Reaction. J. Phys. Chem. C 2018, 122, 23943-23949.

[36] Lin, C.; Batchelor-McAuley, C.; Laborda, E.; Compton, R. G. Tafel-Volmer Electrode Reactions: The Influence of Electron-Transfer Kinetics. J. Phys. Chem. C 2015, 119, 22415-22424.

[37] Ren, W.; Zhang, H.; Cheng, C. Ultrafine Pt nanoparticles decorated MoS_2 nanosheets with significantly improved hydrogen evolution activity. Electrochim. Acta 2017, 241, 316-322.

[38] Liao, L.; Wang, S.; Xiao, J.; Bian, X.; Zhang, Y.; Scanlon, M. D.; Hu, X.; Tang, Y.; Liu, B.; Girault, H. A nanoporous molybdenum carbide nanowire as an electrocatalyst for hydrogen evolution reaction. Energy Environ. Sci. 2014, 7, 387-392.

[39] Shervedani, R. K.; Madram, A. R. Kinetics of hydrogen evolution reaction on nanocrystalline electrodeposited $Ni_{62}Fe_{35}C_3$ cathode in alkaline solution by electrochemical impedance spectroscopy. Electrochim. Acta 2007, 53, 426-433.

[40] Kalasapurayil Kunhiraman, A.; Ramasamy, M.; Ramanathan, S. Efficient hydrogen evolution catalysis triggered by electrochemically anchored platinum nano-islands on functionalized-MWCNT. Inter. J. Hydrogen Energy 2017, 42, 9881-9891.

[41] Sun, M.; Liu, H.; Qu, J.; Li, J. Earth-Rich Transition Metal Phosphide for Energy Conversion and Storage. Adv. Energy Mater. 2016, 6, 1600087.

[42] Farsak, M.; Telli, E.; Tezcan, F.; Akgül, F. S.; Yüce, A. O.; Kardaş, G. The electrocatalytic properties of lithium copper composite in the oxygen reduction reaction. Electrochim. Acta 2014, 148, 276-282.

[43] Telli, E.; Farsak, M.; Kardaş, G. Investigation of noble metal loading CoWZn electrode for HER. Int. J. Hydrogen Energy 2017, 42, 23260-23267.

[44] Orazem, M. E.; Pébère, N.; Tribollet, B. Enhanced Graphical Representation of Electrochemical Impedance Data. J. Electrochem. Soc. 2006, 153, B129.

[45] Fan, G.; Liu, Q.; Tang, D.; Li, X.; Bi, J.; Gao, D. Nanodiamond supported Ru nanoparticles as an effective catalyst for hydrogen evolution from hydrolysis of ammonia borane. Int. J. Hydrogen Energy 2016, 41, 1542-1549.

[46] Diez-Garcia, M. I.; Gomez, R. Investigating Water Splitting with $CaFe_2O_4$ Photocathodes by Electrochemical Impedance Spectroscopy. ACS Appl. Mater. Interfaces 2016, 8, 21387-97.

[47] Benck, J. D.; Chen, Z.; Kuritzky, L. Y.; Forman, A. J.; Jaramillo, T. F. Amorphous Molybdenum Sulfide Catalysts for Electrochemical Hydrogen Production: Insights into the Origin of their Catalytic Activity. ACS Catal. 2012, 2, 1916-1923.

[48] Kibsgaard, J.; Jaramillo, T. F. Molybdenum phosphosulfide: an active, acid-stable, earth-abundant catalyst for the hydrogen evolution reaction. Angew. Chem. Int. Ed. 2014, 53, 14433-14437

[49] Liu, Y.; Shang, X.; Gao, W.; Dong, B.; Chi, J.; Li, X.; Yan, K.; Chai, Y.; Liu, Y.; Liu, C. Ternary CoS_2/MoS_2/RGO Electrocatalyst with CoMoS Phase for Efficient Hydrogen Evolution. Appl. Surf. Sci. 2017, 412, 138-145.

[50] Sabhapathy, P.; Liao, C.; Chen, W.; Chou, T.; Shown, I.; Sabbah, A.; Lin, Y.; Lee, J.; Tsai, M.; Chen, K.; Chen, L. Highly efficient nitrogen and carbon coordinated N-Co-C electrocatalysts on reduced grapheme oxide derived from vitamin-B12 for the hydrogen evolution reaction. J. Mater. Chem. A 2019, 7, 7179- 7185.

[51] Narayanamoorthy, B.; Datta, K. K. R.; Eswaramoorthy, M.; Balaji, S. Highly Active and Stable Pt_3Rh Nanoclusters as Supportless Electrocatalyst for Methanol Oxidation in Direct Methanol Fuel Cells. ACS Catal. 2014, 4, 3621-3629.

[52] Ghosh, A.; Ramaprabhu, S. An efficient and durable novel catalyst support with superior electron-donating properties and fuel diffusivity for a direct methanol fuel cell. Catal. Sci. Technol. 2017, 7, 5079-5091.

[53] Li, B.; Higgins, D. C.; Zhu, S.; Li, H.; Wang, H.; Ma, J.; Chen, Z. Highly active Pt-Ru nanowire network catalysts for the methanol oxidation reaction. Catal. Commun. 2012, 18, 51-54.

[54] Huang, M.; Zhang, J.; Wu, C.; Guan, L. Pt Nanoparticles Densely Coated on SnO_2-Covered Multiwalled Carbon Nanotubes with Excellent Electrocatalytic Activity and Stability for Methanol Oxidation. ACS Appl. Mater. Interfaces 2017, 9, 26921-26927.

[55] You, G.; Jiang, J.; Li, M.; Li, L.; Tang, D.; Zhang, J.; Zeng, X.C.; He, R. PtPd (111) Surface versus PtAu (111) Surface: Which One Is More Active for Methanol Oxidation. ACS Catal. 2017, 8, 132-143.

[56] Chatterjee, D.; Shetty, S.; Muller-Caspary, K.; Grieb, T.; Krause, F. F.; Schowalter, M.; Rosenauer, A.; Ravishankar, N. Ultrathin Au-Alloy Nanowires at the Liquid-Liquid Interface. Nano Lett. 2018, 18, 1903-1907.

[57] Cao, J.; Chen, H.; Zhang, X.; Zhang, Y.; Liu, X. Graphene-supported platinum/nickel phosphide electrocatalyst with improved activity and stability for methanol oxidation. RSC Adv. 2018, 8, 8228-8232.

[58] Suen, N.-T.; Hung, S.-F.; Quan, Q.; Zhang, N.; Xu,Y.-J.; Chen, H.-M. Electrocatalysis for the Oxygen Evolution Reaction: Recent Development and Future Perspectives. Chem. Soc. Rev. 2017, 46, 337-365.

[59] Retuerto, M.; Calle-Vallejo, F.; Pascual, L.; Lumbeeck, G.; Fernandez-Diaz, M. T.; Croft, M.; Gopalakrishnan, J.; Pena, M. A.; Hadermann, J.; Greenblatt, M.; Rojas, S. $La_{1.5}Sr_{0.5}NiMn_{0.5}Ru_{0.5}O_6$ Double Perovskite with Enhanced ORR/OER Bifunctional Catalytic Activity. ACS Appl Mater Interfaces 2019, 11, 21454-21464.

[60] Gao, S.; Fan, H.; Wei, X.; Li, L.; Bando, Y.; Golberg, D. Nitrogen-Doped Carbon with Mesopore Confinement Efficiently Enhances the Tolerance, Sensitivity, and Stability of a Pt Catalyst for the Oxygen Reduction Reaction. Part. Part. Syst. Charact. 2013, 30, 864-872.

[61] Ashok, A.; Kumar, A.; Matin, M. A.; Tarlochan, F. Probing the effect of combustion controlled surface alloying in silver and copper towards ORR and OER in alkaline medium. J. Electroanal. Chem. 2019, 844, 66-77.

[62] Liu, B.; Huo, L.; Si, R.; Liu, J.; Zhang, J. A General Method for Constructing Two-Dimensional Layered Mesoporous Mono- and Binary-Transition-Metal Nitride/Graphene

as an Ultra-Efficient Support to Enhance Its Catalytic Activity and Durability for Electrocatalytic Application. ACS Appl. Mater. Interfaces 2016, 8, 18770-18787.

[63] Jukk, K.; Kongi, N.; Tammeveski, K.; Solla-Gullón, J.; Feliu, J. M. Electroreduction of Oxygen on PdPt Alloy Nanocubes in Alkaline and Acidic Media. ChemElectroChem 2017, 4, 2547-2555.

[64] Jiao, W.; Chen, C.; You, W.; Chen, G.; Xue, S.; Zhang, J.; Liu, J.; Feng, Y.; Wang, P.; Wang,Y.; Wen, H.; Che, R. Tuning strain effect and surface composition in PdAu hollow nanospheres as highly efficient ORR electrocatalysts and SERS substrates. Appl. Catal. B: Environ. 2020, 262, 118298.

[65] Liu, L.; Wei, Q.; Yu, X.; Zhang, Y. Metal-Organic Framework-Derived Co_3O_4/Au Heterostructure as a Catalyst for Efficient Oxygen Reduction. ACS Appl. Mater. Interfaces 2018, 10, 34068-34076.

[66] Men, B.; Sun, Y.; Tang, Y.; Zhang, L.; Chen, Y.; Wan, P.; Pan, J. Highly Dispersed Ag-Functionalized Graphene Electrocatalyst for Oxygen Reduction Reaction in Energy-Saving Electrolysis of Sodium Carbonate. Ind. Eng. Chem. Res. 2015, 54, 7415-7422.

CHAPTER 3

CoO Promoted the Catalytic Activity of Nitrogen-Doped MoS_2 Supported on Carbon Fibers for Overall Water Splitting

3.1 Introduction

Electrochemical water splitting represents one the most relevant technologies to meet the increased global demand for clean and sustainable energy [1-3]. Electrocatalytic systems for effective water splitting typically explore the outstanding catalytic properties of noble metals (Pt, Ir and Ru) to accelerate the two half reactions of the water-splitting process, i.e., the hydrogen evolution reaction (HER) at the cathode and the oxygen evolution reaction (OER) at the anode, due to the sluggish kinetics of both processes [4-6]. However, the availability and high cost of these noble metals inhibit their application in commercial processes. Therefore, there is a continuous quest for innovative approaches for the preparation of highly efficient and stable electrocatalysts using low cost and earth-abundant materials [7-9].

In the last decades, non-noble metal materials including transition-metal chalcogenides [10-12], phosphides [13-15], carbides [16, 17] and complexes as well as metal alloys [18] have proven to be promising alternatives to precious metals-based electrocatalysts. The ongoing research efforts are currently focused on the design of highly efficient OER or HER electrocatalysts with the aim to accelerate the two half reactions of the water-splitting process, or coupling existing HER and OER electrocatalysts that can operate in the same electrolytic composition for overall water splitting [15, 19]. From the practical viewpoint, the development of bifunctional electrocatalysts for overall water splitting represents one of the most technologically relevant strategies. However, to simultaneously create active sites for HER and OER on a single catalyst encounters still serious challenges.

Recently, many reports highlighted the outstanding HER activity of chalcogenides of W [20], Mo [21], Co [22], and Ni [23] electrocatalysts, owing to their enhanced electrical conductivity compared to other materials. Particularly, nanosized MoS_2-based electrocatalysts have generated huge attention, owing to their two-dimensional permeable ion transportation channels and enhanced electrocatalytic activity [24]. The Mo and S atoms in MoS_2 have strong ionic bonding, with the different layers of MoS_2 interacting *via* van der Waals forces [25]. It is now well-established that layered MoS_2 is a good HER electrocatalyst, but exhibits a very poor OER activity, which inhibits its usage as a bifunctional electrocatalyst for overall water splitting [26].

Recent studies have underlined the importance of Fe, Co, Ni element doping into MoS_2 to tune its electronic structure, improve its electrical conductivity and decrease the hydrogen adsorption free energy for HER [27-29]. However, most of these related reports have primarily focused on the enhancement of MoS_2 HER activity, while ignoring its OER activity. Additionally, both theoretical and experimental investigations revealed the direct correlation of the MoS_2 HER activity with the number of unsaturated Mo-S sites along the edges [30]. Thus, one of the main techniques for achieving high HER activity of MoS_2 consists of increasing the maximum number of exposed edge sites and enhancing the intrinsic activity of the edge sites by chemical doping.

In this work, we adopted an original approach to develop a bifunctional MoS_2-based electrocatalyst for overall water splitting. To enhance the HER activity, the inert basal plane of 2D MoS_2 was activated *via* chemical doping with nitrogen. The nitrogen-doped MoS_2 electrocatalyst supported on carbon fibers (N-MoS_2/CF) possessed improved hydrogen evolution than the non-doped MoS_2/CF [31]. The cobalt (Co)-based compounds are considered as promising candidates because of their high intrinsic catalytic activity, low-cost, earth abundance, and environmentally friendly nature. Particularly, cobalt oxides are

generally employed as one of the most promising anode materials due to their high theoretical capacity, easy fabrication, recyclability, and high stability. Furthermore, to improve the OER activity of N-MoS_2 additional coupling with CoO was performed. CoO hybridization with N-doped MoS_2 generated additional OER active sites, ensuring bifunctional activity needed for overall water splitting. The CoO/N-MoS_2 electrocatalyst supported on carbon fibers (CoO/N-MoS_2/CF) was synthesized by a facile hydrothermal method and electrochemical deposition technique. The experimental results demonstrated that CoO/N-MoS_2/CF exhibited enhanced OER and HER activities in alkaline medium with good stability. The bifunctionality of CoO/N-MoS_2/CF was further exploited to perform water splitting. The alkaline electrolyzer delivered a maximum current density of 53 mA cm^{-2} at an applied cell voltage of 1.5 V. These results are promising for practical application of the developed electrocatalyst for overall water splitting.

3.2 Experimental section

3.2.1 Preparation of N-MoS_2/CF electrocatalyst

Typically, 0.27 g of Na_2MoO_4 and 1.5 g of thiourea were added to 35 mL of Milli-Q (MQ) water under magnetic stirring for 1 h to form a homogeneous solution. And then 0.3, 0.5 or 0.8 g of ammonium fluoride was added to above solution, respectively (**Figure 1**). Before MoS_2 deposition, the carbon fiber (CF, 1 cm × 5 cm) was annealed for 30 min in air at 400 °C to remove the organic binder on the fiber surface, followed by an activation step (boiling in 40% nitric acid solution) for 30 min. Then, the resulting CF was immersed in the above solution, sonicated for 1 h, and subsequently transferred into a Teflon-lined stainless-steel autoclave for hydrothermal treatment at 250 °C. After 24 h, the autoclave was cooled down to room temperature and then the formed N-MoS_2/CF was copiously rinsed with ethanol and MQ water to remove excess reagents and dried at 60 °C overnight.

3.2.2 Preparation of CoO/N-MoS_2/CF electrocatalyst.

CoO was electrochemically deposited on the N−MoS_2/CF substrate using an aqueous solution of 0.5 M H_3BO_3 and 1 M $CoSO_4$ at -0.75 V versus Ag/AgCl for 10 min, followed by an anodic oxidation at +0.2 V versus Ag/AgCl.

3.2.3 Preparation of MoS_2/CF electrocatalyst.

Typically, 0.27 g of Na_2MoO_4 and 1.5 g of thiourea (without NH_4F) were added to 35 mL of distilled water under vigorous stirring for 1 h to form a homogeneous solution. Then, the following steps are the same as for N-MoS_2/CF electrocatalyst synthesis.

3.2.4 Preparation of CoO/CF electrocatalyst.

CoO was electrochemically deposited on the N-MoS_2/CF substrate using an aqueous solution of 0.5 M H_3BO_3 and 1 M $CoSO_4$ at -0.75 V *vs.* Ag/AgCl for 10 min [32]. Subsequently, CoO/N-MoS_2/CF electrocatalyst was oxidized by applying an anodic potential of 0.2 V *vs.* Ag/AgCl for 2 min.

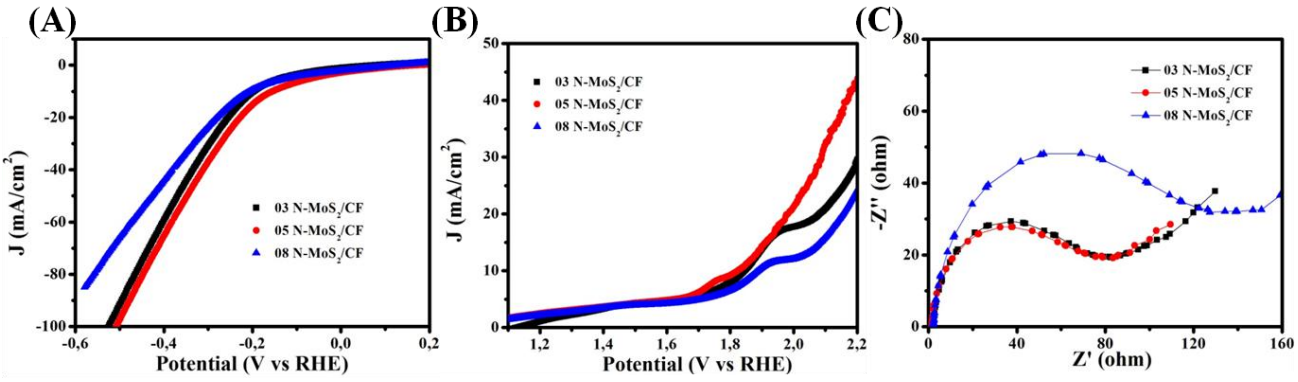

Figure 1. (A) HER polarization curves of different dosage of NH_4F: 0.3g (black), 0.5 g (red) and 0.8 g (blue). (B) OER polarization curves 0.3 g (black), 0.5 g (red) and 0.8 g (blue). (C) Nyquist plots of the prepared electrocatalysts recorded over 100 kHz to 0.01 Hz frequency range.

3.2.5 Electrochemical measurements

Electrochemical measurements were performed with a ModuLab-MTS electrochemical test station (Solartron, France) in a standard three-electrode system using the prepared catalysts as the working electrode, Pt plate as the counter electrode and Ag/AgCl (3.5 M KCl) electrode as the reference electrode. Linear sweep voltammetry (LSV) measurements were performed in 1.0 M KOH at the scan rate of 50 mV s^{-1}.

A two-electrode alkaline water electrolyzer was constructed using CoO/N-MoS_2/CF as both cathode and anode for full water splitting in 1.0 M KOH aqueous solution.

3.3 Results and discussion

3.3.1 Illustration of the CoO/N-MoS_2/CF fabrication process

The fabrication process of CoO/N-MoS_2/CF is schematically illustrated in **Figure 2**. Prior to MoS_2 deposition, the CF was activated through thermal annealing at 400 °C, followed by chemical treatment in boiling HNO_3 aqueous solution. This activation step is necessary not only to remove organic impurities on the CF surface, but also to switch the wetting properties from hydrophobic to hydrophilic through the generation of oxygen containing functional groups. Hydrothermal process was used for coating N-doped MoS_2 on the CF support, followed by electrochemical deposition of CoO from a cobalt sulfate ($CoSO_4$) precursor under acidic conditions.

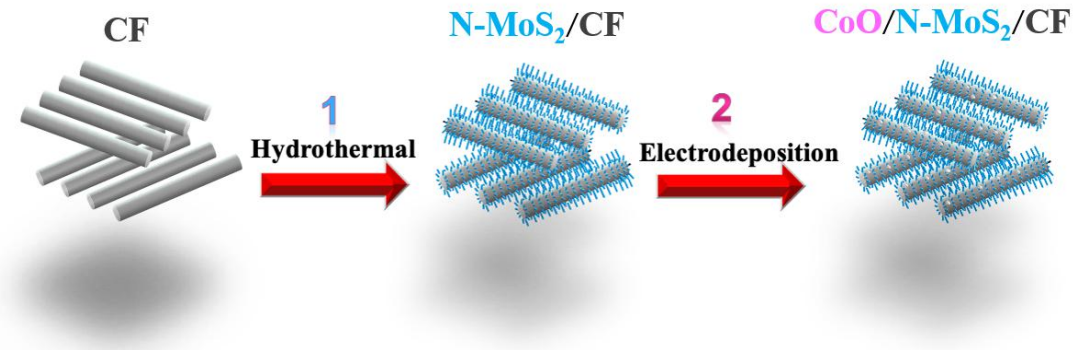

Figure 2. Illustration of the CoO/N-MoS_2/CF fabrication process.

3.3.2 Surface analysis of CoO/N-MoS_2/CF

Figure 3A depicts an SEM micrograph of the carbon fiber (CF) at high magnification, revealing a dense and smooth carbon network without apparent defects or particles on its surface. MoS_2 coating on CF is clearly evidenced by the presence of a dense sheet-like layer (**Figure 3B**). After nitrogen doping and Co electrodeposition, the SEM images in **Figure 3C** and **3D** reveal that N-MoS_2/CF and CoO/N-MoS_2/CF have similar morphology, consisting of intercrossed MoS_2 nanoflakes covering homogeneously the CF support. The chemical composition of CoO/N-MoS_2/CF was assessed by energy-dispersive spectroscopy (EDS) elemental mapping, **Figure 4**. The EDS spectrum comprises peaks ascribed to C, Mo, S, and Co, while the EDS elemental mapping shows homogeneous distribution of these elements in the material. It is worth to note that nitrogen was not detected using this technique because of its low content (see XPS analysis below).

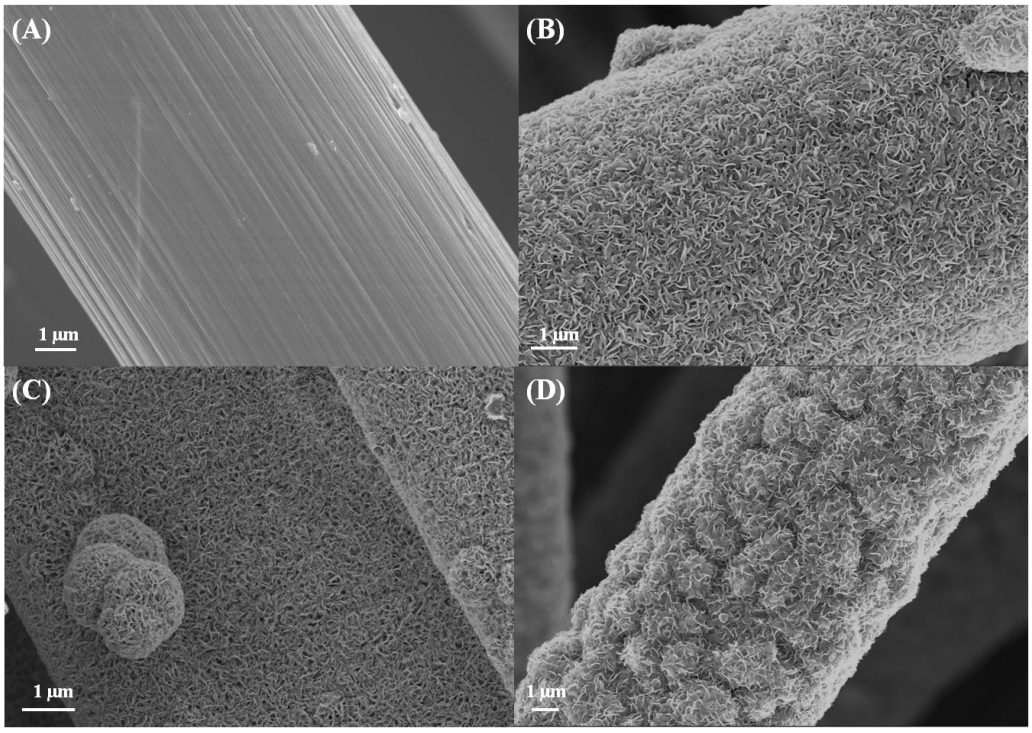

Figure 3: High magnification SEM micrographs of (A) CF, (B) MoS_2/CF, (C) N-MoS_2/CF (C) and (D) CoO/N-MoS_2 /CF.

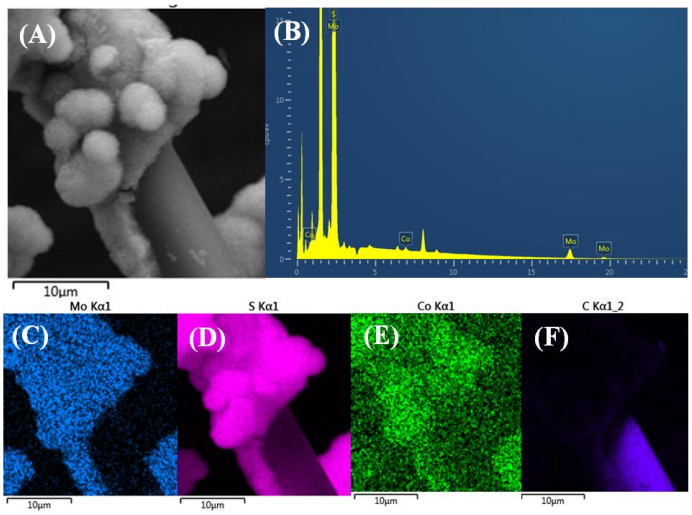

Figure 4. (A) SEM of CoO/N-MoS_2/CF. (B) EDX spectrum recorded from (A). (C) EDS mapping of Mo (C), (D) S, (E) Co, and (F) C.

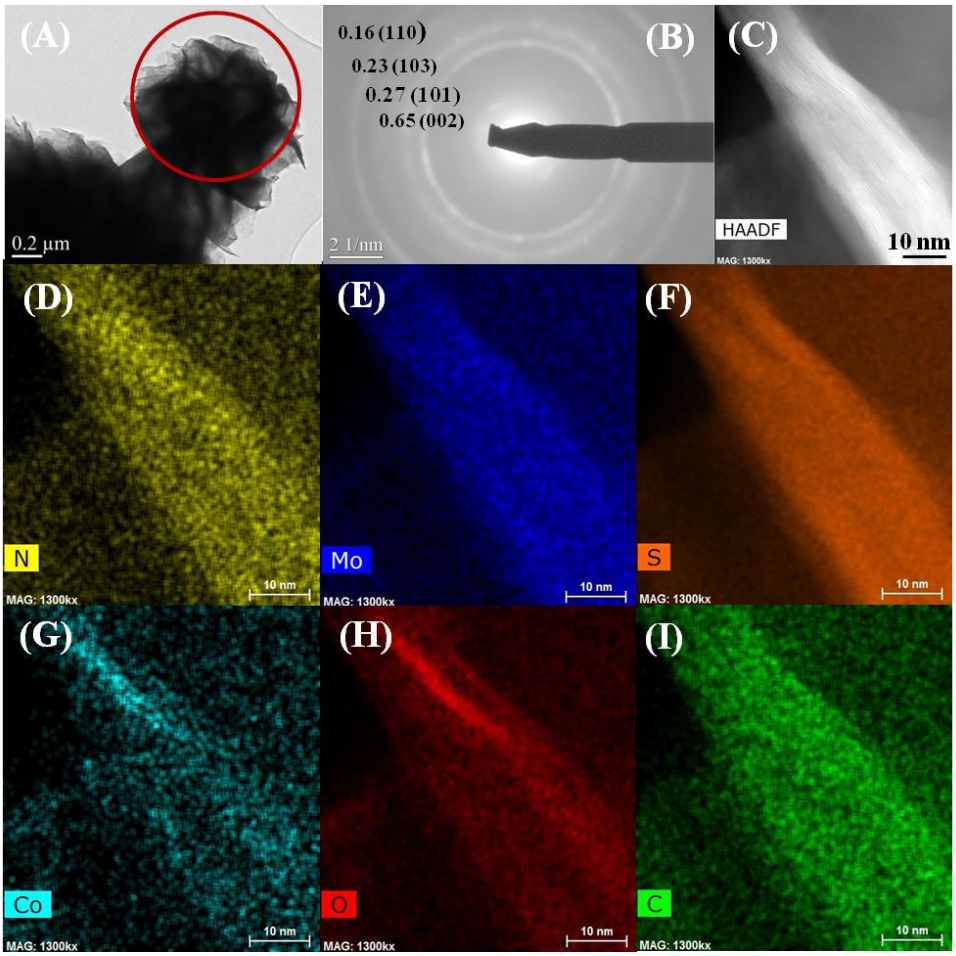

Figure 5. (A) TEM image of CoO/N-MoS_2/CF. (B) SAED image taken in (A). (C) HRTEM image of CoO/N-MoS_2/CF. (D-I) EDX elemental mapping images of a CoO/N-MoS_2/CF, indicating the homogeneous distribution of N, Mo, S, Co, O and C.

Transmission electron microscopy (TEM, **Figure 5A**) images further showed a large number of thin rogues-shaped MoS_2 nanosheets. The interlayer spacing of 0.65, 0.27, 0.23 and 0.16 nm between the stripes of MoS_2 can be observed from the SAED pattern (**Figure 5B**), which can be indexed respectively to the (002), (101), (103) and (110) planes of MoS_2. The HRTEM images of **Figure 5C** confirm that the surface of MoS_2 was covered with no particles. Moreover, the corresponding EDX mapping analyses indicate the homogeneous distribution of N, Mo, S, Co, O and C (**Figure D-I**). The absence of diffraction peaks from CoO suggests its amorphous nature.

3.3.3 Structural analysis of CoO/N-MoS_2/CF

Figure 6A depicts the XRD patterns of the CF, N-MoS_2/CF and CoO/N-MoS_2/CF electrocatalysts. The XRD pattern of the CF comprises a prominent diffraction peak at 26.1° and a small contribution at 54.2° due to the (002) and (004) planes of carbon, respectively (PDF card 81-2220). The XRD of N-MoS_2/CF and CoO/N-MoS_2/CF electrocatalysts display diffraction peaks at 14.4°, 33.6°, 39.6° and 58.6°, which can be indexed respectively to the (002), (101), (103) and (110) planes of MoS_2 (JCPDS No. 73-1508) along with diffraction peaks at 2θ of 26.1° and 54.2° ascribed to the (002) and (004) planes of carbon, respectively (PDF card 81-2220). Although the diffraction peaks of both CF and MoS_2 can be easily distinguished on the XRD pattern of CoO/N-MoS_2/CF, no obvious XRD signature was observed for CoO, suggesting that CoO is amorphous in nature or its thickness is very low to be detected under our experimental conditions.

The bonding characteristics of the prepared electrocatalysts are in addition identified by Raman spectroscopy. **Figure 6B** displays the Raman spectra of N-MoS_2/CF and CoO/N-MoS_2/CF. For both samples, the characteristic peaks of MoS_2 with E_{2g}^1 (~378 cm^{-1}) and A_{1g} (~401 cm^{-1}) modes are observed, indicating the existence of MoS_2 nanolayers. The peak at 280 cm^{-1} is identified as E_{1g} mode associated with the octahedral coordination of Mo atoms in

the 1T phase MoS_2 [33]. The two scattering bands located at around 1340 and 1580 cm^{-1} are ascribed to the disorder-induced D band and the tangential stretching G band mode, respectively, characteristic of graphenic materials. Obviously, the D/G intensity ratio (I_D/I_G) of the prepared CoO/N-MoS_2/CF sample (0.61) is lower than that of N-MoS_2/CF (0.87), suggesting the reduction of the defects in the CoO/N-MoS_2/CF electrode material.

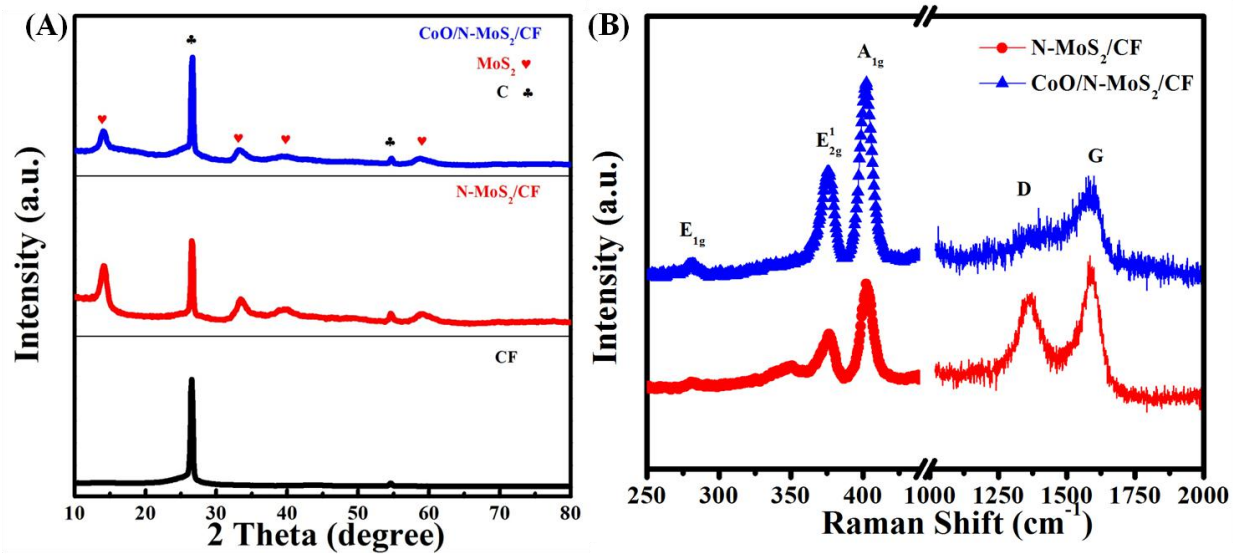

Figure 6: (A) XRD patterns of the CF, N-MoS_2/CF and CoO/N-MoS_2/CF electrocatalysts. (B) Raman spectra of N-MoS_2/CF and CoO/N-MoS_2/CF.

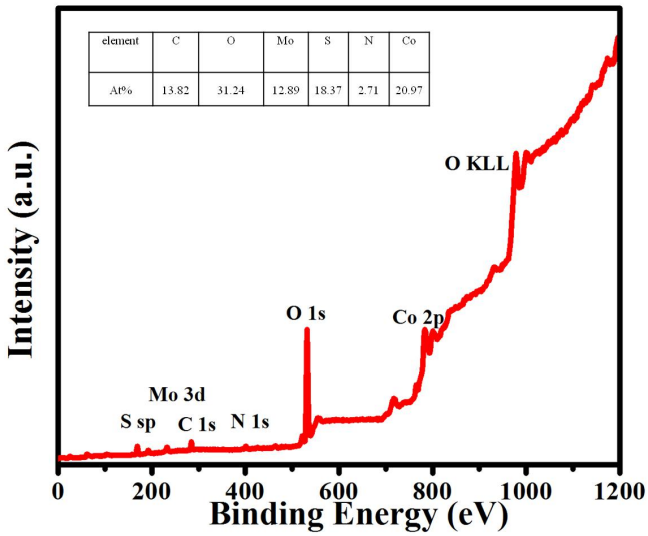

Figure 7. XPS survey spectrum of CoO/N-MoS_2/CF.

The chemical analysis and oxidation state of the different elements on the hierarchical surface of CoO/N-MoS_2/CF were assessed using X-ray photoelectron spectroscopy (XPS). The XPS survey spectrum of Co/N-MoS_2/CF comprises peaks due to C, O, Mo, S, N and Co with atomic concentrations of 13.82, 31.24, 12.89, 18.37, 2.71 and 20.97 at%, respectively (**Figure 7**). The high concentration of oxygen results most likely from carbon fiber oxidation during its annealing/activation steps. Also, it is worth to notice the deviation of Mo/S ratio (0.7) from 0.5 expected for a stoichiometric MoS_2 product. This is partially due to nitrogen doping of MoS_2.

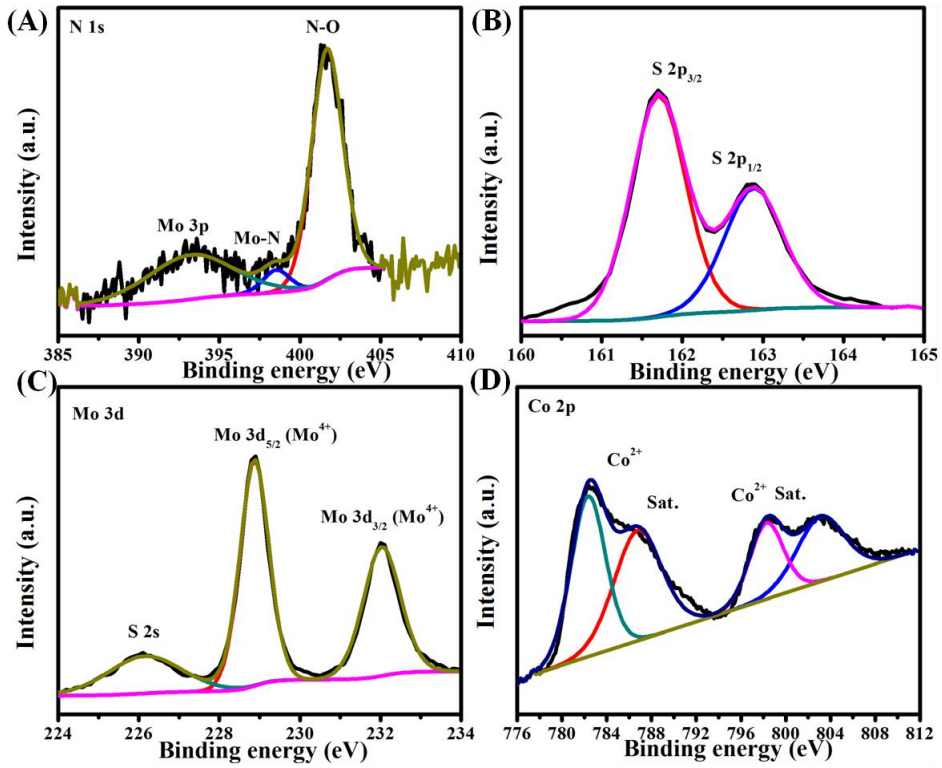

Figure 8: XPS analysis of the CoO/N-MoS_2/CF. High-resolution XPS spectra of (A) N_{1s}, (B) S_{2p}, (C) Mo_{3d}, (D) Co_{2p}.

Figure 8A depicts the core level XPS spectra of the $Mo_{3p3/2}$ and N_{1s}. The band at 394.5 eV is attributed to $Mo_{3p3/2}$, while the overlapped peak signal located at 398.9 eV originates from

N-Mo bonds. The prominent N_{1s} peak at 401.5 eV can be ascribed to graphitic nitrogen [34] and N-O bonds [24]. Indeed, under the hydrothermal conditions, it is not excluded that the carbon fiber is also partially doped with nitrogen. N-O most likely arises from nitrogen oxidation under hydrothermal conditions. The S_{2p} high resolution XPS spectrum comprises two dominant doublet peaks at 161.2 and 162.4 eV, corresponding to the $S_{2p3/2}$ and $S_{2p1/2}$, respectively (**Figure 8B**). The Mo_{3d} high resolution spectrum (**Figure 8C**) can be fitted with three components centered at 226.2, 229.2 and 232.4 eV due to S_{2s}, $Mo_{3d5/2}$ and $Mo_{3d3/2}$ of MoS_2, respectively [26]. The core level XPS spectrum of Co_{2p} is displayed in **Figure 8D**. The spectrum contains two prominent peaks at 781.1 and 797.3 eV due to $Co_{2p1/2}$ and $Co_{2p3/2}$, respectively and two shake-up satellite peaks (abbreviated as "Sat."), indicating that Co exists in +2 oxidation state in CoO [35].

3.3.4 CoO/N-MoS_2/CF activity for HER and OER

The electrochemical behavior of the as-prepared electrocatalysts for HER was assessed in 1.0 M KOH aqueous solution using a three-electrode system. To reflect the sole contribution from the electrocatalyst, the polarization curves have been I-R corrected to avoid interference caused by ohmic losses from wiring, substrate and electrolyte. Interestingly, intercalation of CoO nanomaterial into N-MoS_2/CF improved significantly the HER activity of MoS_2 (i.e., N-MoS_2/CF *vs.* CoO/N-MoS_2/CF). **Figure 9A** depicts the linear sweep voltammograms (LSV) recorded in a N_2-purged 1.0 M KOH aqueous solution of the different electrocatalysts, namely CF, CoO/CF, MoS_2/CF, N-MoS_2/CF, CoO/N-MoS_2/CF and Pt plate. The CoO/N-MoS_2/CF and Pt electrocatalysts achieved a current density of 10 mA cm^{-2} respectively at a low overpotential of 78 and 52 mV for HER, largely improved compared to CF (550 mV), CoO/CF (310 mV), MoS_2/CF (220 mV) and N-MoS_2/CF (130 mV), suggesting that the CoO/N-MoS_2/CF electrode has superior catalytic activity. The comparison reveals that CoO hybridization with N-MoS_2 is the key element in the improvement of the HER activity.

The Tafel slope reflects the intrinsic properties of electrocatalyst materials [3], with smaller Tafel slope values indicate faster kinetics for efficient HER. From the data in **Figure 9B**, CoO/N-MoS_2/CF electrode displays a Tafel slope of 71 mV dec^{-1}. This value is somehow larger than 40 mV dec^{-1}, the theoretical value at which the Volmer-Heyrovsky reaction pathway takes place, where hydrogen desorption is the rate-limiting step. Additionally, the Tafel slopes of N-MoS_2/CF, MoS_2/CF, and CoO/CF are also determined from the LSV curves for comparison. Higher values of 93, 112, to 150 mV dec^{-1} are calculated for N-MoS_2/CF, MoS_2/CF and CoO/CF, respectively. These values are close to 120 mV dec^{-1}, suggesting that the HER proceeds *via* a primary discharge step. The lower Tafel slope of CoO/N-MoS_2/CF indicates a better HER kinetics.

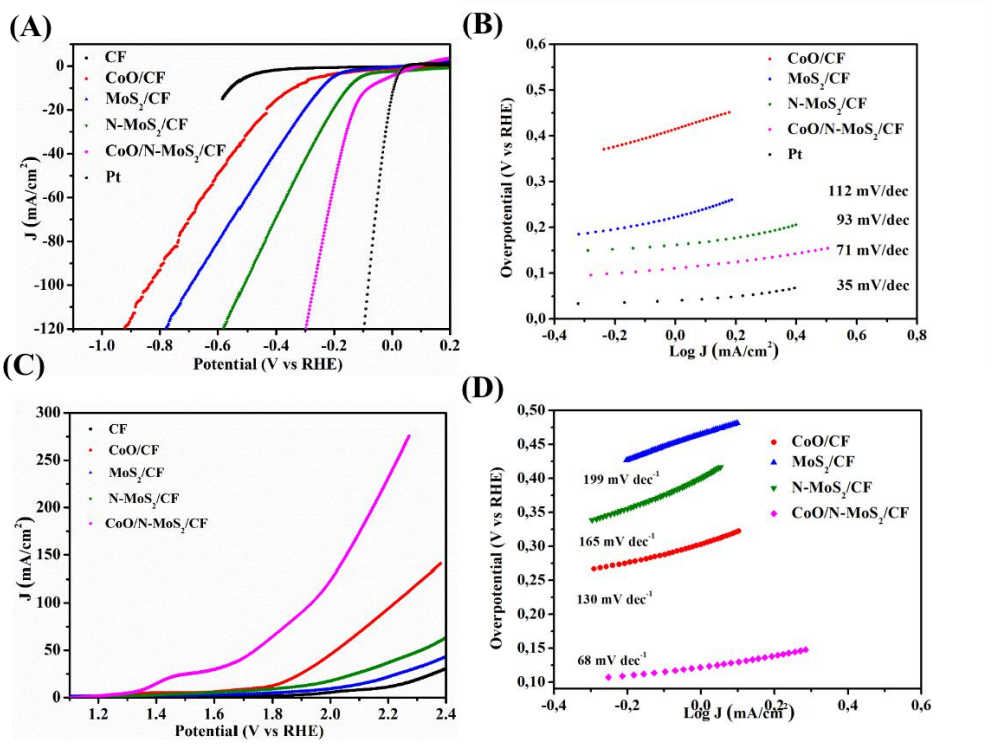

Figure 9: (A) HER polarization curves of CF, CoO/CF, MoS_2/CF, N-MoS_2/CF, CoO/N-MoS_2/CF and Pt plate electrocatalysts, scan rate = 50 mV s^{-1}. (B) The corresponding Tafel plots determined from LSV curves in (A). (C) OER polarization curves of CF, CoO/CF, MoS_2/CF, N-MoS_2/CF and CoO/N-MoS_2/CF. (D) The corresponding Tafel plots calculated from LSV curves in (C).

Furthermore, the electrocatalytic performance of CoO/N-MoS_2/CF was assessed for oxygen evolution reaction (OER) in 1.0 M KOH aqueous solution in a three-electrode system. **Figure 9C** displays the LSV curves of CoO/N-MoS_2/CF, N-MoS_2/CF, MoS_2/CF, CoO/CF and CF at 50 mV s^{-1}. In comparison with MoS_2/CF and N-MoS_2/CF, enhanced OER activity was observed for CoO/N-MoS_2/NF, confirming the low OER activity of MoS_2 [36]. MoS_2/CF and N-MoS_2/CF displayed an overpotential of 820 mV and 650 mV at 10 mA cm^{-2}, respectively. In contrast, CoO/N-MoS_2/CF revealed remarkably improved electrocatalytic activity with an overpotential of 138 mV at 10 mA cm^{-2}, which outperforms that of CF (980 mV) and CoO/CF (389 mV).

The Tafel slope value (**Figure 9D**) of CoO/N-MoS_2/CF is around 68 mV dec^{-1}, lower than that of MoS_2/CF (199 mV dec^{-1}), N-MoS_2/CF (165 mV dec^{-1}) and CoO/CF (130 mV dec^{-1}). Its onset potential (η_{onset}) is 100 mV, outperforming N-MoS_2/CF (410 mV), MoS_2/CF (520 mV) and CoO/CF (330 mV). The data reveals the kinetic merit of the CoO/N-MoS_2/CF for water oxidation, which is further attested by the Nyquist plots, revealing that the CoO/N-MoS_2/CF has enhanced electron transfer ability compared to N-MoS_2/CF, MoS_2/CF, CoO/CF and CF samples.

The kinetics of the developed electrocatalysts under HER were assessed by electrochemical impedance spectroscopy (EIS) measurements (**Figure 10A**). The complex-plane impedance plots of studied catalysts display two-time constants in the form of two depressed semicircles, and appear as two separated humps in the corresponding Bode plots (**Figure 11**), related to a resistance-capacitance (RC) network. The RC network comprises the charge transfer resistance (R_{ct}) of the HER and the corresponding double layer capacitance (C_{dl}) at the catalyst/electrolyte interface [37]. The first semicircle due to charge-transfer resistance exhibits a small diameter R_1 and occurs at high frequencies. The diameter R_2 of the

second semi-circle is large, covering a wide range of frequency values (medium-to-low frequency domains).

This impedance response is successfully modelled by the equivalent circuit presented in the inset of **Figure 10A**, with the overall impedance being described by a parallel combination of resistance and capacitance of two charge-transfer processes. The total charge-transfer resistance ($R_{ct} = R_1 + R_2$) describes the kinetics of the HER [38]. From the Nyquist plots, we can deduce that the diameters of the semicircles follow the trend: R_{ct} of CoO/N-MoS_2/CF (3.5 ohm·cm^{-2}) < R_{ct} of CoO/CF (30 ohm·cm^{-2}) < R_{ct} of N-MoS_2/CF (140 ohm·cm^{-2}) < R_{ct} of MoS_2/CF (225 ohm·cm^{-2}). The small charge transfer impedance reflects fast electron transfer during the HER, indicating high catalytic activity [10]. Note that the better electron transfer ability of CoO/N-MoS_2/CF should also contribute to its enhanced HER and OER catalytic activity.

As the stability is one of the key factors in determining the practicability of electrocatalysts, the CoO/N-MoS_2/CF catalyst long-term stability was probed by potential-time plots in an alkaline environment. **Figure 10B** depicts the chronopotentiometric curves of the CoO/N-MoS_2/CF catalyst recorded in 1.0 M KOH aqueous solution at J = -10 mA cm^{-2} (red line) and J = +10 mA cm^{-2} (black line). The V-t measurements indicated an almost steady potential without any significant decay during 50 h of continuous HER and OER, revealing the high stability of the CoO/N-MoS_2/CF electrode for HER and OER.

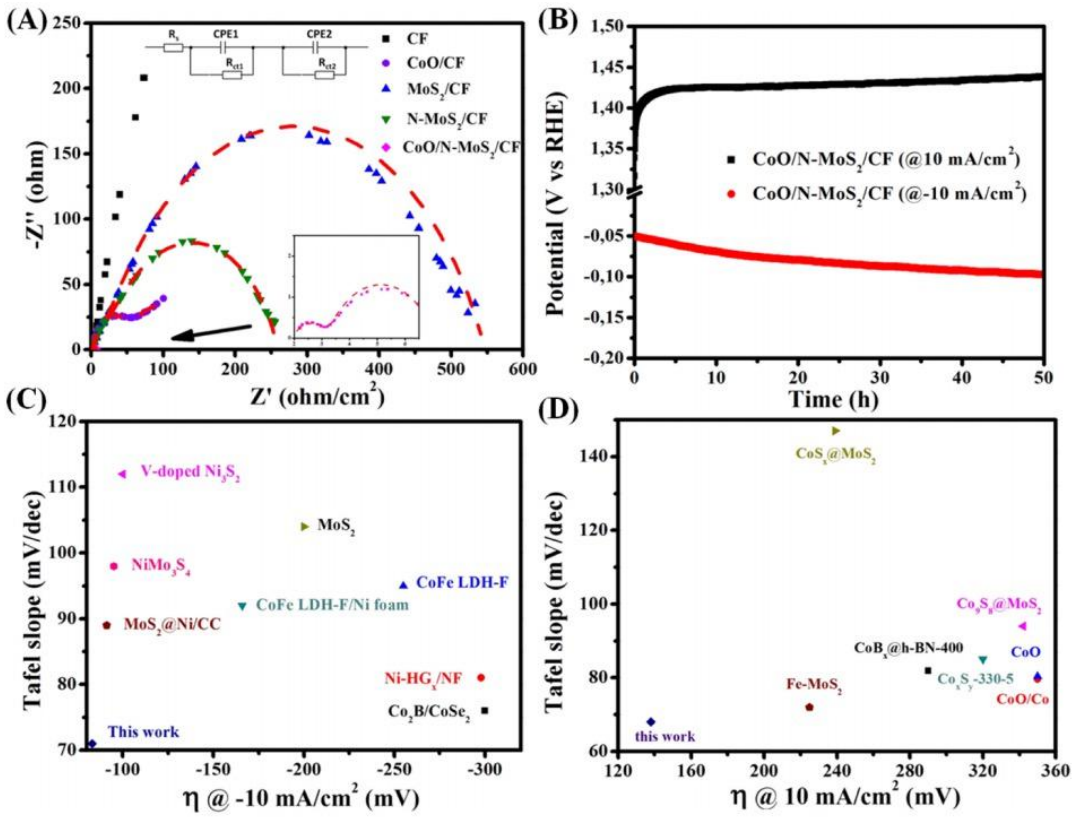

Figure 10: (A) Nyquist plots of the prepared electrocatalysts recorded over 100 kHz to 0.01 Hz frequency range. (B) HER and OER stability tests of CoO/N-MoS_2/CF catalyst at J= -10 mA cm^{-2} and J = +10 mA cm^{-2} in 1 M KOH solution, respectively. (C) Comparison of the overpotential at -10 mA cm^{-2} and Tafel slope values of recent reports on Mo- and Co-based electrocatalysts. (D) Comparison of the overpotential at +10 mA cm^{-2} and Tafel slope values of recent reports on Mo- and Co-based electrocatalysts.

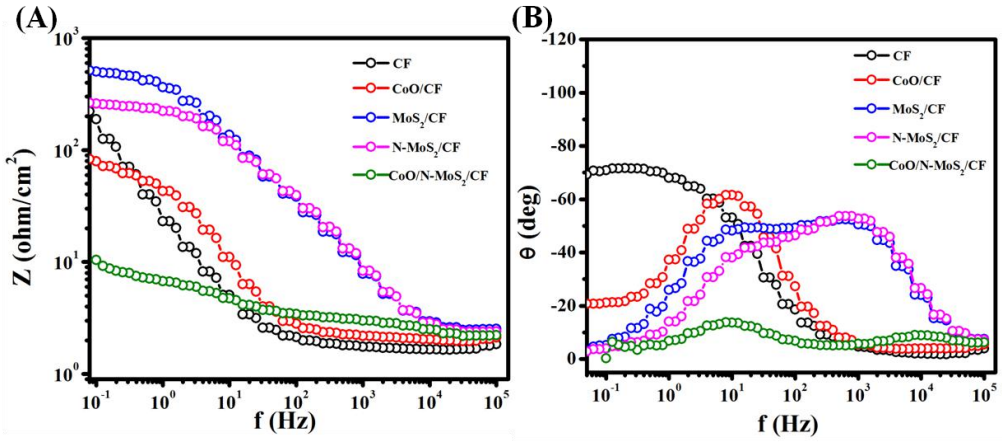

Figure 11. Bode (A) impedance modulus |Z| and (B) phase angle θ.

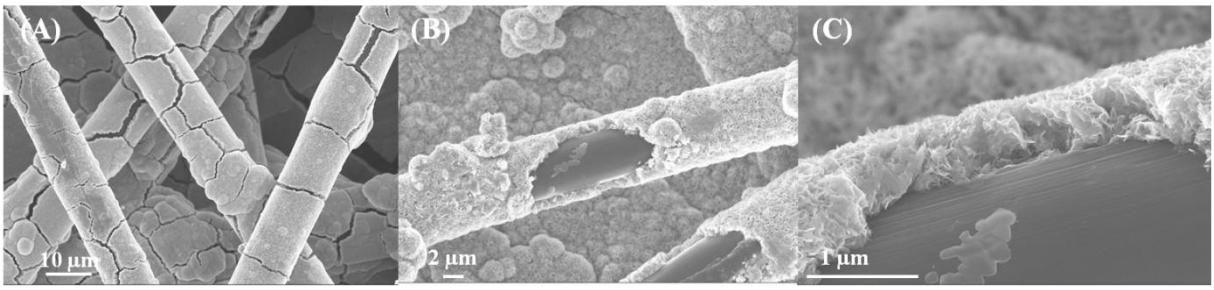

Figure 12. The SEM image of CoO/N-MoS_2/CF after HER and OER stability tests. (A) after 30000s OER and HER stability test. (B) After 50 h OER and HER stability test. (C) SEM micrograph of (B) at higher magnification.

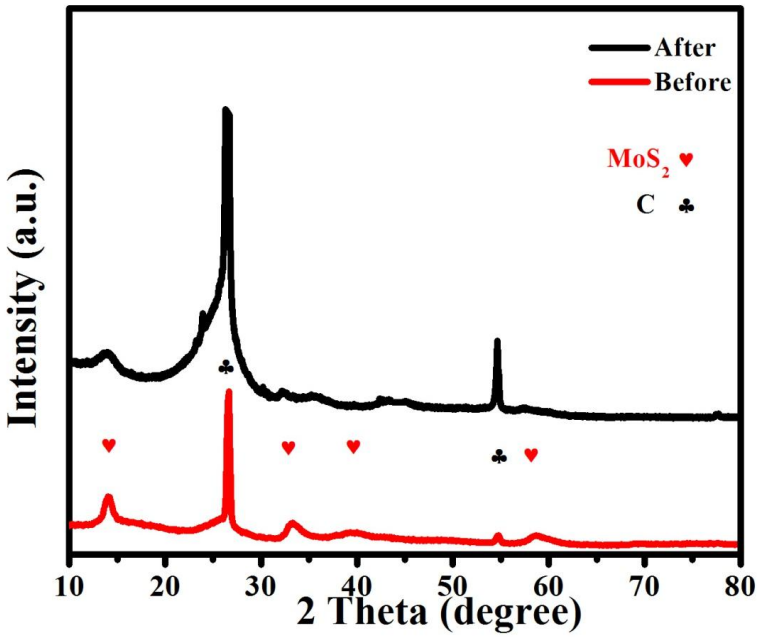

Figure 13. XRD patterns of the as-prepared CoO/N-MoS_2/CF electrocatalyst before (red) and after (black) HER and OER stability tests.

SEM (**Figure 12**) imaging and XRD (**Figure 13**) analysis were performed to follow the changes that occurred after the HER and OER stability tests. The SEM image of CoO/N-MoS_2/CF exhibits cracks within the CoO/N-MoS_2 layer that were absent in the SEM image of the as-prepared electrocatalyst. The presence of cracks suggests partial loss of CoO/N-MoS_2

layer and/or morphological changes due to stress encountered during the stability tests. The result is corroborated by the slight decrease of the MoS_2 diffraction peaks intensity in the XRD pattern and increase of the CF related peaks (**Figure 13**). All of the diffraction peaks of N-MoS_2 are in good agreement with the standard card data of hexagonal MoS_2.

Figure 10 C, D summarizes the HER [39-44] and OER [45-50] kinetic data of recent Mo- and Co-based electrodes in alkaline solutions. It is important to notice that most of these electrocatalysts consist of nanostructured films or foams with large surface areas and high loading amounts. From these comparison studies, it is obvious that CoO/N-MoS_2/CF electrode represents one of the most active electrocatalysts with Tafel slope values of 71 and 68 mV dec^{-1} for HER and OER, respectively (for more details see **Tables 1** and **2**). The low Tafel slope values indicate that, upon increasing the overpotential, both OER and HER rates of CoO/N-MoS_2/CF will increase rapidly, which is beneficial for practical applications.

Table 1. HER properties of reported MoS_2-based electrocatalysts.

Catalyst	Onsetpotential (mV vs. RHE)	V at J = 10 mA/cm^2 (mV)	Tafel slope (mv/dec)	Reference
MoS_2@Ni/CC	30	91	89	[41]
Co_9S_8@MoS_2	/	143	117	[47]
MoS_2/$MoSe_2$	180	235	96	[51]
MoS_2@CoO	/	173	129.9	[52]
$Ni(OH)_2$/MoS_2	/	227	105	[53]
CoMoOS	65	130	86	[54]
MoS_2-WS_2	/	129	72	[55]
CoO/N-MoS_2/CF	**30**	**78**	**71**	**this work**

Table 2. OER properties of reported MoS_2-based electrocatalysts.

Catalyst	Onsetpotential (mV vs. RHE)	η at J = 10 mA cm^{-2} (mV)	Tafel slope (mV dec^{-1})	Reference
Co_9S_8@MoS_2	/	342	79	[47]
CoS_x@MoS_2	/	347	147	[46]
Fe-MoS_2	/	225	72	[48]
CoO/Co	/	350	79.6	[50]
MoS_2@CoO	270	325	83	[52]
CoO/N-MoS_2/CF	**100**	**470 (50 mA cm^{-2})**	**68**	**this work**

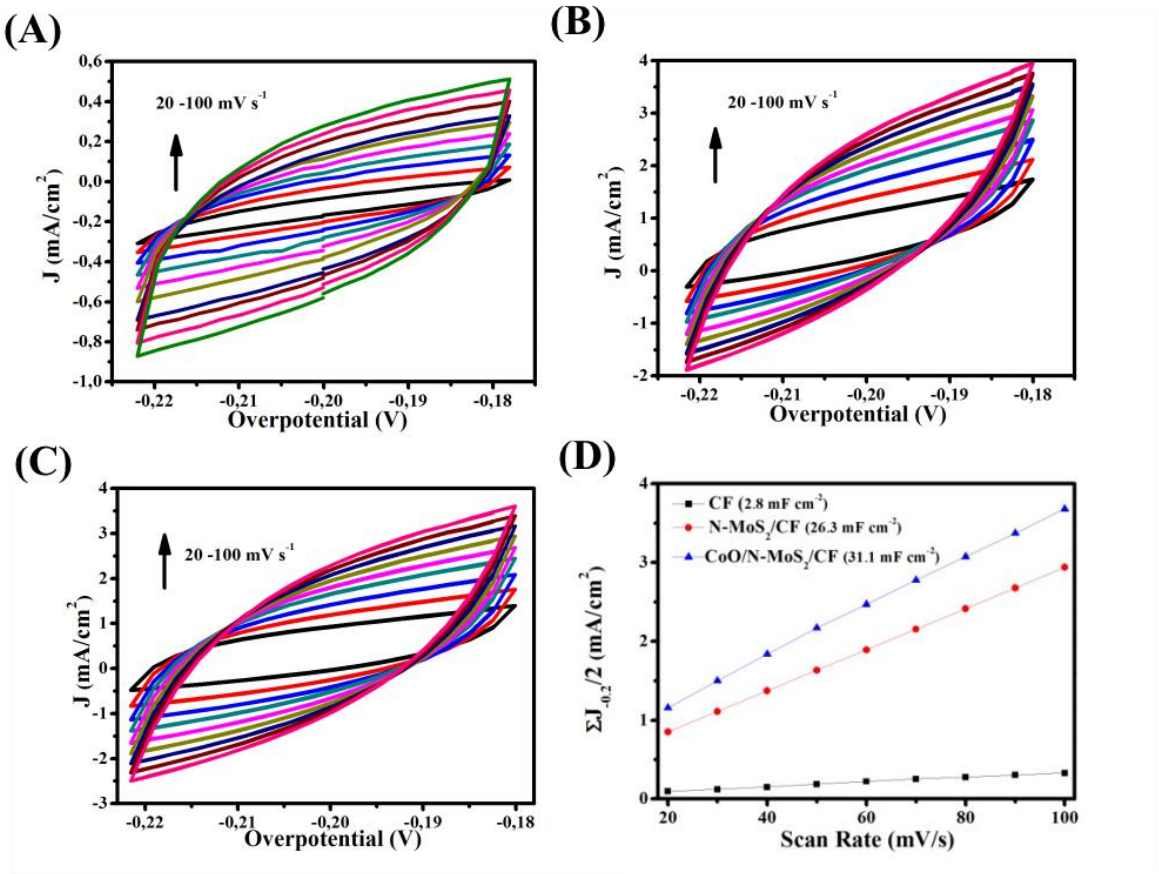

Figure 14: Cyclic voltammograms of (A) CF, (B) N-MoS_2/CF, (C) CoO/N-MoS_2/CF in the -0.18 ~ -0.22 V *vs.* Ag/AgCl potential range. (D) Double-layer charging currents of CF, N-MoS_2/CF and CoO/N-MoS_2/CF recorded at -0.20 V at various scan rates.

To advance our understanding on the enhanced HER and OER electrocatalytic activity of CoO/N-MoS_2/CF compared to N-MoS_2/CF, the electrochemical active surface areas (ECSAs) were calculated from the electrical double layer capacitance (C_{dl}) [51].

To evaluate the C_{dl}, cyclic voltammograms were acquired in a non-Faradaic potential window of the voltammograms (-0.18 ~ -0.22 V *vs.* Ag/AgCl) at various scan rates (**Figure 14A-C**). It is generally accepted that the ECSA is proportional to its C_{dl} value for electrocatalysts of similar composition. The C_{dl} values were calculated from the slope of the straight line (linear part) of the current density *vs.* scan rate curves. The good electrochemical activity of the CoO/N-MoS_2/CF electrode was revealed by a larger double layer capacitance value of 16 mF cm^{-2}, as compared to N-MoS_2/CF (13 mF cm^{-2}) and CF (1 mF cm^{-2}) (**Figure 14D**).

3.3.5 Calculation of roughness factor and active site density

The C_{dl} values are used to calculate the roughness factor (R_f), one of the most important parameters employed to account for the high catalytic performance of electrocatalysts [52, 53]. In this respect, the method of Jaramillo et al.[52, 53] is applied here for the calculation of R_f of the investigated catalysts. Based on this method, the value of R_f is calculated from the ratio of $C_{measured}$ to $C_{calculated}$ ($R_f = C_{measured} / C_{calculated}$); both measured in mF cm^{-2}. $C_{measured}$ denotes the capacitance value recorded from CV measurements (**Figure 14**), while $C_{calculated}$ represents the capacitance value obtained from flat surfaces (20-60 μF/cm^2) [52]. In these calculations, an average value of 40 μF cm^{-2} (or 0.04 mF cm^{-2}) is considered for $C_{calculated}$. Based on these values, R_f values of 25, 325, and 400 were estimated for CF, N-MoS_2/CF, and CoO/N-MoS_2/CF, respectively. The high R_f value of the CoO/N-MoS_2/CF catalyst highlights its outstanding catalytic activity as compared to N-MoS_2/CF.

The number of catalytic surface sites, designated here as $N_{catalyst}$, for the tested catalysts was estimated from the product of R_f and catalyst surface sites per cm^2 geometric area [52,

53]. Considering 1.164×10^{15} MoS_2/cm^2 as the number of surface sites per cm^2 geometric area for flat MoS_2 [54], the value of $N_{catalyst}$ for N-MoS_2/CF and CoO/N-MoS_2/CF catalysts was estimated to be 7.65×10^{17} and 9.05×10^{17}, respectively, referring to a large number of active sites.

3.3.6 Calculation of turnover frequency

The turnover frequency (TOF) per site was determined by dividing the total H_2 turnover per cm^2 geometric area $(TOF)_{hydrogen}$ by the catalyst surface sites per cm^2 geometric area, $N_{catalyst}$ [55]. A value of 3.12×10^{15} H_2 $s^{-1}cm^{-2}$ $(mA\ cm^{-2})^{-1}$ was adopted for $(TOF)_{hydrogen}$ [55]. So the TOF per site for N-MoS_2/CF and CoO/N-MoS_2/CF catalysts at a cathodic potential of -200 mV *vs.* RHE is calculated using the expression given below, where cathodic current densities of j_c = 20 and 54 mA cm^{-2} were generated at that potential for N-MoS_2/CF, and CoO/N-MoS_2/CF catalysts, respectively.

TOF per site = $\{(j_c)\ (TOF)_{hydrogen}\}$ / $N_{catalyst}$

Based on this equation, TOF values of 0.082 and 0.19 H_2/s per surface site were estimated for N-MoS_2/CF and CoO/N-MoS_2/CF catalysts, respectively. These results confirm the promising catalytic activity of the CoO/N-MoS_2/CF catalyst, as it exhibits a faster TOF value compared to N-MoS_2/CF catalyst.

3.3.7 Full water splitting

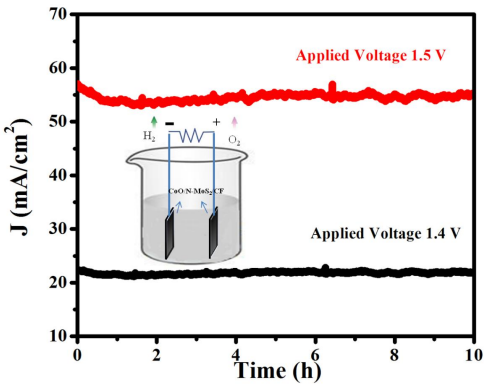

Figure 15: Chronoamperometric measurements of overall water splitting in 1.0 M KOH aqueous solution at an applied potential of 1.4 or 1.5 V across the two electrodes.

Inspired by the excellent OER/HER catalytic performances of CoO/N-MoS_2/CF, we investigated the potential of CoO/N-MoS_2/CF as cathode and anode for full water splitting in a two-electrode alkaline water electrolyzer system. **Figure 15** exhibits the chronoamperometry (j ~ t) curves recorded in 1.0 M KOH. The CoO/N-MoS_2/CF was able to deliver stable current densities of 21 and 53 mA cm^{-2} at constant applied potentials of 1.4 and 1.5 V, respectively for 10 h, attesting of its good performance.

A comparison with literature data reveals the good performance of CoO/N-MoS_2/CF for full water splitting (**Table 3**).

Table 3. Full water splitting properties of reported Mo- and Co-based electrocatalysts.

Catalyst	Solution	Potential (V)	Current density (mA cm^{-2})	Reference
MoP/CC + CoP/CC	1.0 M KOH	1.6	40	[56]
GDs/$Co_{0.8}Ni_{0.2}P$	1.0 M KOH	1.54	10	[57]
CoP/Co_9S_8	1.0 M KOH	1.6	10	[58]
NiMoN	1.0 M KOH	1.507	10	[59]
CoO_x-CoSe	1.0 M KOH	1.66	20	[60]
Ni - Fe - Mo NTs	1.0 M KOH	1.513	10	[61]
$Co_5Mo_{1.0}P$ NSs@NF	1.0 M KOH	1.68	10	[62]
CoO/N-MoS_2/CF	**1.0 M KOH**	**1.4**	**21**	**this work**

3.4 Conclusion

In summary, CoO loaded on N-MoS_2 nanosheets supported on 3D conductive carbon fiber (CoO/N-MoS_2/CF) electrocatalyst was prepared using sequential hydrothermal and electrochemical processes. The catalytic activity of the developed CoO/N-MoS_2/CF electrode

was assessed for hydrogen evolution reaction (HER) and oxygen evolution reaction (OER) in alkaline medium. Our results revealed the high performance of CoO/N-MoS_2/CF as an efficient and robust bifunctional electrocatalyst. The inclusion of CoO allowed to tune effectively the electronic structure as well as the electrochemical active surface area and catalytic kinetics of the CoO/N-MoS_2/CF catalyst. Remarkably, the optimized CoO/N-MoS_2/CF electrocatalyst delivered a current density of -10 mA cm^{-2} at very small overpotential values of 78 mV and 50 mA cm^{-2} at 458 mV, respectively for HER and OER. Chronoamperometry measurements in 1.0 M KOH aqueous solution established the high stability of the electrode. Furthermore, the robustness of the developed electrocatalyst was demonstrated in full water splitting configuration at an applied potential of 1.5 V. The results obtained in this study provide important aspects for the development of earth-abundant elements-based electrode materials as cost-effective, robust and efficient electrocatalysts for full water splitting applications.

3.5 References

[1] Anantharaj, S.; Ede, S. R.; Sakthikumar, K.; Karthick, K.; Mishra, S.; Kundu, S. Recent Trends and Perspectives in Electrochemical Water Splitting with an Emphasis on Sulfide, Selenide, and Phosphide Catalysts of Fe, Co, and Ni: A Review. ACS Catal. 2016, 6, 12, 8069-8097.

[2] Wang, J.; Yue, X.; Yang, Y.; Sirisomboonchai, S.; Wang, P.; Ma, X.; Abudula, A.; Guan, G. Earth-abundant transition-metal-based bifunctional catalysts for overall electrochemical water splitting: A review. J. Alloys Comp. 2020, 819, 153346.

[3] Roger, I.; Shipman, M. A.; Symes, M. D. Earth-abundant catalysts for electrochemical and photoelectrochemical water splitting. Nat Rev Chem 2017, 1, 0003.

[4] Liu, Z.; Qi, J.; Liu, M.; Zhang, S.; Fan, Q.; Liu, H.; Liu, K.; Zheng, H.; Yin, Y.; Gao, C. Aqueous Synthesis of Ultrathin Platinum/Non-Noble Metal Alloy Nanowires for Enhanced Hydrogen Evolution Activity. Angew. Chem. Int. Ed. 2018, 57, 11678-11682.

[5] Zhu, C.; Shi, Q.; Feng, S.; Du, D.; Lin, Y. Single-Atom Catalysts for Electrochemical Water Splitting. ACS Energy Lett. 2018, 3, 7, 1713-1721.

[6] Zhao, D.; Zhuang, Z.; Cao, X.; Zhang, C.; Peng, Q.; Chen, C.; Li, Y. Atomic site electrocatalysts for water splitting, oxygen reduction and selective oxidation. Chem. Soc. Rev. 2020, 49, 2215-2264.

[7] Mishra, I. K.; Zhou, H.; Sun, J.; Qin, F.; Dahal, K.; Bao, J.; Chen, S.; Ren, Z. Hierarchical CoP/Ni_5P_4/CoP microsheet arrays as a robust pH-universal electrocatalyst for efficient hydrogen generation. Energy Environ. Sci. 2018, 11, 2246-2252.

[8] Li, P.; Zhao, R.; Chen, H.; Wang, H.; Wei, P.; Huang, H.; Liu, Q.; Li, T.; Shi, X.; Zhang, Y.; Liu, M.; Sun, X., Recent Advances in the Development of Water Oxidation Electrocatalysts at Mild pH. Small 2019, 15, e1805103.

[9] Ito, Y.; Ohto, T.; Hojo, D.; Wakisaka, M.; Nagata, Y.; Chen, L.; Hu, K.; Izumi, M.; Fujita, J.-i.; Adschiri, T. Cooperation between holey graphene and NiMo alloy for hydrogen evolution in an acidic electrolyte. ACS Catal. 2018, 8, 3579-3586.

[10] Kuang, P.; Tong, T.; Fan, K.; Yu, J. In Situ Fabrication of Ni-Mo Bimetal Sulfide Hybrid as an Efficient Electrocatalyst for Hydrogen Evolution over a Wide pH Range. ACS Catal. 2017, 7, 6179-6187.

[11] Wang, L.; Wu, X.; Guo, S.; Han, M.; Zhou, Y.; Sun, Y.; Huang, H.; Liu, Y.; Kang, Z. Mesoporous nitrogen, sulfur co-doped carbon dots/CoS hybrid as an efficient electrocatalyst for hydrogen evolution. J. Mater. Chem. A 2017, 5, 2717-2723.

[12] Xiao, W.; Liu, P.; Zhang, J.; Song, W.; Feng, Y. P.; Gao, D.; Ding, J. Dual-Functional N Dopants in Edges and Basal Plane of MoS_2 Nanosheets Toward Efficient and Durable Hydrogen Evolution. Adv. Energy Mater. 2017, 7, 1602086.

[13] Liang, Y.; Liu, Q.; Asiri, A. M.; Sun, X.; Luo, Y., Self-Supported FeP Nanorod Arrays: A Cost-Effective 3D Hydrogen Evolution Cathode with High Catalytic Activity. ACS Catal. 2014, 4, 4065-4069.

[14] Liu, T.; Liu, D.; Qu, F.; Wang, D.; Zhang, L.; Ge, R.; Hao, S.; Ma, Y.; Du, G.; Asiri, A. M.; Chen, L.; Sun, X. Enhanced Electrocatalysis for Energy-Efficient Hydrogen Production over CoP Catalyst with Nonelectroactive Zn as a Promoter. Adv. Energy Mater. 2017, 7, 1700020.

[15] Menezes, P. W.; Panda, C.; Loos, S.; Bunschei-Bruns, F.; Walter, C.; Schwarze, M.; Deng, X.; Dau, H.; Driess, M. A structurally versatile nickel phosphite acting as a robust bifunctional electrocatalyst for overall water splitting. Energy Environ. Sci. 2018, 11, 1287-1298.

[16] Jia, J.; Xiong, T.; Zhao, L.; Wang, F.; Liu, H.; Hu, R.; Zhou, J.; Zhou, W.; Chen, S. Ultrathin N-Doped Mo_2C Nanosheets with Exposed Active Sites as Efficient Electrocatalyst for Hydrogen Evolution Reactions. ACS Nano 2017, 11, 12509-12518.

[17] Lin, H.; Shi, Z.; He, S.; Yu, X.; Wang, S.; Gao, Q.; Tang, Y. Heteronanowires of MoC-Mo_2C as efficient electrocatalysts for hydrogen evolution reaction. Chem. Sci. 2016, 7, 3399-3405.

[18] Wang, Z.; Ren, X.; Wang, L.; Cui, G.; Wang, H.; Sun, X., A hierarchical $CoTe_2$-$MnTe_2$ hybrid nanowire array enables high activity for oxygen evolution reactions. Chem. Commun. 2018, 54, 10993-10996.

[19] Yan, Y.; Xia, B. Y.; Zhao, B.; Wang, X. A review on noble-metal-free bifunctional heterogeneous catalysts for overall electrochemical water splitting. J. Mater. Chem. A 2016, 4, 17587-17603.

[20] Mahler, B.; Hoepfner, V.; Liao, K.; Ozin, G. A. Colloidal synthesis of 1T-WS_2 and 2H-WS2 nanosheets: applications for photocatalytic hydrogen evolution. J. Am. Chem. Soc. 2014, 136, 14121-7.

[21] Li, H.; Du, M.; Mleczko, M. J.; Koh, A. L.; Nishi, Y.; Pop, E.; Bard, A. J.; Zheng, X. Kinetic Study of Hydrogen Evolution Reaction over Strained MoS_2 with Sulfur Vacancies Using Scanning Electrochemical Microscopy. J. Am. Chem. Soc. 2016, 138, 5123-9.

[22] Zhou, X.; Yang, X.; Li, H.; Hedhili, M. N.; Huang, K.-W.; Li, L.-J.; Zhang, W. Symmetric synergy of hybrid CoS_2-WS_2 electrocatalysts for the hydrogen evolution reaction. J. Mater. Chem. A 2017, 5, 15552-15558.

[23] Liu, Q.; Xie, L.; Liu, Z.; Du, G.; Asiri, A. M.; Sun, X., A Zn-doped Ni_3S_2 nanosheet array as a high-performance electrochemical water oxidation catalyst in alkaline solution. Chem. Commun. 2017, 53, 12446-12449.

[24] Wang, Y.; Liu, S.; Hao, X.; Zhou, J.; Song, D.; Wang, D.; Hou, L.; Gao, F. Fluorine- and Nitrogen-Co doped MoS_2 with a Catalytically Active Basal Plane. ACS Appl. Mater. Interfaces 2017, 9, 27715-27719.

[25] Zhou, K.; Withers, F.; Cao, Y.; Hu, S.; Yu, G.; Casiraghi, C. Raman Modes of MoS_2 Used as Fingerprint of van der Waals Interactions in 2-D Crystal-Based Heterostructures. ACS Nano 2014, 8, 9914-9924.

[26] Pu, Z.; Liu, Q.; Asiri, A. M.; Luo, Y.; Sun, X.; He, Y., 3D macroporous MoS_2 thin film: in situ hydrothermal preparation and application as a highly active hydrogen evolution electrocatalyst at all pH values. Electrochim. Acta 2015, 168, 133-138.

[27] Luo, R.; Luo, M.; Wang, Z.; Liu, P.; Song, S.; Wang, X.; Chen, M. The atomic origin of nickel-doping-induced catalytic enhancement in MoS_2 for electrochemical hydrogen production. Nanoscale 2019, 11, 7123-7128.

[28] Luo, Y.; Li, X.; Cai, X.; Zou, X.; Kang, F.; Cheng, H. M.; Liu, B. Two-Dimensional MoS_2 Confined $Co(OH)_2$ Electrocatalysts for Hydrogen Evolution in Alkaline Electrolytes. ACS Nano 2018, 12, 4565-4573.

[29] Tang, B.; Yu, Z. G.; Seng, H. L.; Zhang, N.; Liu, X.; Zhang, Y. W.; Yang, W.; Gong, H. Simultaneous edge and electronic control of MoS_2 nanosheets through Fe doping for an efficient oxygen evolution reaction. Nanoscale 2018, 10, 20113-20119.

[30] Benson, J.; Li, M.; Wang, S.; Wang, P.; Papakonstantinou, P. Electrocatalytic Hydrogen Evolution Reaction on Edges of a Few Layer Molybdenum Disulfide Nanodots. ACS Appl. Mater. Interfaces 2015, 7, 14113-22.

[31] Li, R.; Yang, L.; Xiong, T.; Wu, Y.; Cao, L.; Yuan, D.; Zhou, W. Nitrogen doped MoS_2 nanosheets synthesized via a low-temperature process as electrocatalysts with enhanced activity for hydrogen evolution reaction. J. Power Sources 2017, 356, 133-139.

[32] Chen, Z.-J.; Cao, G.-X.; Gan, L.-Y.; Dai, H.; Xu, N.; Zang, M.-J.; Dai, H.-B.; Wu, H.; Wang, P. Highly Dispersed Platinum on Honeycomb-like NiO@Ni Film as a Synergistic Electrocatalyst for the Hydrogen Evolution Reaction. ACS Catal. 2018, 8, 8866-8872.

[33] Zhu, P.; Chen, Y.; Zhou, Y.; Yang, Z.; Wu, D.; Xiong, X.; Ouyang, F. A metallic MoS_2 nanosheet array on graphene-protected Ni foam as a highly efficient electrocatalytic hydrogen evolution cathode. J. Mater. Chem. A 2018, 6, 16458-16464.

[34] Zhao, L.; Hong, C.; Lin, L.; Wu, H.; Su, Y.; Zhang, X.; Liu, A. Controllable nanoscale engineering of vertically aligned MoS_2 ultrathin nanosheets by nitrogen doping of 3D graphene hydrogel for improved electrocatalytic hydrogen evolution. Carbon 2017, 116, 223-231.

[35] Mao, Z.; Chen, J.; Yang, Y.; Wang, D.; Bie, L.; Fahlman, B. D. Novel g-C_3N_4/CoO Nanocomposites with Significantly Enhanced Visible-Light Photocatalytic Activity for H_2 Evolution. ACS Appl. Mater. Interfaces 2017, 9, 12427-12435.

[36] Xiong, Q.; Zhang, X.; Wang, H.; Liu, G.; Wang, G.; Zhang, H.; Zhao, H. One-step synthesis of cobalt-doped MoS_2 nanosheets as bifunctional electrocatalysts for overall water splitting under both acidic and alkaline conditions. Chem. Commun. 2018, 54, 3859-3862.

[37] Darabdhara, G.; Amin, M. A.; Mersal, G. A. M.; Ahmed, E. M.; Das, M. R.; Zakaria, M. B.; Malgras, V.; Alshehri, S. M.; Yamauchi, Y.; Szunerits, S.; Boukherroub, R., Reduced graphene oxide nanosheets decorated with Au, Pd and Au-Pd bimetallic nanoparticles as highly efficient catalysts for electrochemical hydrogen generation. J. Mater. Chem. A 2015, 3, 20254-20266.

[38] Li, Y.; Wang, H.; Xie, L.; Liang, Y.; Hong, G.; Dai, H., MoS_2 nanoparticles grown on graphene: an advanced catalyst for the hydrogen evolution reaction. J. Am. Chem. Soc. 2011, 133, 7296-9.

[39] Qu, Y.; Yang, M.; Chai, J.; Tang, Z.; Shao, M.; Kwok, C. T.; Yang, M.; Wang, Z.; Chua, D.; Wang, S.; Lu, Z.; Pan, H. Facile Synthesis of Vanadium-Doped Ni_3S_2 Nanowire Arrays as Active Electrocatalyst for Hydrogen Evolution Reaction. ACS Appl. Mater. Interfaces 2017, 9, 5959-5967.

[40] Liu, P. F.; Yang, S.; Zhang, B.; Yang, H. G. Defect-Rich Ultrathin Cobalt-Iron Layered Double Hydroxide for Electrochemical Overall Water Splitting. ACS Appl. Mater. Interfaces 2016, 8, 34474-34481.

[41] Xing, Z.; Yang, X.; Asiri, A. M.; Sun, X. Three-Dimensional Structures of MoS_2@Ni Core/Shell Nanosheets Array toward Synergetic Electrocatalytic Water Splitting. ACS Appl. Mater. Interfaces 2016, 8, 14521-6.

[42] Guo, Y.; Yao, Z.; Shang, C.; Wang, E. Amorphous Co_2B Grown on $CoSe_2$ Nanosheets as a Hybrid Catalyst for Efficient Overall Water Splitting in Alkaline Medium. ACS Appl. Mater. Interfaces 2017, 9, 39312-39317.

[43] Du, J.; Wang, L.; Bai, L.; Zhang, P.; Song, A.; Shao, G. Effect of Ni Nanoparticles on HG Sheets Modified by GO on the Hydrogen Evolution Reaction. ACS Sustain. Chem. Eng. 2018, 6, 10335-10343.

[44] Jiang, J.; Gao, M.; Sheng, W.; Yan, Y. Hollow Chevrel-Phase $NiMo_3S_4$ for Hydrogen Evolution in Alkaline Electrolytes. Angew. Chem., Int. Ed. 2016, 55, 15240-15245.

[45] Jiang, A.; Nidamanuri, N.; Zhang, C.; Li, Z. Ionic-Liquid-Assisted One-Step Synthesis of CoO Nanosheets as Electrocatalysts for Oxygen Evolution Reaction. ACS Omega 2018, 3, 10092-10098.

[46] Yang, L.; Zhang, L.; Xu, G.; Ma, X.; Wang, W.; Song, H.; Jia, D. Metal–Organic-Framework-Derived Hollow CoS_x@MoS_2 Microcubes as Superior Bifunctional Electrocatalysts for Hydrogen Evolution and Oxygen Evolution Reactions. ACS Sustain. Chem. Eng. 2018, 6, 12961-12968.

[47] Bai, J.; Meng, T.; Guo, D.; Wang, S.; Mao, B.; Cao, M. Co_9S_8@MoS_2 Core-Shell Heterostructures as Trifunctional Electrocatalysts for Overall Water Splitting and Zn-Air Batteries. ACS Appl. Mater. Interfaces 2018, 10, 1678-1689.

[48] Tang, B.; Yu, Z. G.; Seng, H. L.; Zhang, N.; Liu, X.; Zhang, Y. W.; Yang, W.; Gong, H., Simultaneous edge and electronic control of MoS_2 nanosheets through Fe doping for an efficient oxygen evolution reaction. Nanoscale 2018, 10, 20113-20119.

[49] Chen, S.; Li, Y.; Zhang, Z.; Fu, Q.; Bao, X. The synergetic effect of h-BN shells and subsurface B in CoB_x@h-BN nanocatalysts for enhanced oxygen evolution reactions. J. Mater. Chem. A 2018, 6, 10644-10648.

[50] Yuan, X.; Ge, H.; Wang, X.; Dong, C.; Dong, W.; Riaz, M. S.; Xu, Z.; Zhang, J.; Huang, F. Controlled Phase Evolution from Co Nanochains to CoO Nanocubes and Their Application as OER Catalysts. ACS Energy Lett. 2017, 2, 1208-1213.

[51] Zhou, Q.; Zhao, G.; Rui, K.; Chen, Y.; Xu, X.; Dou, S. X.; Sun, W. Engineering additional edge sites on molybdenum dichalcogenides toward accelerated alkaline hydrogen evolution kinetics. Nanoscale 2019, 11, 717-724.

[52] Cheng, P.; Yuan, C.; Zhou, Q.; Hu, X.; Li, J.; Lin, X.; Wang, X.; Jin, M.; Shui, L.; Gao, X.; Nötzel, R.; Zhou, G.; Zhang, Z.; Liu, J. Core-Shell MoS_2@CoO Electrocatalyst for Water Splitting in Neural and Alkaline Solutions. J. Phys. Chem. C 2019, 123, 5833-5839.

[53] Zhao, G.; Lin, Y.; Rui, K.; Zhou, Q.; Chen, Y.; Dou, S. X.; Sun, W. Epitaxial growth of $Ni(OH)_2$ nanoclusters on MoS_2 nanosheets for enhanced alkaline hydrogen evolution reaction. Nanoscale 2018, 10, 19074-19081.

[54] Wang, Y.; Zhu, Y.; Afshar, S.; Woo, M. W.; Tang, J.; Williams, T.; Kong, B.; Zhao, D.; Wang, H.; Selomulya, C. One-dimensional CoS_2-MoS_2 nano-flakes decorated MoO_2 sub-micro-wires for synergistically enhanced hydrogen evolution. Nanoscale 2019, 11, 3500-3505.

[55] Vikraman, D.; Hussain, S.; Akbar, K.; Truong, L.; Kathalingam, A.; Chun, S.-H.; Jung, J.; Park, H. J.; Kim, H.-S. Improved Hydrogen Evolution Reaction Performance using MoS_2-WS_2 Heterostructures by Physicochemical Process. ACS Sustain. Chem. Eng. 2018, 6, 8400-8409.

[56] Zhang, G.; Wang, G.; Liu, Y.; Liu, H.; Qu, J.; Li, J. Highly Active and Stable Catalysts of Phytic Acid-Derivative Transition Metal Phosphides for Full Water Splitting. J. Am. Chem. Soc. 2016, 138, 14686-14693.

[57] Hou, J.; Sun, Y.; Cao, S.; Wu, Y.; Chen, H.; Sun, L. Graphene Dots Embedded Phosphide Nanosheet-Assembled Tubular Arrays for Efficient and Stable Overall Water Splitting. ACS Appl. Mater. Interfaces 2017, 9, 24600−24607.

[58] Meng, T.; Qin, J.; Xu, D.; Cao, M. Atomic Heterointerface Induced Local Charge Distribution and Enhanced Water Adsorption Behavior in a Cobalt Phosphide Electrocatalyst for Self-Powered Highly Efficient Overall Water Splitting. ACS Appl. Mater. Interfaces 2019, 11, 9023-9032.

[59] Wang, Y.; Sun, Y.; Yan, F.; Zhu, C.; Gao, P.; Zhang, X.; Chen, Y. Self-supported NiMo-based Nanowire Arrays as Bifunctional Electrocatalysts for Full Water Splitting. J. Mater. Chem. A 2018, 6, 8479-8487.

[60] Xu, X.; Du, P.; Chen, Z.; Huang, M. An Electrodeposited Cobalt-Selenide-based Film as an Efficient Bifunctional Electro catalyst for Full Water Splitting. J. Mater. Chem. A 2016, 4, 10933-10939.

[61] Zhu, C.; Yin, Z.; Lai, W.; Sun, Y.; Liu, L.; Zhang, X.; Chen, Y.; Chou, S.-L. Fe-Ni-Mo Nitride Porous Nanotubes for Full WaterSplitting and Zn-Air Batteries. Adv. Energy Mater. 2018, 8, 1802327-1802338.

[62] Zhang, Y.; Shao, Q.; Long, S.; Huang, X. Cobalt-molybdenum nanosheet arrays as highly efficient and stable earth-abundant electrocatalysts for overall water splitting. Nano Energy 45 (2018) 448-455.

CHAPTER 4

Enhanced electrocatalytic hydrogen evolution on a plasmonic electrode: the importance of the Ti/TiO_2 adhesion layer

4.1 Introduction

Identification of efficient electrocatalysts other than Pt for the HER is timely and represents a growing field of research and development. The clean and potentially cost-effective pathway for H_2 production *via* electro-reductive water splitting makes H_2 the ultimate fuel of the future [1, 2]. The energy required to drive the reductive water-splitting reaction ($4H^+ + 4e- \rightarrow 2H_2(g)$) necessitates the use of catalysts, with Pt being at present the most active catalyst for the HER in acidic solutions [3, 4].

Polished polycrystalline Pt or platinized Pt electrodes can achieve -10 mA cm^{-2} at an overpotential of $\eta \approx -0.04$ V [5]. The large-scale application of Pt catalysts is yet limited by their high cost and low abundance, motivating researchers in discovering cost-effective alternatives achieving -10 mA cm^{-2} at $\eta \approx -0.1$ V. Yet, only some catalysts such as electrodeposited NiMo and NiMoCo films [4], amorphous molybdenum sulphide films deposited on F-doped tin oxide (FTO) electrodes [6] or ternary pyrite-type cobalt phosphosulphide (CoPS) [7] showed comparable activities attaining -10 mA cm^{-2} at $\eta \approx -0.05$ V [4], -15 mA cm^{-2} at $\eta = -0.20$ V [6], and -10 mA cm^{-2} at $\eta = -0.048$ V [7]. The search for electrocatalytic systems with efficiencies comparable to or even better than platinum remains a demanding task up to now. Nanoporous graphene with single-atom nickel dopants was proposed by Qiu et al. and achieved a current density of -10 mA cm^{-2} at $\eta = -0.05$ V in 0.5 M H_2SO_4 with excellent cyclic stability [8]. Tan et al. demonstrated the interest of 3D nanoporous cobalt phosphide (np-Co_2P) with a pore size of 30 nm for HER with a current density of -10 mA cm^{-2} at $\eta = -0.08$ V [9].

Although substantial progress has been made in this field, the search for HER catalysts focused mainly only on designing platinum-free electrocatalysts, neglecting the integration of other driving sources, especially plasmonic phenomena [10-19]. Plasmonic enhancement is mainly achieved through three mechanisms, namely, far-field scattering, near-field enhancement and charge carrier or resonant energy transfer [20]. While plasmon-enhanced photocatalytic water splitting has been demonstrated by several research groups [21-23], plasmon-mediated electrochemical water reduction has been described only in a few reports [24-30]. These works were mainly based on the coupling of plasmonic nanostructures with few layered MoS_2 materials due to the excellent catalytic activity of MoS_2 for the HER [28-31]. Shi et al. work was based on drop-coating of Au nanorods/MoS_2 nanosheet hybrids onto glassy carbon electrodes, reaching a current density of -10 mA cm^{-2} at η = -0.12 V [11]. The catalytic enhancement was attributed to an increase in carrier density in MoS_2 induced by the injection of hot electrons from the plasmonic nanostructures. Wang et al. reported recently the possibility of boosting electrocatalytic hydrogen evolution over metal-organic frameworks by plasmon-induced hot-electron injection *via* gold nanorods [26]. Upon irradiation with a 808 nm laser, a current density of -10 mA cm^{-2} was recorded at an overpotential of η = -0.135 V. We report here on plasmon-accelerated electrocatalytic reduction of water in acid solution and H_2 production on different plasmonic electrodes. These systems comprise several of the essential components for boosting the electrocatalytic HER: (i) a plasmonic resonant structure in the form of gold nanohole (Au NHs) layers with excellent subwavelength light manipulation properties and electromagnetic field enhancement; (ii) an electrical interface working as a heterogenous electrocatalyst for water reduction, and in one case (iii) a Ti/TiO_2 adhesion layer forming a Mott-Schottky barrier with the nanohole gold layer. We show that under laser illumination at 980 nm (2 W cm^{-2}), an interface comprising next to the Au NHs a thin Ti/TiO_2 (noted S2 in this work), enables the injection of hot electrons from the plasmonic

interface to adsorbed water molecules. A current density of -10 mA cm^{-2} can be attained at an overpotential of $\eta \approx$ -0.045 V. The HER activity of commercial benchmark Pt was not affected by laser illumination and achieved -10 mA cm^{-2} at -0.048 *vs.* RHE.

4.2 Experimental section

4.2.1 Fabrication of gold nanoholes (Au NHs) directly on kapton (S1)

Kapton foils (10×10 mm^2, thickness = 125 μm, DuPont, Circleville, OH, USA) were used. In short, a monolayer of 980 nm polystyrene beads (Microparticles GmbH, Germany) was deposited on the surface of Kapton by self-assembly, followed by SF_6 and oxygen plasma etching for 11 min (5 mTorr) to reduce particle size. The samples were then coated with 50 nm Au at a constant deposition rate of 2 Å s^{-1} using physical vapor deposition. The beads on top of the Kapton were removed by dissolution in chloroform (overnight). The arrays display holes of 630 nm average size and center-to-center spacing of 980 nm.

4.2.2 Fabrication of gold nanoholes (Au NHs) on kapton (S2)

Kapton foils (10×10 mm^2, thickness = 125 μm, DuPont, Circleville, OH, USA) were used. In short, a monolayer of 980 nm polystyrene beads (Microparticles GmbH, Germany) was deposited on the surface of Kapton by self-assembly, followed by SF_6 and oxygen plasma etching for 11 min (5 mTorr) to reduce particle size. The samples were then coated with ≈2 nm Ti followed by 50 nm Au at a constant deposition rate of 2 Å s^{-1} using physical vapor deposition. The beads on top of the Kapton were removed by dissolution in chloroform (overnight). The arrays display holes of 630 nm average size and center-to-center spacing of 980 nm.

4.2.3 Fabrication of Ti/TiO_2/on kapton (S3)

Kapton foils (10×10 mm^2, thickness = 125 μm, DuPont, Circleville, OH, USA) were used. In short, a monolayer of 980 nm polystyrene beads (Microparticles GmbH, Germany) was deposited on the surface of Kapton by self-assembly, followed by SF_6 and oxygen plasma

etching for 11 min (5 mTorr) to reduce particle size. The samples were then coated with 50 nm Ti at a constant deposition rate of 2 Å s^{-1} using physical vapor deposition. The beads on top of the Kapton were removed by dissolution in chloroform (overnight). The arrays display holes of 630 nm average size and center-to-center spacing of 980 nm.

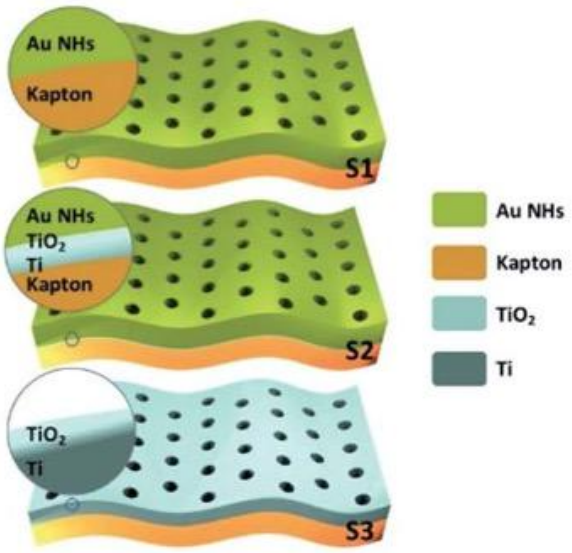

Figure 1. Schematics of the three types of investigated systems.

4.2.4 Electrochemical experiments

Electrochemical measurements were performed with a ModuLab-MTS electrochemical test station (Solartron, France) in a standard three-electrode system with the plasmonic electrodes (or Pt) as the working electrode, a carbon plate as the counter electrode and an Ag/AgCl (3.5 M KCl) electrode as the reference electrode. The measured potentials were converted to that relative to the reversible hydrogen electrode (RHE) according to:

$$E_{RHE} = E_{Ag/AgCl} + 0.059 * pH + E°_{Ag/AgCl}, \text{ with } E°_{Ag/AgCl} = 0.1976 \text{ V } (25°C).$$

Cyclic voltammetry (CV) and linear sweep voltammetry (LSV) measurements were performed in 0.1 M H_2SO_4 solution at a scan rate of 50 mV s^{-1}. Electrochemical impedance data were acquired over a frequency range of 100 kHz to 0.01 Hz. The electrochemically active surface area (A) in the electrochemical cell was derived from the linear plot of the peak current as a function of the square root of the scan rate according to equation:

$$A=s/(268600 \times n^{3/2} \times D_f^{1/2} \times c_f v^{1/2})$$

where n is the number of electrons transferred in the redox event (n = 1), D_f is the diffusion coefficient of ferrocenemethanol (7.5×10^{-6} cm^2 s^{-1}), c_f is the concentration of ferrocenemethanol (0.0001 mol cm^{-3}), and s is the slope of the linear fit to the data. The exposed area of the working electrode was 0.28 cm^2.

For plasmon-enhanced electrocatalysis, the electrode was illuminated with light from a continuous wave laser (980 and 808 nm, Gbox model, Fournier Medical Solution) with a laser power output between 0.5 and 2 W cm^{-2}. The temperature changes were captured by an infrared camera (Thermovision A40) and treated using ThermaCam Researcher Pro 2.9 software.

4.2.5 Faradic efficiency

The Faradic efficiency (FE) of H_2 evolution was calculated by comparing the amount of formed H_2 volumetrically to that calculated from potentiostatic cathodic electrolysis (assuming 100% FE). Assuming a one electron redox process, the number of moles (n) of H_2 formed during electrolysis can be calculated according to:

$$n = Q/2F$$

with F is the Faraday constant (96485 C mol^{-1}) and Q is the charge passed during the experiment.

To determine the volume of H_2 formed, the outlet of the tightly closed electrolytic cell was connected to a tube that has been inserted into a beaker of 1 mL filled with water. When H_2 gas is generated, the gas will flow into the tube and start displacing the water in the beaker.

4.3 Results and discussion

4.3.1 Nanoperforated Au thin film electrodes

The tunable optical properties of Au nanostructures and their good electrical conductivity make noble metal ordered architectures ideally suited for the construction of plasmonic

electrodes [32, 33]. Colloidal lithography was adopted to generate different types of nanostructured electrodes on Kapton (K) (**Figure 1**).

The samples are structured and labeled as follows: (S1) K/Au NHs (50 nm), (S2) K/Ti/TiO_2/Au NHs (50 nm), (S3) K/Ti/TiO_2 (30 nm). Ultra-thin (< 3 nm) disordered adhesion layers of Ti, obtained by physical vapor deposition, as those used here, typically display a metal-insulator transition and contain amorphous TiO_2 [34]. Note that when titanium is exposed to air, a native TiO_2 layer is formed spontaneously.

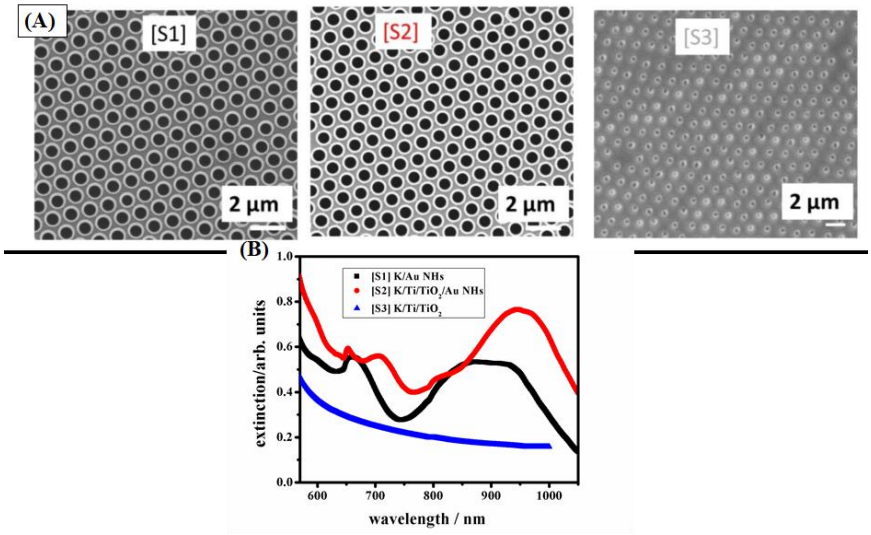

Figure 2. (A) SEM images of the investigated electrodes. The scale bar is 2 µm. (B) UV/vis absorption spectra of the different interfaces: S1: K/Au NHs (50 nm) (black), S2: K/Ti/TiO_2/Au NHs (50 nm) (red), S3: K/Ti/TiO_2 (30 nm) (blue).

The scanning electron microscopy (SEM) images of the specimens are displayed in **Figure 2A**, showing the characteristics of nanoperforated thin metal film structures. Electrodes S1 and S2 support different localized surface plasmon resonance (LSPR) modes (**Figure 2B)**, while S3 shows no plasmonic response. Specifically, S1 displays a plasmon band at 660 nm and a broad absorption (857-926 nm), due to the excitation of surface plasmon waves in the Au NHs, acting as two-dimensional diffraction gratings that convert incident photons into SP waves [35]. The structure S2 displays, next to the plasmon band at

653 nm, an intense absorption band centered at around 980 nm with, however, a large half-wave width. This indicates a certain distribution of Au NH sizes with different LSPR maxima in the near infrared region.

4.3.2 Electrocatalytic activity towards HER

The electrochemical behavior of the electrodes using ferromagnetic as a redox active probe in aqueous solution reveals reversible voltammograms for S1 and S2 electrodes with a ΔE = 62 mV. The electrode S3 displays a quasi-reversible electron transfer behavior (**Figure 3A**) due to the presence of amorphous TiO_2, with poor electrical conductivity [17].

The electrocatalytic activity of the S1-S3 samples towards HER in acidic solution was investigated in a N_2-saturated 0.1 M H_2SO_4 electrolyte at room temperature. Their behavior with and without light illumination is presented in **Figure 3**. As shown in **Figure 3**, S3 ($K/Ti/TiO_2$) demonstrates poor HER activity [23]. In contrast, the surfaces with Au NHs exhibit electrocatalytic activity towards HER with onset potentials shifting positively from -0.102 V (*vs.* RHE) (S1) to -0.098 V (vs. RHE) (S2). For comparison, the onset potential of a Pt foil electrode under the same conditions is -0.025 V (*vs.* RHE) (**Figure 3)**.

Upon illumination with a laser at 980 nm (2 W cm^{-2}), the HER activity of S1 and S2 is enhanced, while that of S3 remains almost unchanged (**Figure 3C**). Interestingly, S2 is outperforming the other surfaces and has a behavior close to that of a Pt sheet electrode under the same conditions. A comparison of the overpotentials η needed to achieve -10 and -100 mA cm^{-2} current densities (**Table 1**) suggests that the required potential energy for HER is reduced on S2. With an overpotential of η = -0.045 V at -10 mA cm^{-2}, S2 approaches the thermodynamic potential of the HER (i.e. 0.0 V). It is also comparable to values attained on Pt foil electrodes under the same conditions, recording a current density of -10 mA cm^{-2} at η = -0.043 V under light illumination (dotted curves in **Figure 3**). This change in η is most likely linked to the increase in the surface temperature of the Pt foil under light irradiation. Indeed,

the solution temperature increased by about 5 ℃ under light irradiation. Note that the HER activity of S3 was not affected by light illumination.

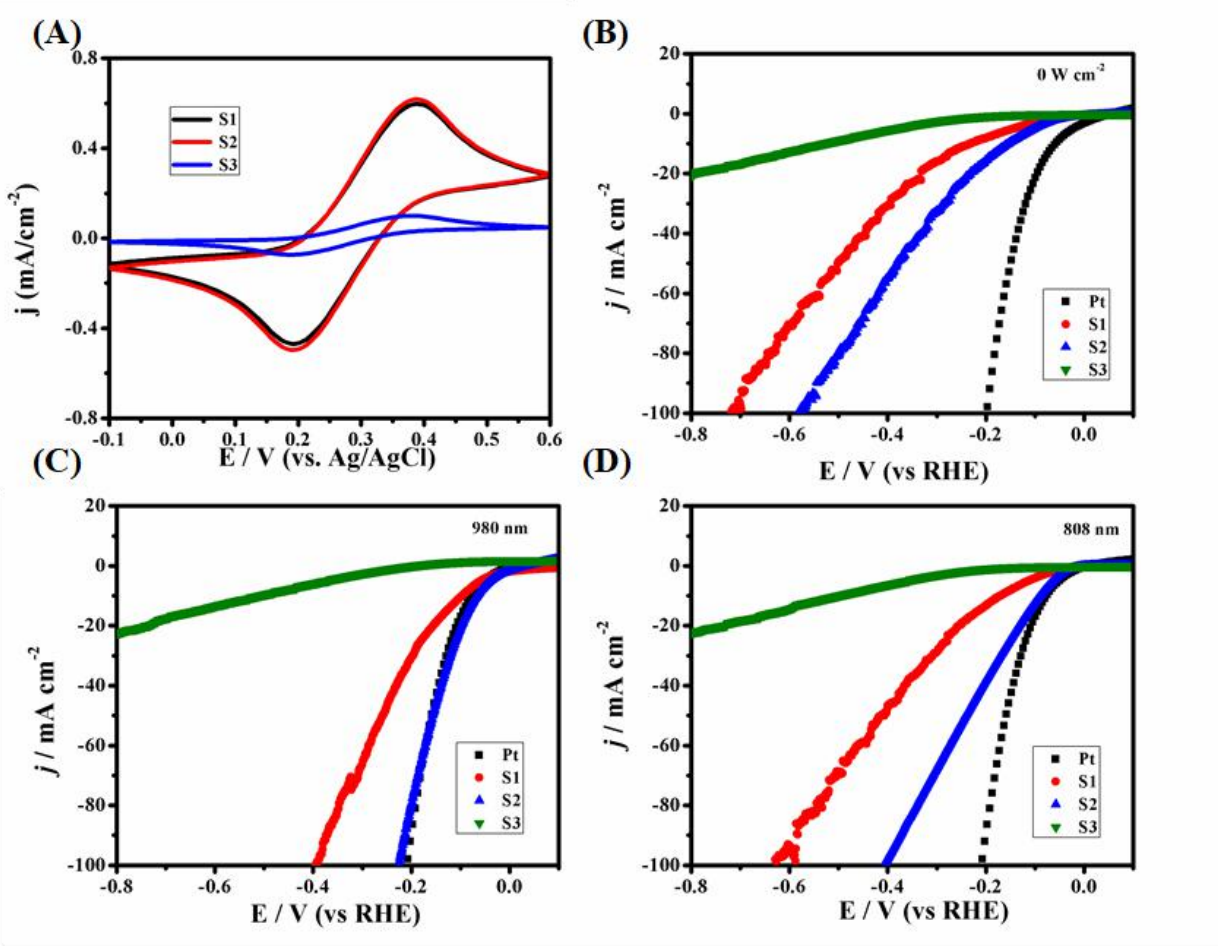

Figure 3. Characteristics of the plasmonic electrodes. (A) Cyclic voltammograms of the different surfaces. S1: K/Au NHs (50 nm) (red), S2: K/Ti/TiO_2/Au NHs (50 nm) (blue), S3: K/Ti/TiO_2 (30 nm) (green) in ferrocenemethanol (1 mM)/KCl (0.1 M). The scan rate is 50 mV s^{-1}. (B) HER polarization curves of S1, S2, S3 and Pt in 0.1 M H_2SO_4 at a scan rate of 50 mVs^{-1} without illumination. (C) HER polarization curves of S1, S2, S3 and Pt under 980 nm light irradiation at 2 W cm^{-2} for 10 min. (D) HER polarization curves of S1, S2, S3 and Pt under 808 nm light irradiation at 2 W cm^{-2} for 10 min. All measurements were performed at room temperature.

In addition, the HER activities of S1, S2, S3 and Pt under illumination at 808 nm (2 W cm^{-2}) were determined (**Figure 3D**). The performance of S2 is decreased as compared to that observed under illumination at 980 nm, while that of S1, S3, and Pt remained the same. These findings confirm that the HER enhancement of S2 is related to a plasmon-mediated effect. Indeed, S2 exhibits an absorption minimum at 808 nm. However, S2 displays an intense LSPR band at ~980 nm, which is responsible for the strongly enhanced HER electrocatalytic activity under this wavelength illumination. These findings confirm that the HER enhancement of S2 is related to a plasmon-mediated effect. The same is true for S1.

Table 1. Overpotentials recorded for S1, S2 and S3 electrodes in 0.1 M H_2SO_4 with and without irradiation at 980 nm (2 W cm^{-2}) or 808 nm (2 W cm^{-2}) for 600 s in thermostated electrolyte (24°C).

Substrate	**Wavelength**	**η (V) (-10 mA cm^{-2})**	**η (V) (-100 mA cm^{-2})**
S1	-	-0.212	-0.601
	980 nm	-0.120	-0.395
	808 nm	-0.201	-0.597
S2	-	-0.183	-0.598
	980 nm	-0.045	-0.238
	808 nm	-0.163	-0.431
S3	-	-0.533	-
	980 nm	-0.462	-
	808 nm	-0.462	-
Pt	-	-0.069	-0.201
	980 nm	-0.043	-0.198
	808 nm	-0.043	-0.198

Table 2. Comparison of S2 performance to literature values.

Interface	Conditions	η (V) (-10 mA cm^{-2})	η (V) (-100 mA cm^{-2})	Tafel ($mV\ dec^{-1}$)	Ref.
Au NHs on Ti/TiO_2	980 nm 2 W cm^{-2}	-0.045	-0.238	35	this work
Amorphous MoS_2	No light	-0.180	-0.31	40	6
CoPS	No light	-0.048	-	56	7
Nanoporous graphene with Ni dopants	-	-0.05	-	45	8
3D nanoporous metal phosphides	No light	-0.080	-	44	9
Au NRs on CoFe-MOF	808 nm	-0.135	-0.19	94	26
MoS_2@$Cu_{1.75}S$-Au	650nm 0.1 W cm^{-2}	-0.120	-	39	27
MoS_2@Au	500 W Uv/Vis	-0.300	-	74	28
N-doped porous carbon@Au	531 nm	-0.099	-	37	29
MoS_2@NPG	Xe lamp 0.1 W cm^{-2}	-0.167	-0.27	38	30
Au@Ag/MoS_2	690 nm 25 mWcm^{-2}	-0.420	-0.55	155	36

Overall, the HER activity of S2 under 980 nm illumination is boosted when compared to other plasmonic HER systems (**Table 2**). The results are competitive with the recently reported 3D nanoporous plasmonic heterostructures, formed by chemically dealloying a 700 nm-thick Au-Ag alloy and post-coated with a monolayer of MoS_2 by chemical vapor deposition [30]. This electrocatalytic interface exhibited hydrogen production at an overpotential of -0.167 V (*vs.* RHE) under visible light illumination at -10 mA cm^{-2}. In this set up, the electrocatalyst is the MoS_2 monolayer and the HER performance was due to an efficient transfer of hot electrons from the gold nanopores to the monolayer MoS_2. In contrast to these plasmonic enhanced electrocatalytic systems, S2 formation is easy on the macroscale (>10 cm^2) and the use of colloidal lithography makes the process highly reproducible.

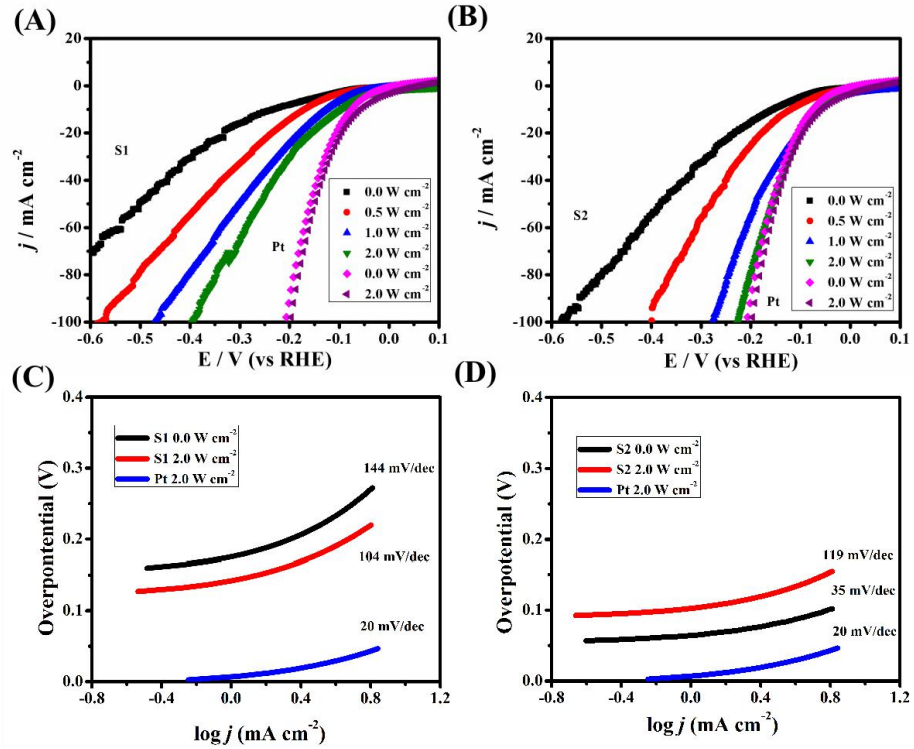

Figure 4. Behavior of nanopatterned gold-based plasmonic electrodes towards HER. (A) HER polarization curves of S1 illuminated at 980 nm at different laser densities, scan rate = 50 mV s^{-1}. (B) HER polarization curves of S2 and Pt illuminated at 980 nm at different laser power densities, scan rate = 50 mV s^{-1}. (C, D) Tafel plots of the indicated electrodes derived from the initial stage of the HER polarization curves displayed in panels (A, B).

As expected, the acceleration of electrochemical water reduction depends on the incident laser power density (**Figure 4**). The onset HER potential decreases as the laser power increases from 500 mW cm^{-2} to 2 W cm^{-2}. At laser powers > 1 W cm^{-2}, the polarization curves reached a pseudo steady state. Based on the polarization curves, the corresponding Tafel plots were estimated to evaluate the influence of light irradiation on the HER kinetics. The Tafel slopes without light activation are 144 mV/dec (S1) and 119 mV/dec (S2). Under 980 nm illumination at 2.0 W cm^{-2}, they decrease respectively to 104 mV/dec (S1) and 35 mV/dec (S2) (**Figure 4**), indicating a good electrocatalytic activity, approaching that of Pt of 28 mV/dec. The reduction in the Tafel slope suggests that the surface adsorption of hydrogen is increasing. Under light irradiation, hydrogen bonds can thus be directly broken with desorption of hydrogen being the rate limiting step [11, 29].

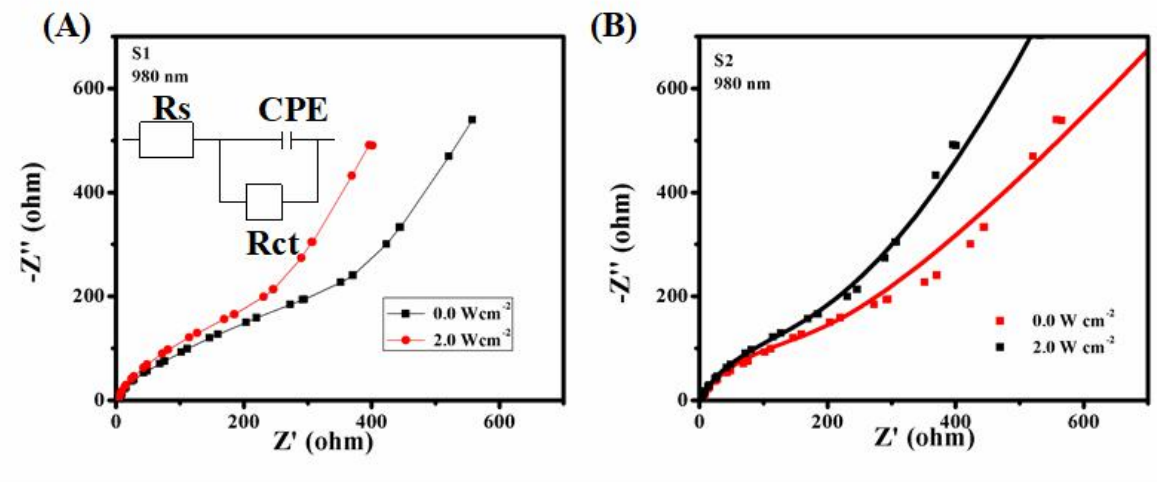

Figure 5. Nyquist plots of S1 (A) and S2 (B) under illumination at 980 nm, 2 W cm^{-2} for 600 s and without illumination over the frequency range of 100 kHz to 0.01 Hz. Points are experimental data and curves are fits to the data. The equivalent circuit used for analysis is shown in the inset of panel (A).

In addition, electrochemical impedance spectroscopy (EIS) measurements were carried out (**Figure 5**) to see if the charge transfer resistance (R_{CT}) changes under light illumination.

In the case of S2 electrode, the diameter of the semicircle in the Nyquist plot is slightly decreased under light illumination at 980 nm (2 Wcm^{-2}) from 188±6 to 127±6 Ω cm^{-2}, revealing an enhancement of electron transfer rate. For S1, the charge transfer resistance without light illumination is comparable to that of S2 (198±11 Ω cm^{-2}). It decreases to 167±12 Ω cm^{-2} upon light illumination with 980 nm laser at 2 Wcm^{-2} (**Figure 5**).

4.3.3. Mechanism

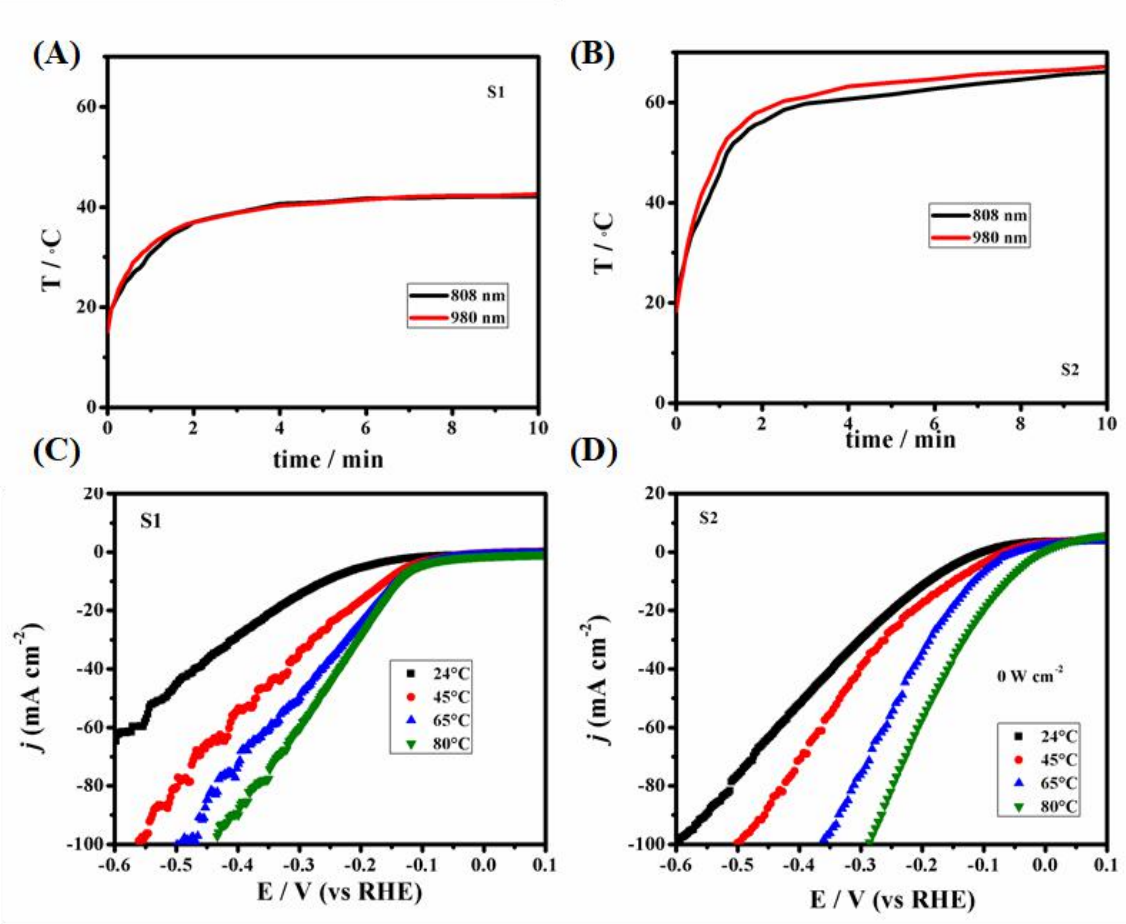

Figure 6. (A) Photothermal heating curves of S1 immersed in 0.1 M H_2SO_4 upon laser light irradiation at 980 nm (full curve) and 808 nm (dashed curve) for 10 min at 2 W cm^{-2}. (B) Photothermal heating curves of S2 immersed in 0.1 M H_2SO_4 and exposed to laser light of 980 nm (full curve) and 808 nm (dashed curve) for 10 min at 2 W cm^{-2}. (C) HER polarization curves at 24 °C, 45 °C, 65 °C and 80 °C in 0.1 M H_2SO_4 solution for S1. (D) HER polarization curves at 24 °C, 45 °C, 65 °C and 80 °C in 0.1 M H_2SO_4 solution for S2.

To understand the origin of the current enhancement, the HER reaction was performed at different solution temperatures up to 80°C (**Figure 6)**. The temperature corresponds to the surface temperature as determined with a thermocouple attached to the sample when immersed in 0.1 M H_2SO_4 and irradiated with a 980 nm laser at 2 W cm^{-2} for 10 min. We observed that the thermal heating effect upon HER is weaker than the plasmonic effect.

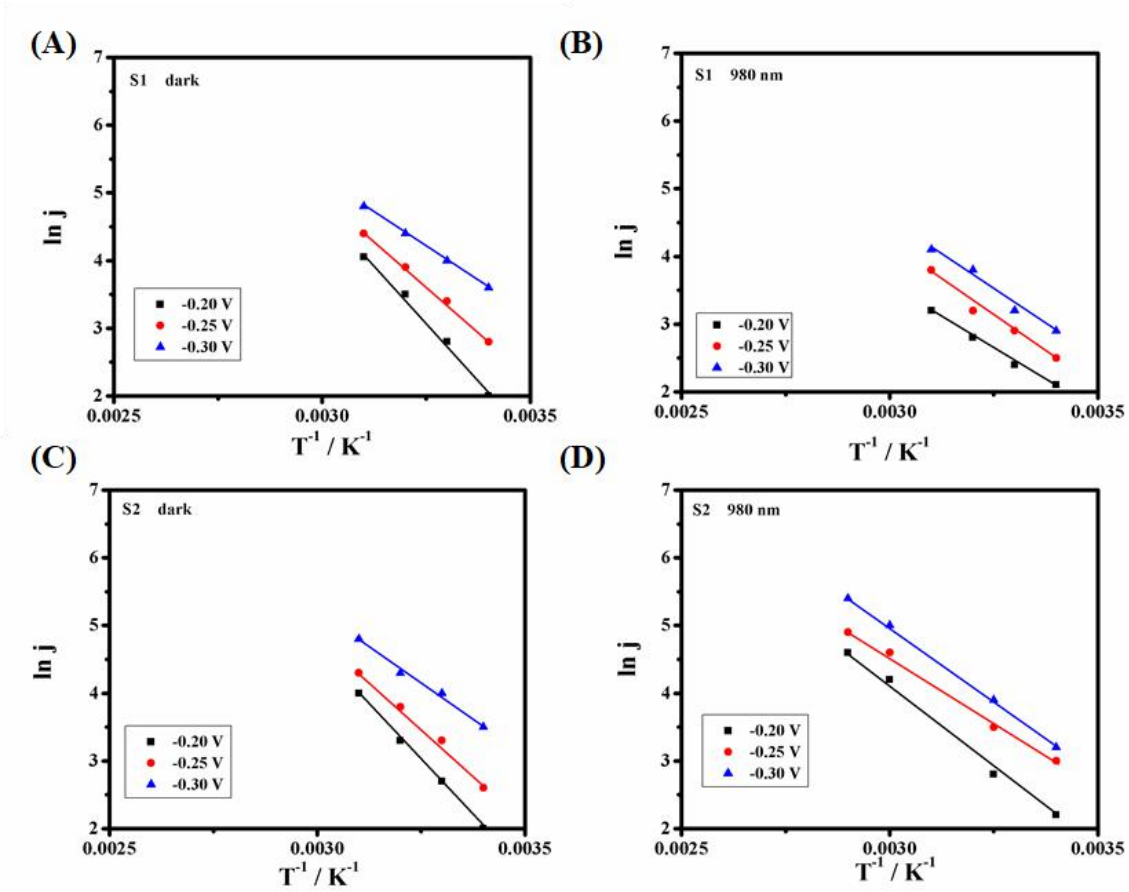

Figure 7. Arrhenius plots of the current density obtained for **S1** (A) in the dark and (B) under light illumination at 980 nm for 10 min. Arrhenius plots of the current density obtained for **S2** (C) in the dark and (D) under light illumination at 980 nm for 10 min at overpotentials of -0.20, 0.25 and -0.30 V. The activation energy (Ea) was determined from the slope of the Arrhenius plots according to $j \propto \exp(-E_a/RT)$, with R being the universal gas constant (8.314 J mol^{-1}) and T the temperature (K).

To gain more evidence of the LSPR enhanced HER activity, the activation energy (E_a) of HER was determined under light illumination at 980 nm and compared to that determined by heating of the solution. The plots of ln *j vs.* 1/T revealed a linear relationship (**Figure 7**) in both cases. For S2, using the Arrhenius equation, the value of E_a under light irradiation was estimated to be 44±5 kJ mol^{-1}, while in dark it was 94±1 kJ mol^{-1} (**Figure 8A**).

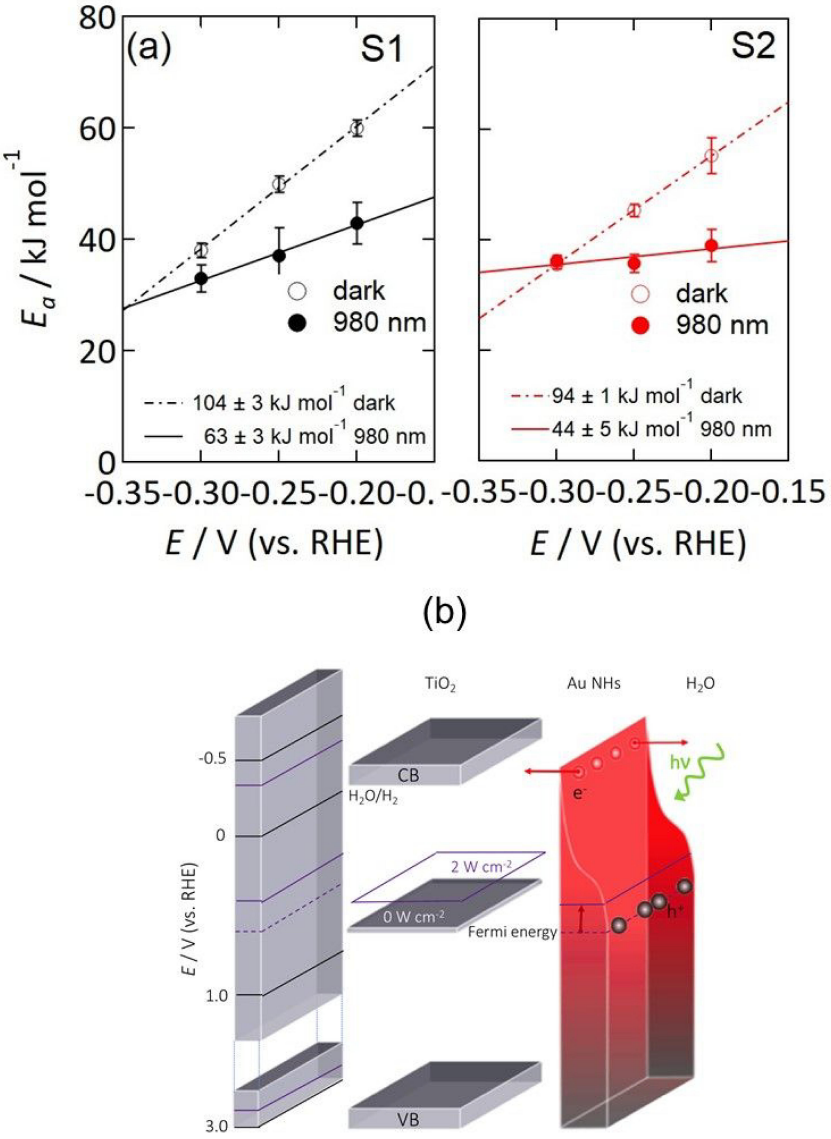

Figure 8. Mechanistic considerations for HER. (A) Activation energy as a function of overpotential upon 980 nm light irradiation (closed symbols) and in dark (open symbols). (B) Schematic presentation of the mechanism involved in HER.

As observed by Wang et al. Recently by investigating hydrogen evolution over metal−organic frame-works through plasmon-induced hot-electron injection,[26] the slopes of S1 and S2 of Ea vs. overpotential graph (**Fig. 8A**) under light are smaller compared to those in the dark. The decreased slope for S2 originates from direct hot-electron injection into the substrate due to plasmon activation. Plasmon-induced processes generated a significantly higher HER activity of S2 due to the formation of hot electrons [13, 26]. This observation is adequately supported by the hot-electron-induced H_2 dissociation rate being increased by almost 2 orders of magnitude [13].

On the basis of the above results, the expected mechanism of the enhanced activity toward HER under laser irradiation is the following: under laser excitation, surface plasmons are generated on the nanopatterned gold films forming electron-hole pairs (**Figure 8B**). The generated hot electrons can then follow different pathways on S2: (i) recombination with the formed holes in the Au NHs layer, (ii) direct electrochemical reduction of water on the Au NHs surface, or (iii) injection into the conducting band of the Ti/TiO_2 semiconductor adhesion layer followed by water reduction.

In the case of S1, where Au NHs are directly deposited on Kapton, no injection into the conduction band of the Ti/TiO_2 semiconductor adhesion layer occurs and only direct electro-chemical reduction of water to hydrogen gas will occur. This results in a less efficient plasmon enhanced HER reaction. Indeed, for S1, the value of Ea under light irradiation is estimated to be 63±3 kJ mol^{-1}, while in dark it is 104±3 kJ mol^{-1}. In this case, only direct electrochemical reduction of water occurs through the generation of hot electrons.

In S2, both direct electrochemical reduction of water and injection of hot electrons *via* the Mott-Schottky barrier into the thin Ti/TiO_2 layer might occur, reflecting a low *Ea* under light irradiation of 44±5 kJ mol^{-1},assuming that the electron injection is faster than the electron-hole recombination process.

The fast generation and injection of hot electrons affect the current density profile abruptly upon laser irradiation, as illustrated in **Figure 9A**, when S2 is biased at -0.043 V (*vs.* RHE). Interestingly, the surface temperature evolution of S2 under 808 and 980 nm illumination at 2W cm^{-2} is similar, pointing again to the key role of the hot electrons in the process rather than a solely thermally-driven reaction.

4.3.4. Reproducibility

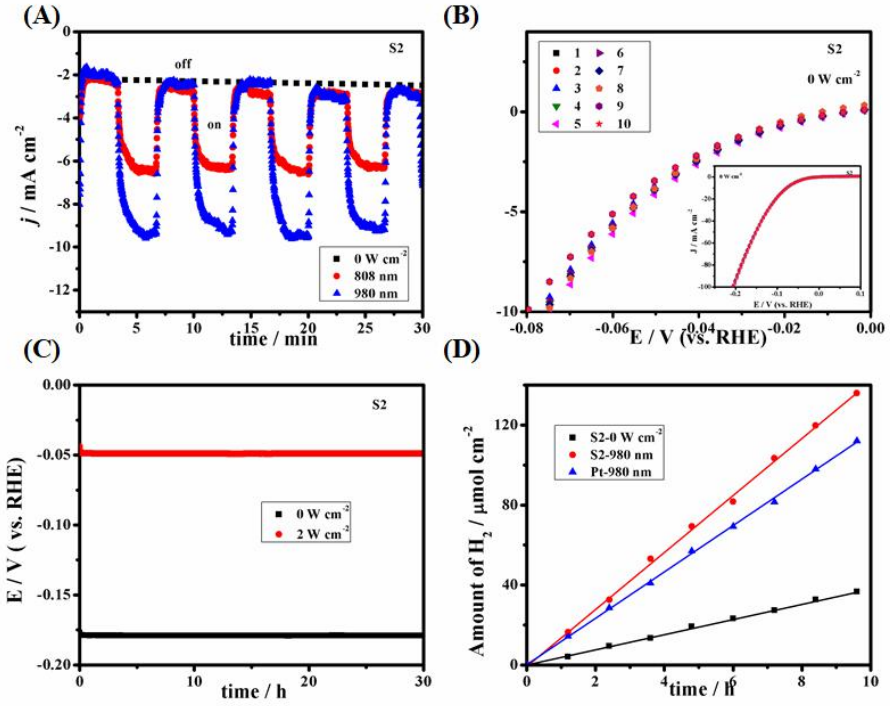

Figure 9. Mechanistic considerations of the HER. (A) Current density-time curves under illumination at 980 nm (red), 808 nm (black) at 2 W cm^{-2} and with no illumination (dashed blue) of **S2**. (B) HER polarization curves of 10 **S2** interfaces in 0.1 M H_2SO_4 at a scan rate of 50 mV s^{-1} in dark. (C) HER stability tests of **S2** at j = -10 mA cm^{-2} with (red, 2 W cm^{-2}) and without light (black) illumination by following the change of the overpotential with time. (D) H_2 production efficiency catalyzed by **S2** at a potential of -0.04 V in 0.1 M H_2SO_4 with and without light irradiation. The theoretical efficiency (lines) was calculated according to the cumulative charge, assuming a 100% Faradic efficiency for H_2 production. The current density was j = -10 mA cm^{-2}. Data for Pt is shown as well (black symbols).

The HER activities are highly reproducible as seen in the curves recorded on 10 different S2 specimens (**Figure 9B**). As the stability is one of the key factors in determining the usefulness of an electrocatalyst, the long-term stability of Au NHs plasmonic catalyst was assessed by overpotential-time transients plots in an acid environment. **Figure 9C** depicts the chronopotentiometric curves of S2 in 0.1 M H_2SO_4 aqueous solution at a current density j = -10 mA cm^{-2}. The overpotential-time measurements indicate an almost steady overpotential without any significant decay during 35 h of continuous HER, revealing excellent durability of the interface. The faradic yields of H_2 production were in addition found to be quantitative within the experimental errors (**Figure 9D**). Up to 52 μmol cm^{-2} H_2 was formed after irradiation for 3 h, which represents a 4-fold enhancement compared to S2 without activation. The faradaic efficiency was determined as 97.2%.

4.4 Conclusion

In conclusion, nanoperforated Au structures coupled *via* Ti/TiO_2 adhesion layers to underlying Kapton substrates have been constructed as plasmonic electrocatalytic electrodes for catalyzing HER in acidic medium. Upon light irradiation at 980 nm, the overpotential at a current density of -10 mA cm^{-2} decreases from -0.183 V to -0.045 V *vs*. RHE. This HER activity of the plasmonic electrodes is comparable to that of Pt where under the same conditions for which an overpotential of -0.049 V *vs*. RHE was required. The interface sustains the hydrogen evolution reaction for several hours without surface poisoning or electrode degradation, as evidenced by the stable current density over time. Mechanistic investigations revealed that fast hot electron injection into the underlying Ti/TiO_2 layer is partially responsible for the enhanced HER activity. The good light trapping behavior of the plasmonic electrodes might in addition allow direct electrochemical reduction of water due to a decrease in the HER activation energy under light irradiation. While TiO_2 is indeed one of the most promising semiconductors at present due to a thorough under- standing of the role of

the TiO_2 polymorph, any other semi- conductor can be used for this application. Our findings reveal that nanopatterned Au electrodes, in the absence of metal oxide semiconductors, display unique plasmonic enhanced HER.

4.5 References

[1] Turner, J. A. Sustainable hydrogen production. Science 2004, 305, 972-974.

[2] Fang, M.; Dong, G.; Wei, R.; Ho, J. C. Hierarchical Nanostructures: Design for Sustainable Water Splitting. Adv. Energy. Mater. 2017, 7, 1700559.

[3] Esposito, D. V.; Hunt, S. T.; Stottlemyer, A. L.; Dobson, K. D.; McCandless, B. E.; Birkmire, R. W.; Chen, J. G. Low-cost hydrogen-evolution catalysts based on monolayer platinum on tungsten monocarbide substrates. Angew. Chem. Int. Ed. 2010, 49, 9859-9862.

[4] McCrory, C. C. L.; Jung, S.; Ferrer, I. M.; Chatman, S. M.; Peters, J. C.; Jaramillo, T. F. Benchmarking hydrogen evolving reaction and oxygen evolving reaction electrocatalysts for solar water splitting devices. J. Am. Chem. Soc. 2015, 137,4347.

[5] Morales-Guio, C. G.; Ster, L.-A.; Hu, X. Nanostructured hydrotreating catalysts for electrochemical hydrogen evolution. Chem. Soc. Rev. 2014, 43, 6555-6569.

[6] Merki, D.; Fierro, S.; Vrubek, H.; Hu, X. Amorphous molybdenum sulfide films as catalysts for electrochemical hydrogen production in water. Chem. Sci. 2011, 1, 1262-1267.

[7] Caban-Acevedo, M.; Stone, L. M.; Schmidt, J. R.; Thomas, J. G.; Ding, Q.; Chang, H.-C.; Tasi, M.-L.; He, J.-H.; Jin, S. Efficient hydrogen evolution catalysis using ternary pyrite-type cobalt phosphosulphide. Nat. Mater. 2015, 14, 1245-1253.

[8] Qui, H.-J.; Ito, Y.; Cong, W.; Tan, Y.; Liu, P.; Hirata, A.; Fujita, T.; Tang, Z.; Chen, M. Nanoporous Graphene with Single-Atom Nickel Dopants: An Efficient and Stable

Catalyst for Electrochemical Hydrogen Production. Angew. Chem., Int. Ed. 2015, 54, 14031-14035.

[9] Tan, Y.; Wang, H.; Liu, P.; Cheng, C.; Zhu, F.; Hirata, M. 3D Nanoporous Metal Phosphides toward High-Efficiency Electrochemical Hydrogen Production. Adv. Mater. 2016, 28, 2951.

[10] Robatjazi, H.; Bahauddin, S. M.; Doiron, C.; Thomann, I. Direct Plasmon-Driven Photoelectrocatalysis. Nano Lett. 2015, 15, 6155-6161.

[11] Shi, Y.; Wang, J.; Wang, C.; Zhai, T.-T.; Bao, W. J.; Xu, J.-J.; Xia, X.-H.; Chen, H.-Y. Hot Electron of Au Nanorods Activates the Electrocatalysis of Hydrogen Evolution on MoS_2 Nanosheets. J. Am. Chem. Soc. 2015, 137, 7365-7370.

[12] Yan, L.; Wang, F.; Meng, S. Quantum Mode Selectivity of Plasmon-Induced Water Splitting on Gold Nanoparticles. ACS Nano 2016, 10, 5452-5458.

[13] Mukherjee, S.; Zhou, L. N.; Good man, A. M.; Large, N.; Ayala-Orozco, C.; Zhang, Y.; Nordlander, P.; Halas, N. J. Hot-electron-induced dissociation of H_2 on gold nanoparticles supported on SiO_2. J. Am. Chem. Soc. 2014, 136, 64-67.

[14] Murdoch, M.; Waterhouse, G. I. N.; Nadeem, M. A.; Metson, J. B.; Keane, M. A.; Howe, R. F.; Llorca, J.; Idriss, H. The effect of gold loading and particle size on photocatalytic hydrogen production from ethanol over Au/TiO_2 nanoparticles. Nat. Chem. 2011, 3, 489-492.

[15] Chiu, Y.-H.; Naghedeh, S. B.; Lindley, S. A.; Lai, T.-H.; Kui, M.-Y.; Chang, K.-D.; Zhang, J. Z.; Hsu, Y.-J. Yolk-shell nanostructures as an emerging photocatalyst paradigm for solar hydrogen generation. Nano Energy 2019, 62, 289-298.

[16] Hsieh, P.-Y.; Chiu, Y.-H.; Lai, T.-H.; Fang, M.-J.; Wang, Y.-T.; Hsu, Y.-J. TiO_2 Nanowire-Supported Sulfide Hybrid Photocatalysts for Durable Solar Hydrogen Production. ACS Appl. Mater. Interfaces 2019, 11, 3, 3006-3015.

[17] Pu, Y.-C.; Wang, G.; Chang, K.-D.; Ling, Y.; Lin, Y.-K.; Fitzmorris, B.-C.; Liu, C.-M.; Lu, X.; Tong, Y.; Zhang, J.-Z.; Hsu, Y.-J.; Li, Y. Au Nanostructure-Decorated TiO_2 Nanowires Exhibiting Photoactivity Across Entire UV-visible Region for Photoelectrochemical Water Splitting. Nano Lett. 2013, 8, 3817-3823.

[18] Li, J.-M.; Tsao, C.-W.; Fang, M.-J.; Chen, C.-C.; Liu, C.-W.; Hsu, Y.-J. TiO_2-Au-Cu_2O Photocathodes: Au-Mediated Z-Scheme Charge Transfer for Efficient Solar-Driven Photoelectrochemical Reduction. ACS Appl. Nano Mater. 2018, 1, 12, 6843-6853.

[19] Chiu, T.-H.; Lai, T.-H.; Kuo, M.-Y.; Hsieh, P.-Y.; Hsu, Y.-J. H. Photoelectrochemical cells for solar hydrogen production: Challenges and opportunities. APL Mater. 2019, 7, 080901.

[20] Jang, Y. H.; Jang, Y. J.; Kim, S.; Quan, L. N.; Chung, K.; Kim, D. H. Plasmonic Solar Cells: From Rational Design to Mechanism Overview. Chem. Rev. 2016, 116, 14982.

[21] Mukherjee, S.; Libisch, F.; Large, N.; Neumann, P.; Brown, L. V.; Cheng, J.; Britt Lassite, J.; Carte, E. A. A.; Nordlander, P.; Halas, N. J. Hot electrons do the impossible: plasmon-induced dissociation of H_2 on Au. Nano. Lett. 2013, 13, 240-247.

[22] Li, X.; Guo, S.; Kan, C.; Zhu, J.; Tong, T.; Ke, S.; Choy, W. C. H.; Wei, B. MoS_2 hybrid structures for efficient photocatalytical hydrogen production via strongly plasmonic coupling effect. Nano Energy 2016, 30, 549-558.

[23] Hou, B.; Shen, L.; Shi, H.; Kapadia, R.; Cronin, S. B. Hot electron-driven photocatalytic water splitting. Phys. Chem. Chem. Phys. 2017, 19, 2877.

[24] Cheng, H.; Klapproth, M.; Sagalchik, A.; Li, S.; Thomas, A. Ordered mesoporous $WO_{2.83}$: selective reduction synthesis, exceptional localized surface plasmon resonance and enhanced hydrogen evolution reaction activity. J. Mater. Chem. A 2018, 6, 2249.

[25] Shi, Y.; Wang, J.; Wang, C.; Zhai, T.-T.; Bao, W.-J.; Xu, J.-J.; Xia, X.-H.; Chen, H.-Y. Hot Electron of Au Nanorods Activates the Electrocatalysis of Hydrogen Evolution on MoS_2 Nanosheets. J. Am. Chem. Soc. 2015, 137, 7365-7370.

[26] Wang, S. S.; Jiao, L.; Qian, Y.; Hu, W.-C.; Xu, G.-Y.; Wang, C.; Jiang, H.-L. Boosting Electrocatalytic Hydrogen Evolution over Metal-Organic Frameworks by Plasmon-Induced Hot-Electron Injection. Angew. Chem., Int. Ed. 2019, 58, 10713-10717.

[27] Cui, J.; Jiang, R.; Lu, W.; Xu, S.; Wang, L. Plasmon-Enhanced Photoelectrical Hydrogen Evolution on Monolayer MoS_2 Decorated $Cu_{1.75}S$-Au Nanocrystals. Small 2017, 13, 1602235.

[28] Siram, P.; Su, D.-S.; Periasamy, P. A.; Manikandan, A.; Wang, S.-W.; Chang, H.-T.; Chueh,Y.-L.; Yen, T.-J. Quadrupole Gap Plasmons: Hybridizing Strong Quadrupole Gap Plasmons Using Optimized Nanoantennas with Bilayer MoS_2 for Excellent Photo-Electrochemical Hydrogen Evolution. Adv. Eng. Mater. 2018, 8, 1801184.

[29] Zhang, H.-X.; Li, Y.; Li, M.-Y.; Zhang, H.; Zhang, J. Boosting electrocatalytic hydrogen evolution by plasmon-driven hot-electron excitation. Nanoscale 2018, 10, 2236-2241.

[30] Zhang, Y.; Du, J.; Luo, R.; Wang, Z.; Wang, Z.; Han, J.; Liu, P.; Fujita, T.; Xue, Q.; Chen, M. 3D bicontinuous nanoporous plasmonic heterostructure for enhanced hydrogen evolution reaction under visible light. Nano Energy 2019, 58, 552-559.

[31] Wang, T.; Liu, L.; Zhu, Z.; Papakostantinou, P.; Hu, J.; Liu, H.; Li, M. Enhanced electrocatalytic activity for hydrogen evolution reaction from self-assembled monodispersed molybdenum sulfide nanoparticles on an Au electrode. Energy Environ. Sci. 2013, 6, 625-633.

[32] Nait Saada, T.; Marques da Silva, A. G.; Subramanian, P.; Pang, L.; Adnane, N.; Bjafari-Rouhani, B.; Mishyn, V.; Meziane, D.; Sorin Melinte, S.; Sandu, G.; Dumeignil,

F.; Paul, S.; Wojcieszak, R.; Boukherroub, B.; Szunerits, S. Plasmon-Enhanced Electrocatalytic Oxygen Reduction in Alkaline Media on Gold Nanohole Electrodes. J. Mater. Chem. A 2020, https://doi.org/10.1039/C9TA14174J.

[33] Li, C.; Ye, R.; Bouckaert, J.; Zurituza, A.; Dridier, D.; Dumych, S.; Paryzhak, V.; Bilyy, R. O.; Melinte, S.; Li, M; Boukherroub, R. Flexible Nanoholey Patches for Antibiotic-Free Treatments of Skin Infections. ACS Appl. Mater. Interfaces 2017, 9, 36665-36674.

[34] Lausmaa, J.; Kasemo, B.; Mattsson, H. Surface spectroscopic characterization of titanium implant materials. Appl. Surf. Sci. 1990, 44, 133-146.

[35] Cheng, K.; Wang, S.; Cui, Z.; Li, Q.; Dai, S. Large-scale fabrication of plasmonic gold nanohole arrays for refractive index sensing at visible region. Appl. Phys. Lett. 2012, 100, 253101.

[36] Kang, Y.; Gong, Y.; Hu, Z.; Li, Z.; Qiu, Z.; Zhu, X.; Ajayan, P. M.; Fang, Z. Plasmonic hot electron enhanced MoS_2 photocatalysis in hydrogen evolution. Nanoscale 2015, 7, 4482.

CHAPTER 5

Conclusion and Perspectives

As the global energy crisis and environmental pollution problems continue to intensify, people gradually pay more attention to the search of renewable clean energy. The hydrogen (H_2) combustion value is high, and its product water is clean and pollution-free, and can be recycled. So H_2 has become an ideal energy carrier in people's minds. Therefore, the use of electrocatalytic decomposition of water to produce H_2 is a fundamental way for environmental issues. After years of research and development, the decomposition of water to produce H_2 have made great progress, but in general water splitting efficiency is still very low, far from reaching the actual application level. Therefore, the research on electrocatalytic H_2 production is still a hot spot in academia.

Hydrolyze water to produce H_2 is a research direction that has developed rapidly since the mid-1970s. The results achieved in recent years showed that it has attractive application prospects, but to achieve practical value, a series of major basic problems must be solved. The successful construction of a water splitting device requires at least one electrocatalyst, electrolyte and product separator. Most of the device designs reported in the literature must be based on high activity and estimated production costs.

Currently, Pt-group metals are the most effective catalysts for HER, while the benchmark catalysts for OER are Ir/Ru-based compounds. However, high cost and scarcity of these metals limit their widespread use. Therefore, enormous efforts have been dedicated to the development of nano-scale non-noble metal catalysts with high dispersibility, large specific surface area, and electrocatalytic activity for water splitting.

In this thesis, we have explored high-efficiency, high-stability, low-price electrocatalysts using a simple and environmentally friendly strategy. Firstly, we prepared

new $PtRu_2$ nanoparticles supported on sulphur and nitrogen co-doped crumbled graphene with trace amounts of iron ($PtRu_2$/PF) electrocatalysts by one-step hydrothermal process. We choose to reduce the Pt content through alloying with Ru. In the second part of my thesis work, we described the preparation of a hybrid material consisting of cobalt oxide decorated on nitrogen-doped MoS_2 supported on carbon fibers (CoO/N-MoS_2/CF) through a two-step process combining hydrothermal technique and electrochemical deposition. The third chapter of my thesis was focused on the plasmon-enhanced electrocatalytic processes. We showed, for the first time, the extraordinarily capacity of perforated gold nanoholes (Au NHs) electrodes for electrochemical water splitting under illumination. The strong electromagnetic enhancement, which occurs under illumination of the perforated Au NHs electrode, facilitates the dissociation of water into H_2. All the prepared materials were characterized by a variety of different techniques, such as SEM, TEM, XRD, XPS, Raman and electrochemical measurements.

Throughout the literature data and research, the current research on catalytic decomposition of water to produce H_2 was mainly focused on the design and preparation of new catalysts with low cost, high efficiency, no pollution and good stability.

At present, we mainly produce hydrogen through electrocatalysis water splitting. In the next step we will combine photocatalysis with electrochemistry to form a photoelectrochemical water splitting system. So far, this field faces many problems related to the low stability of the photocatalysts (photo-corrosion) and the low efficiency in the visible light region. So, I will prepare Au NHs with absorption in the visible range, use a lamp or sunshine as the power to promoted the water splitting. And I also will use optical lithography to generate structures. And in the future, solar cell may be used in the water splitting system. Although some progress has been made in the research on water photocatalysis in recent years, there are still many areas that need further research and improvement. Once the research on

the use of solar energy to catalyze the decomposition of water to produce H_2 can be put into practical use, it will fundamentally change the energy structure of the world today, with a broad prospect for development. The use of solar energy and catalytic decomposition of water to produce H_2 are research topics that are related to the destiny of any country and the well-being of mankind, and deserve our constant exploration.

Appendix

Experimental Part

6.1 Characterization techniques

6.1.1 Scanning electron microscopy (SEM)

SEM images were recorded using an electron microscope ULTRA 55 (Zeiss) equipped with a thermal field emission emitter and three different detectors (EsB detector with filter grid, high-efficiency In-lens SE detector, and Everhart-Thornley secondary electron detector).

6.1.2 Transmission electron microscopy (TEM)

TEM images were recorded on a FEI, TECNAI G2 F20 instrument. Samples were prepared by dispersing the electrocatalysts in ethanol (0.2 mg mL^{-1}). From the dispersed solution, 5 μL was drop casted on a 200 mesh Cu grid for the high-resolution transmission electron microscopy (HR-TEM) analysis.

6.1.3 X-ray diffraction (XRD)

XRD patterns were collected on a high flux Rigaku Smartlab rotated anode, working with a copper Kα radiation (1.5418 ang) at an applied voltage of 45 kV and an anode current of 200 mA in the 2θ range of 5-90°. After optimization, a Bragg-Brentano reflexion geometry configuration was chosen in combination with 5° Soller's slits in incident and diffracted beams. In addition, since the diffracted intensity is very weak, low background silicon sample-holders were used.

6.1.4 Raman spectroscopy

Raman measurements were performed on a LabRam HR Micro-Raman system (Horiba Jobin Yvon) using a 473-nm laser diode as excitation source. Visible light is focused by a 100× objective. The scattered light is collected by the same objective in backscattering configuration, dispersed by a 1800 mm focal length monochromator and detected by a CCD camera.

6.1.5 X-ray photoelectron spectroscopy (XPS)

XPS is an advanced analytical technique in the microanalysis of electronic materials and components. It not only provides information on molecular structure and atomic valence state, but also provides various information about the elemental composition and content, chemical state, molecular structure, and chemical bonds of a compound. When analyzing electronic materials, it can not only provide overall chemical information, but also give information on the surface, micro areas and depth distribution. In addition, because the X-ray beam incident on the surface of the sample is a photon beam, the damage to the sample is very small. This is very beneficial for the analysis of organic materials and polymer materials. XPS (ESCALAB 220 XL) spectrometer from Vacuum Generators featuring a monochromatic Al Kα X-ray source (1486.6 eV) was used to assess the chemical composition of the electrode materials.

6.1.6 Inductively coupled plasma atomic emission spectroscopy (ICP-AES)

The amount of Pt and Ru in prepared samples was determined with a Varian (liberty II axial view) ICP-AES. The wavelength and detection limit for Pt were 214.423 nm and 0.03 μg mL^{-1}, respectively and the wavelength and detection limit for Ru were 240.272 nm and 0.01 μg mL^{-1}, respectively. The spectrometer was equipped with a pneumatic V-groove nebulizer and Sturmun-Master inert PTFE spray chamber. Sample solutions were driven through columns of resin by means of a multi-channel Gilson peristaltic pump equipped with 2.28 mm i.d. tubing. Teflon tubing, polyethylene bottles, and a pH meter (WTW) with glass electrode were also used.

6.1.7 Ultraviolet-visible (UV/vis) spectrophotometer

The UV/vis absorption spectra were recorded using a Perkin Elmer Lambda UV-vis 950 spectrophotometer. The wavelength range is from 300-1050 nm.

6.1.8 Physical vapor deposition (PVD)

PVD technology means that under vacuum conditions, using a physical method, the material source-solid or liquid surface is vaporized into gaseous atoms, molecules or parts ionized into ions, and through low pressure gas (or plasma). The process of depositing a thin film with a special function on the surface of the substrate. The main methods of physical vapor deposition include vacuum evaporation, sputtering, arc plasma plating, ion plating, and molecular beam epitaxy. Up to now, physical vapor deposition technology can not only deposit metal films, alloy films, but also compounds, ceramics, semiconductors, polymer films, etc.

Publications

1) **Pang, L.**; Barras, A.; Zhang, Y.; Amin, M. A.; Addad, A.; Szunerits, S.; Boukherroub, R. CoO Promoted the catalytic Activity of Nitrogen-Doped MoS_2 Supported on Carbon Fibers for Overall Water Splitting. ACS Appl. Mater. Interfaces 2019, 11, 35, 31889-31898.
2) **Pang, L.**; Barras, A.; Mishyn, V.; Melinte, S.; Subramanian, P.; Boukherroub, R.; Szunerits, S. Enhanced electrocatalytic hydrogen evolution on a plasmonic electrode: the importance of the Ti/TiO_2 adhesion layer. J. Mater. Chem. A 2020, 8, 13980-13986.
3) Tamazouzt, N.; da Silva, A.; Subramanian, P.; **Pang, L.**; Adnane, N.; Djafari-Rouhani, B.; Mishyn, V.; Meziane, D.; Melinte, S.; Sandu, G.; Dumeignil, F.; Paul, S.; Wojcieszak, R.; Boukherroub, R.; Szunerits, S. Plasmon-Enhanced Electrocatalytic Oxygen Reduction in Alkaline Media on Gold Nanohole Electrodes. J. Mater. Chem. A 2020, 8, 10395-10401.
4) **Pang, L.**; Bhange, S. N.; Barras, A.; Addad, A.; Roussel, P.; Amin, M. A.; Kurungot, S.; Szunerits, S.; Boukherroub, R. The ultimate limit of Pt electrocatalytic activity in PtRu/nitrogen and sulphur co-doped crumbled graphene in acid and alkaline media. Electrochim. Acta. Submitted.